ROMANIAN ACADEMY

ROMANIAN ASTRONOMICAL JOURNAL

Vol. 28 • No. 2 • 2018

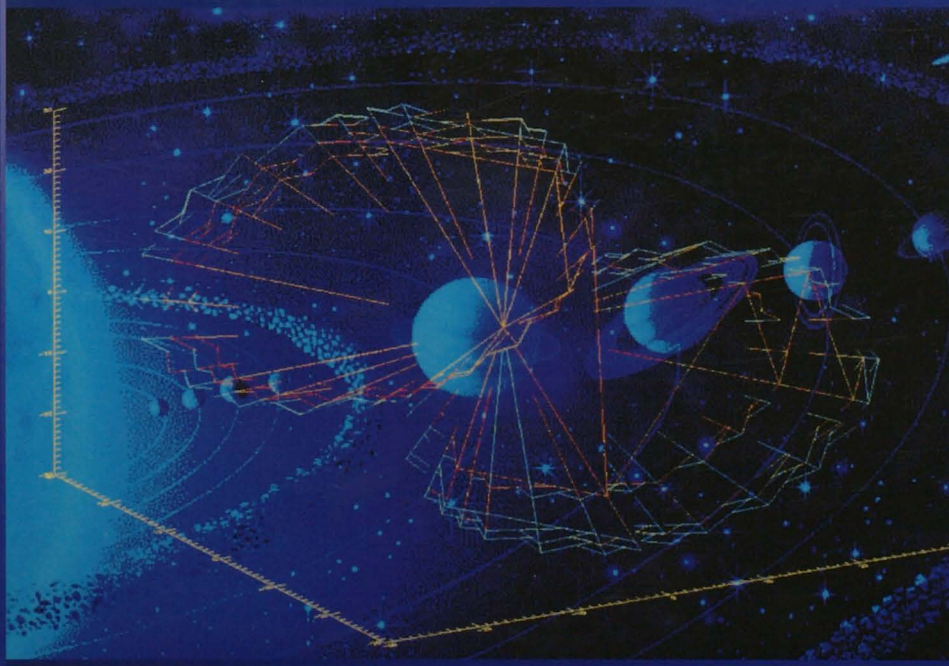

EDITURA ACADEMIEI ROMÂNE

ROMANIAN ACADEMY

ROMANIAN ASTRONOMICAL JOURNAL

The ROMANIAN ASTRONOMICAL JOURNAL appears twice a year. Orders from abroad (issues or subscriptions) should be sent to:

EDITURA ACADEMIEI ROMÂNE, Calea 13 Septembrie nr. 13, sector 5, 050711, Bucureşti, România, Tel.: 4021-318 8146, 4021-318 8106, Fax: 4021-318 2444, E-mail: edacad@ear.ro, Web: www.ear.ro

ORION PRESS IMPEX 2000 S.R.L., P.O. Box 77–19, sector 3, Bucureşti, România Tel.: 4021-210 6787; 4021-610 6765; Email: office@orionpress.ro

S.C. MANPRES DISTRIBUTION S.R.L., Piaţa Presei Libere nr. 1, Corp B, Etaj 3, Cam. 301–302, sector 1, Bucureşti, România, Tel.: 4021-314 6339, Fax: 4021-314 6339 Email: abonamente@manpres.ro, office@manpres.ro www.romanianjournals.com

S.C. SORIRORI SOLUTIONS S.R.L., Tel.: 004 0765 262 077, 004 0765 166 433; Internet: http://www.sorirori.ro; E-mail: sorin.costreie@sorirori.ro, rosana.guta@sorirori.ro

CRIS MEDIA PRESS IMPEX S.R.L., P.O. Box 41–71, sector 1, Bucureşti, România Tel.: 004 0722 333 405, 004 0744 325 043
E-mail: office.crismedia@gmail.com

The manuscripts, the books and journals proposed in exchange and the mail should be sent to the Editorial Board.

Editorial Board's Address:

ROMANIAN ASTRONOMICAL JOURNAL
Astronomical Institute of the Romanian Academy
Str. Cuţitul de Argint 5
RO-040557 Bucharest 28
Phone: +(4021) 335 68 92, +(4021) 335 80 10
Phone/Fax: +(4021) 337 33 89
E-mail: roaj@aira.astro.ro
http://www.astro.ro/~roaj/
Romania

Work published with financial support from Recurring Donor Fund of the Romanian Academy.

ROMANIAN ASTRONOMICAL JOURNAL

Vol. 28 , No. 2, 2018

CONTENTS

OBSERVATIONAL ASSET FOR NEO AND SPACE DEBRIS

MIREL BIRLAN[1,2], VASILE PLEŞCA[3,4], COSTIN HEDWIG GÂNDESCU[3,4], DAN ALIN NEDELCU[2,1], MUGUREL BĂLAN[5], COSMIN BĂNICĂ[3,4], CONSTANTIN PANDELE[5], ADRIAN SONKA[1,6], TUDOR GEORGESCU[7]

[1]*Institut de Mécanique Céleste et des Calculs des Éphémérides, CNRS UMR8028, Observatoire de Paris, PSL Research University, 77 av Denfert-Rochereau, 75014 Paris Cedex, France*
Email: Mirel.Birlan@imcce.fr
[2]*Astronomical Institute, Romanian Academy, 5-Cuţitul de Argint, 040557 Bucharest, Romania*
[3]*Wing Computer Group SRL, Sos. Virtuţii 19D, 060042 Bucharest, Romania*
[4]*Faculty of Electric Engineering, Politehnica University Splaiul Independenţei 313, corp EA, 060042 Bucharest, Romania*
[5]*Institute of Space Science,409, Atomiştilor Street, 077125 Măgurele, Ilfov, Romania*
[6]*Faculty of Physics, Bucharest University, 405, Atomiştilor Street, 077125 Măgurele, Ilfov, Romania*
[7]*Elcos Proiect SRL, Str. Blândeşti 24C, 060042 Bucharest, Romania*

Abstract. Near-Earth Objects, artificial satellites and space debris are objects of the *Earth-Space-Environment*(SEE). New data are required continuously for these objects for improving their ephemerides. In the case of Near Earth Objects optimal periods of observations are sparse over the century and in the order of 10-30 days. It is mandatory to exploit these situations in terms of observations for refine the orbit and for derive their physical properties. For the artificial satellites optical observations should be addressed in order to corroborate telemetry and other observational techniques. An increasing importance is addressed to space debris, which are tremendously increased into the last decade. Their orbital evolution is very sensitive to gravitational harmonics of the Earth, tidal effects of the Moon, Sun and major planets, and to non-gravitational forces. Observational survey is required during their evolution on the orbit but also during their falls through the atmosphere. The article presents the premises of a modern asset which should answer to the problematic of observations of Near-Earth Objects, artificial satellites, and space debris in a paradigm of a mobile system which can be rapidly deployed.

Key words: instrumentation – observations – Near-Earth Object – space debris..

1. INTRODUCTION

Earth-space-environment (ESE) is considered as the interplanetary space which starts usually from 100 of kilometers of altitude, conventionally called *Karman line* (Okninski, Raurell, and Mitre, 2016). The common upper limit of ESE is located approximately at 7.5 million of kilometers around the Earth.

Out of the Moon, there are several categories of objects which cross/intersect the Earth orbit's such are *Near-Earth Objects* (NEOs), comets, meteors showers, torus of dust and gas, and random meteoroids. Also, in the last seven centuries, the results of mankind have put in orbit inside ESE a large number of artificial satellites which are largely used for daily life of peoples. The life on Earth is now strongly connected with space activities.

1.1. ASTEROIDS

During the 15 years of efforts of observational surveys for detecting and cataloged NEOs achieved a completeness of 99% for the objects with a diameter larger than 1 kilometer (Michel, 2013). This completeness is still a desiderata for object with diameters between 140 meters and 1 kilometer, a common work of scientific community and specific surveys such as Catalina Sky Survey, PanStarrs, Linear, NEAT, Spacewatch.

During the history of Earth, collisions with asteroids have altered the course of life, and there is no reason that these unpredictable events should not continue. Detailed analyses of questions related to realistic options for preventing the collision of a NEA with Earth are now performed in Europe (Harris *et al.*, 2015). Several similar initiatives for providing detailed test mission designs for mitigation processes are now developed all over the world. These initiatives include both researchers in fundamental sciences and industries specialized in space explorations to establish a correct scenario of each situation. Each scenario is specific to each NEO that is subject to mitigation. Thus, a good knowledge of the physical properties of NEOs and the response of various types of external stress is required to design an efficient mitigation tool (Michel, 2013).

Some spectral data of NEOs are also obtained and analyzed in short time dedicated campaigns. Thus, very important scientific data were obtained for the asteroid (357439) 2004 BL_{86} in February 2015. These results conclude to a diameter of this object 40% smaller than the previous estimation (Birlan *et al.*, 2015), and a mineralogy of its surface similar to basalt. Observations of Near-Earth-Asteroid (214869) 2007 PA_8 in November 2012 conclude to an object with mineralogy similar to ordinary chondrite iron-rich meteorites; backward numerical integration of its orbit concluded to an express delivery of this objects from the Main-Belt of asteroids to NEO population in less than 200,000 years (Nedelcu *et al.*, 2014).

While NEOs evolve on orbits much closer to Earth than main belt asteroids, the common idea might be that they can be observed more easily and more often. Their small diameters imply tight constraints that are related to their close encounters with Earth. Unfortunately, when the ephemerides are computed it show that the NEO encounters occur on average three to five times per century (Birlan *et al.*, 2016).

Due to their relative velocity to the Earth, of around 11 km/s, these observational windows are very tight. Depending on how NEOs are grazing the Earth, the interval of observations could be in the order of few hours, up to few weeks. Thus it is mandatory to use these favorable geometries to perform as many observations as possible to constrain the asteroid position, its mass and internal structure, the surface composition and rugosity.

Additional important objective is the tackling of critical missing link between asteroids and meteorites (Dumitru *et al.*, 2017) by combining optical observations of NEAs as meteorite sources and of meteors as asteroidal/cometary materials sampled by Earth atmosphere during entry. The important addition of meteorite radar detection provide a third, independent set of valuable data used to study the aforementioned link. We note that radio data is available both during daylight and during times unsuitable for astronomical observations.

1.2. ARTIFICIAL OBJECTS

ESE until 36,000 km of altitude is populated by artificial objects. Depending on altitude the satellites are classified into *Low Earth Orbit* (LEO) when the altitude is lower than 1,500 km, *Medium Earth Orbit* (MEO) when the altitude is between 1,500 km and 20,000km and Geostationary Earth Orbit (GEO) when the altitude is around 36,000 km (Capderou, 2005). There are however few category of satellites like Molnya and Tundra with orbits of *high eccentricity* (HEO). Sometimes for short periods GEO satellites could be also on *Geostationary Transfer Orbits* (GTO). Some of satellites for which the launching procedure do not allows to put them into a nominal orbit are usually on *Failed Transfer Orbits* (FTO).

Each launch of a new artificial satellite is subject of collateral space junks which allow its insertion on a nominal orbit. The generic term of space debris is commonly used to define upper stage of rockets, pieces of shield, solar panels, dead satellites, etc. In the same category of space debris we will include also the results of accidental collisions between satellites or experiments of destroying of satellites. Such an accidental collision occurs in February 2009 between the Iridium-33 satellites and the Kosmos-2251 one (Sudheer Reddy, Gopal Reddy, and Anilkumar, 2011).

Mathematical models of space debris elaborated by the European Space Agency estimate that in July 2013 the Earth environment is populated by more than 29,000 space junks larger than 10 cm, more than 670,000 fragments with sizes larger than 1 cm, and more than 170 millions of debris with sizes larger than 1mm. They are traveled from space with a speed larger than 8 km/s, value large enough to damage a satellite or a spacecraft. Larger space debris could be tracked from the ground, as well as some space junks larger than 2cm in size, while the mm size space debris

could not be tracked from the ground. However, objects smaller than 10 cm are not consistently trackable, thus no active collision avoidance is possible using nowadays mathematical models.

Satellites could be also subject of collisions with meteoroids. In 1993 the European Space Agency satellite Olympus 1 was put out of service during the Perseid meteor shower, while the satellite Lansat 5 began to spin out of control during the same Perseid meteor shower, in 2009.

Tracking space debris is now of a real importance for the development of space exploration. The *High Area-to-Mass Ratio* (HAMR) space debris need to be tracked not only using the ephemerides derived using the geopotential of Earth, but also by including non-gravitational forces such as drag effect, radiation pressure, Poynting-Robertson effect, etc (Rosengren and Scheeres, 2013). Due to their high area-to-mass ratios, solar radiation pressure perturb their orbits in ways that makes it difficult to predict their orbital trajectories over periods of time exceeding a week (Skinner *et al.*, 2011). Consistent study of these HAMR objects requires repeated follow-up and tracking. Usually, HAMR objects are subject of random, spinning or tumbling movement, under the effects of geo-lunar-solar gravitation, unmodeled solar radiation pressure, thermal emission, and electrostatic charging which induced perturbation of trajectory. The models and should account these effects into the procedure of adjustment in order to increase the orbital parameters and prediction (Kelecy and Jah, 2011).

The aim of this article is to put bricks and basics of a concept for an optical mobile facility able to tackle simultaneously the problematic of NEOs and space debris. The asset could tackle the subject of ESE through the perspective of optical observational astronomy, by means of a mobile system which can address problematic of space awareness, science of orbital evolution of objects, and links between astronomical reference frames.

2. BASICS

Apart the diurnal movement of Earth, both NEOs and artificial objects experienced high rate differential movement in the sky.

Constrains on observing artificial satellites and space debris from the ground are directly related to their relative angular velocity(as seen from the groundbased observer), dimensions, attitude, and reflective properties. For the estimation of performances of future asset, these constraints shall be integrated to seeing, telescope aperture, and performances of CCD detectors.

Using basic radiometric equations we can estimate the detection thresholds for objects in Low, Medium and Geostationary orbits (Table 2). For this simulation the

Table 1

Simulation of detection for asset of 0.6 meter aperture telescope, for LEO, MEO, and GEO objects. The simulation was performed using the thresholds as mentioned in the text

LEO 0.01s exp time			MEO 0.1s exp time			GEO 1.0s exp time		
Mag(V)	SNR	Size(m)	Mag(V)	SNR	Size(m)	Mag(V)	SNR	Size(m)
10	73	0.12	10	276	6.05	10	895	10.82
11	37	0.08	11	167	3.82	11	559	6.83
12	17	0.05	12	96	2.41	12	344	4.31
13	n/a	n/a	13	51	1.52	13	205	2.72
14	n/a	n/a	14	24	0.96	14	115	1.71
15	n/a	n/a	15	10	0.6	15	58	1.08
16	n/a	n/a	17	n/a	n/a	16	27	0.68
17	n/a	n/a	17	n/a	n/a	17	11	0.43

most favorable conditions of astronomic observations were taken into account: night with New Moon, an airmass = 1, the unfiltered CCD observations, a sky brightness of 19 mag/arcsec^2, the atmospheric extinction of 0.2 mag and no telescope optical losses. We used a 0.6 m, f/6 telescope and a detector with 80% quantum efficiency (CCD camera). The detector was considered having 13 μm pixel size. Thus, this configuration can detect objects of magnitudes 12, 15, and 17 for exposure times of 0.01, 0.1 and 1.0 seconds respectively, in the assumption of with SNR$\geq$10. The maximum exposure time is determined by the need to keep the detection trail $\leq$ than 3 arcsec, a length comparable with a modest value for atmospheric seeing.

The sizes of objects corresponding to the limiting magnitude (assuming a diffuse Lambertian phase function and an albedo of 0.1) at distances of 400, 20,000, and 36,000km are presented in Table 2.

These constraints are less important for NEOs, except some peculiar cases when the object will graze the Earth toward distances lower than Earth-Moon one. In the case of NEOs, optimal periods of observations are sparse over the century and in the order of 10-30 days. Thus, we stress the importance to exploit these favorable situations in terms of observations for refine the orbit and for derive their physical properties. Non-gravitational effects should be quantified and included as input for mitigation processes and scenarios.

Another aspect tackled during the conception of the asset is the system of data acquisition and archiving.

The *Flexible Image Transport System* (FITS) is the de facto standard for astronomical images exchange and archiving in the digital era (Pence *et al.*, 2010). FITS represents a portable, hardware-independent and self-describing system for storing scientific data (images, spectra, data cubes, tables, etc.) together with relevant metadata (Calabretta and Greisen, 2002).

For astronomical images, the size of FITS files mainly depends on the detectors

array size with a minimal contribution from ASCII card metadata. Thus, a detector with an array of size Md (in megapixels) will produce FITS images of size Md*32 (in megabits) for 32-bit integer format.

FITS images contain too much noise (thermal, electronic, sky background variability, etc.) to be losslessly compressed in an efficient manner. As a test, we generated a set of FITS images ranging in size from 100x100 pixels to 4Mx4M pixels by adding random stars of SNR 2 to 10 (as Gaussian) over a random sky background. Lossless compression algorithms as bzip2 and gzip achieved only a modest compression ration of 1.13.

If a lossy compressed image is acceptable, a significantly higher compression factor than the lossless compression algorithms can be obtained if we don't want to exactly preserve every bit of the original image pixel values. For the same set of FITS images, lossy algorithms implemented by fpack tool (Pence, Seaman, and White, 2009), compressed data with a significantly higher ratio of 6.2 (Figure 1).

Using these results we can estimate the volume of data produced by the telescope in a single hour of observations. For exposure times short enough to detect fast moving objects (10 seconds including image download and storing overhead) a 2Mx2M pixels detector will produce 900MB of lossy compressed images or, alternatively, 5.5 GB of lossless compressed data. A further data volume reduction factor of 4 can be obtained by using the detector in 2x2 binning mode.

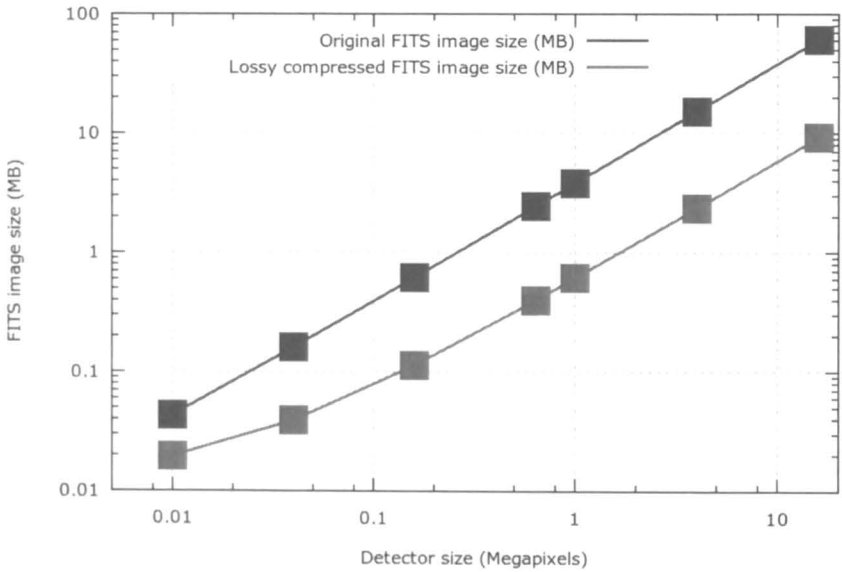

Fig. 1 – FITS image size as function of detector size for 32-bit integers format.

3. TECHNICAL REQUIREMENTS

Technical requirements are designed depending on scientific objectives of the mobile asset, namely: i) observations on alert for NEOs during the close encounters with the Earth, ii) space debris, and iii) satellite tracking.

One series of technical requirements might be:

- Mobile system; the system is designed based on a frame made up of a transport container that can be easily loaded and unloaded on a transport trailer;
- High precision telescope; the system contains the optical device precisely leveled with a specific sensor, high precision leveling platform and the movement of the telescope is controlled by a custom software plus high speed and high precision drives;
- Automated; the system can be fully automated thanks to multiple, separate automation systems that control all the included subsystems;
- Remote controlled; the system can be remote controlled to perform different tasks, regarding the minimization/optimization of electrical consumption and data acquisition;
- Autonomous; thanks to renewable energy systems that is built in the platform covers the daytime consumption and handles the recharging of the battery pack, plus the added generator covers peak consumption and emergency situations, the system can be fully automated;
- Customized frame; the system might be designed inside a transport container custom retrofitted to allow side mounting of the solar panels, with a custom lid that can easily be opened and closed to allow the telescope activities, all those modifications to the classical frame follow the regulations imposed by the road, railway, and maritime transport rules.
- Weather and weather forecast; the system could be able to process realtime meteorological data and derive the sky coverage and atmospheric conditions over a period of 7-15 days by processing inputs of weather forecast;
- Information technology system; the system might allow the main point to point communication system, stores the data acquired from the telescope, keeps a record of the data acquired from the sensors and security systems;
- Scientific pre-processing and archiving; the system can allow on-board pre-processing of scientific images thanks to a specific pipeline for astronomic data

reduction. The processed data need a specific format to be ingested into the databases for astronomical observations;

As an example, one version of the electric system of such an asset could be seen in Figure 2.

The identification of power consumers was made as following: telescope mount, CCD camera, horizontal container stabilizer, system mechanism for roof opening and closing sequence, IT central unit, communication system elements.

The power system can contain several components such are:

1. Photovoltaic cell panels. One string of four panels each shall be mount on both laterals of the container. These photovoltaic polycristallin panels ensure battery charge during the day, thus being a continuous energy reserve. The panels will drop down costs due to fossil fuel used to produce electricity and will raise the efficiency. The panels might be fixed on the container such as each orientation of this one will allow the same collected power from the Sun. Their installation will not change the container gauge.

2. Battery system. This system will be composed by several batteries working in isolation, ensuring the energy back-up and security of devices. The batteries might be chosen among the deep-cycle device because of their continuous operation. This will allow at least 2,000 loading/unloading cycles without damaging the internal structure of batteries.

3. Charging regulator. This subsystem is managing the process of loading of batteries, verifying the temperature and the value of current. The sub-system shall be calibrated for each of photovoltaic panel toward the optimization of loading process.

4. Power generator. This is a high power monophasic 230V AC generator which can also turn 12V DC. The sub-system will be callibrated as function of photovoltaic system. The generator should be automated when the power level of batteries (produced by solar cells) cannot assure the level for a nominal functioning of asset. A sensor sub-system of fuel level allows the estimation of left operating time for the generator.

5. Automation. The network of sensors (intensity and voltage, temperature, humidity, fuel level) will allow the automation of electric system. The management of this sub-system could be done using an industrial IT equipment such as the AMTEL/ARDUINO kit.

6. Electric inverter. This sub-system will transform DC current from battery system to AC current required by the major part of components. The selected

inverter transforms into a sinusoidal AC, excellent for component performance. The inverter shall be chosen in order to manage the situation on which the power comes from the national electric power SEN.

7. Security elements. These are AC and DC electric fuses which can act in the case of short circuit of one of consumer, and protect for damage other system of sub-system of the asset.

Electric power system for the asset is vital while it is conceived to work autonomously. The fine tuning of using source energies and their priority is sensitive. Thus, the batteries will be used during the observational run, while the thermal generator could induce vibrations and smog which will alter the quality of acquired scientific data.

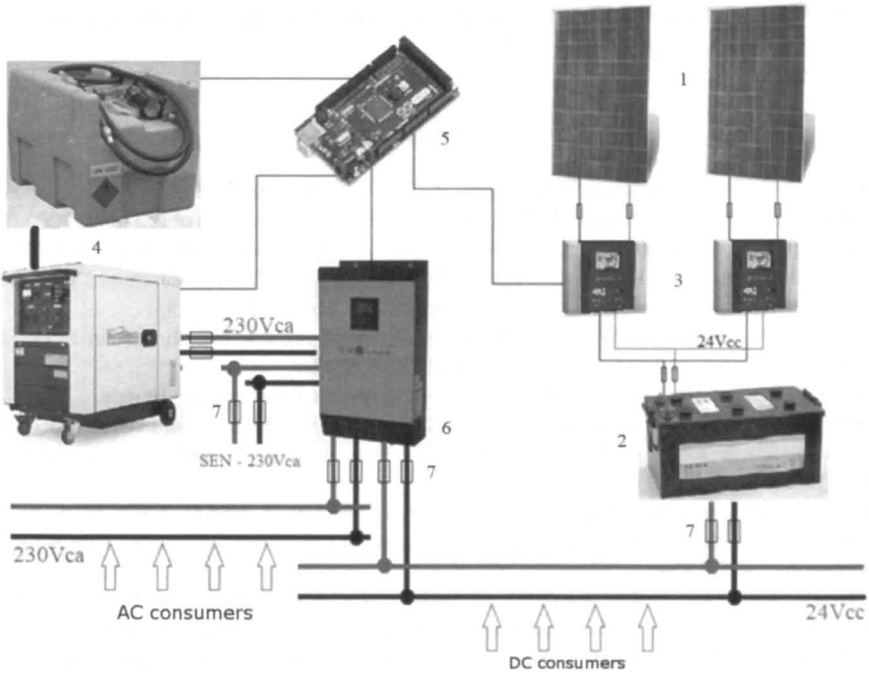

Fig. 2 – Global image of the power system.

In the case of mechanical system for the mobile asset, the requirements of design should account for:

- the sub-system of stabilizing the container;
- the sub-system of roof opening/closing;

- the sub-system of lifting and positioning the telescope;
- the sub-system of power supply location inside the container;

4. CONCLUSION

Requirements for observing objects inside ESE, namely NEOs, artificial satellites, and space debris, are presented. Basis of acquiring optimal data using a new concept of mobile optical asset allow the identification of systems and sub-systems necessary for the design. Simulation of concept, as well as scenario of some systems were briefly described.

Acknowledgements. This scientific study was supported by the grant of the Romanian National Authority for Scientific Research, Program for research - Space Technology and Advanced Research - STAR, project number 465.

REFERENCES

Birlan, M., Popescu, M., Nedelcu, D.A., Turcu, V., Pop, A., Dumitru, B., Stevance, F., Vaduvescu, O., Moldovan, D., Rocher, P., Sonka, A., Mircea, L.: 2015, Characterization of (357439) 2004 BL86 on its close approach to Earth in 2015. *Astron. Astrophys.* **581**, A3. doi:10.1051/0004-6361/201526460.

Birlan, M., Nedelcu, D.A., Sonka, A., Popescu, M., Dumitru, B.: 2016, Observations for Secure and Recovery Near-Earth Asteroids. *Romanian Astronomical Journal* **26**, 25 – 33.

Calabretta, M.R., Greisen, E.W.: 2002, Representations of celestial coordinates in FITS. *Astron. Astrophys.* **395**, 1077 – 1122. doi:10.1051/0004-6361:20021327.

Capderou, M.: 2005, *Satellites - Orbits and missions*, Springer France, Paris, France.

Dumitru, B.A., Birlan, M., Popescu, M., Nedelcu, D.A.: 2017, Association between meteor showers and asteroids using multivariate criteria. *Astron. Astrophys.* **607**, A5. doi:10.1051/0004-6361/201730813.

Harris, A.W., Boslough, M., Chapman, C.R., Drube, L., Michel, P., Harris, A.W.: 2015, In: Michel, P., DeMeo, F.E., Bottke, W.F. (eds.) *Asteroid Impacts and Modern Civilization: Can We Prevent a Catastrophe?*, 835 – 854.

Kelecy, T., Jah, M.: 2011, Analysis of high area-to-mass ratio (HAMR) GEO space object orbit determination and prediction performance: Initial strategies to recover and predict HAMR GEO trajectories with no a priori information. *Acta Astronautica* **69**, 551 – 558. doi:10.1016/j.actaastro.2011.04.019.

Michel, P.: 2013, Physical properties of Near-Earth Objects that inform mitigation. *Acta Astronautica* **90**, 6 – 13. doi:10.1016/j.actaastro.2012.07.022.

Nedelcu, D.A., Birlan, M., Popescu, M., Bădescu, O., Pricopi, D.: 2014, Evidence for a source of H chondrites in the outer main asteroid belt. *Astron. Astrophys.* **567**, L7. doi:10.1051/0004-6361/201423949.

Okninski, A., Raurell, D.S., Mitre, A.R.: 2016, Feasibility of a low-cost sounding rockoon platform. *Acta Astronautica* **127**, 335 – 344. doi:10.1016/j.actaastro.2016.06.010.

Pence, W.D., Seaman, R., White, R.L.: 2009, Lossless Astronomical Image Compression and the Effects of Noise. *Pub. Astron. Soc. Pac.* **121**, 414. doi:10.1086/599023.

Pence, W.D., Chiappetti, L., Page, C.G., Shaw, R.A., Stobie, E.: 2010, Definition of the Flexible Image Transport System (FITS), version 3.0. *Astron. Astrophys.* **524**, A42. doi:10.1051/0004-6361/201015362.

Rosengren, A.J., Scheeres, D.J.: 2013, Long-term dynamics of high area-to-mass ratio objects in high-Earth orbit. *Advances in Space Research* **52**, 1545 – 1560. doi:10.1016/j.asr.2013.07.033.

Skinner, M.A., Russell, R.W., Rudy, R.J., Gutierrez, D.J., Kim, D.L., Crawford, K., Gregory, S., Kelecy, T.: 2011, Time-resolved infrared spectrophotometric observations of high area to mass ratio (HAMR) objects in GEO. *Acta Astronautica* **69**, 1007 – 1018. doi:10.1016/j.actaastro.2011.06.018.

Sudheer Reddy, D., Gopal Reddy, N., Anilkumar, A.K.: 2011, Modeling spatial density in low earth orbits using wavelets and random search. *Advances in Space Research* **48**, 1432 – 1440. doi:10.1016/j.asr.2011.06.015.

Received on 21 April 2018

PHOTOMETRIC MONITORING OF PHA (3122) FLORENCE

ADRIAN BRUNO SONKA[1,2], ANDREEA IOANA GORNEA[1,3], MIREL BIRLAN[1,4]

[1]*Astronomical Institute of Romanian Academy*
5 Cutitul de Argint, 040557 Bucharest, Romania
Email: sonka@astro.ro
[2]*Faculty of Physics, University of Bucharest*
405 Atomistilor, 077125 Magurele, Ilfov, Romania
[3]*Technical University of Civil Engineering Bucharest*
Lacul Tei Bvd. 122 - 124, 020396 Bucharest, Romania
[4]*IMCCE, Observatoire de Paris*
77 av Denfert Rochereau, 75014 Paris Cedex, France

Abstract. During a close approach of minor planet (3122) Florence we took the opportunity to determine and monitor changes in the synodic period of this *Potentially Hazardous Asteroid*. We found that the period varied in such degree that it was difficult to match observations made during several nights. A common synodical period was found to be 2.615 ± 0.003 h. The amplitude of brightness variation of Florence was found to be of 0.3 magnitudes. The absolute magnitude was determined as H = 13.542 ± 0.188 and the slope parameter as G = 0.169 ± 0.09.

Key words: Near-Earth Asteroid – photometry – lightcurve.

1. INTRODUCTION

Minor planet (3122) Florence is the 5^{th} largest Potentially Hazardous Asteroid (PHA) discovered so far. The group of Potentially Hazardous Asteroids consists of minor planets that have a minimum orbital intersection of less than 0.05 AU and are larger than 140 m, the size being defined as an absolute magnitude of 22 or brighter. Until April 24^{th} 2018, 1905 PHAs have been discovered.

Florence was discovered at Siding Spring Observatory, on March 2^{nd}, 1981, by S.J. Bus, and it was found that it periodically approaches Earth at nominal distances smaller than 0.4 AU, and sometimes smaller than 0.05 AU, as in 1930, 2017 and 2057.

The most recent size estimation of this minor planet, based on NEOWISE spectrophotometric data, states a diameter of 4.40 ± 0.03 km (Mainzer *et al.*, 2011). Another result comes from Thomas *et al.* (2011), who determined a visual albedo of 0.21 from Spitzer Space telescope in its Warm Spitzer Mode. Combined with Harris (1997) model diameter measurement based on absolute magnitude and visual albedo, an albedo of 0.21 and an absolute magnitude of 14.1 give a diameter of 4.4 km for Florence, in good agreement with the first result.

Using M4AST tool for modelling spectra of minor planets (Popescu *et al.*, 2012; Birlan *et al.*, 2016) we found that in Bus-DeMeo taxonomic system (DeMeo *et al.*, 2009) Florence is classified as type S (de León *et al.*, 2010). S class is the third important main-belt population, representing 8% of its mass (Binzel *et al.*, 2004). In 2017, using a low resolution spectrograph and only visible data, Gherase *et al.* (2017) established that Florence belongs to the Q type minor planets.

Florence was also observed by radar with NASA's Goldstone Deep Space Communications Complex on August 29^{th} and September 14^{th}, 2017. The doppler-delay images show the 4.5 km small elongated body of the asteroid and two small moons (between 100-300 m), which rotate in 8 and 25 hours (`https://cneos.jpl.nasa.gov/news/news199.html`). The asteroid's synodic period was found by radar to be 2.4 hours.

The synodic period found at the previous approach is close to 2.36 h, according to Pravec *et al.* (2002), Elenin and Molotov (2012) and Warner (2016). In 2017 the synodic period was found to be in good agreement with previous results (Franco *et al.*, 2018; Rodrigo *et al.*, 2018; Tomassini *et al.*, 2018; Klinglesmith III and Hendrickx, 2018). There is also a hint of a second period of 11.899 hours, superimposed on the main period (Rodrigo *et al.*, 2018).

2. OBSERVATIONS

In September 1^{st}, 2017, Florence came as close as 0.047AU from Earth, being at the smallest distance from our planet in recent history and for the following 150 years. For a period of nine months, during its closest approach, the asteroid was brighter than 16^{th} magnitude, and a good target for our equipment.

The observations were carried at the Astronomical Institute of the Romanian Academy (IAU MPC code 073). We used the 0.38-meter f/8 Ritchey-Chretien telescope (Gherase *et al.*, 2017) and a SBIG STL-11000M CCD camera, cooled down to $-20\,^{\circ}$C. The field-of-view is 44x29 arcmin and the pixel scale of 1.3 arcsec/pixel (a 2x2 binning was used during the run, in order to minimize image download time from sensor).

We observed the asteroid for nine nights during three runs per night, in order to find variability in the synodic period. In September and December 2017, we acquired V filtered images (Johnson photometric system). The observing circumstances are in Table 1. The asteroid was also observed in January 2018, but in less favourable conditions (high airmass and high apparent magnitude).

For our analysis we used a total of 982 data points. The small amplitude of the brightness variation on January 2018 did not allow us to detect any variability so we discarded the data.

Table 1

Observing circumstances with the beginning and the end of every observing run, the exposure time used, the apparent visual magnitude, the airmass at the beginning and the end of the session, the phase angle and the Earth-asteroid distance (Delta) in AU

Day UT start - UT end [hh:mm]	Exp. time [s]	V [mag]	Airmass	Phase [deg]	Delta [AU]
10.09.2017 20:01 - 23:22	30	11.2	1.1-1.4	71.4	0.081
11.09.2017 19:48 - 22:46	30	11.4	1.1-1.3	73.2	0.088
12.09.2017 19:36 - 21:49	30	11.6	1.1-1.3	74.6	0.094
21.09.2017 20:17 - 22:24	45	12.9	1.3-1.5	79.5	0.156
23.09.2017 19:58 - 22:01	45	13.1	1.3-1.5	79.5	0.170
22.12.2017 17:18 - 19:50	60	15.1	1.3-1.2	37.8	0.571

3. DATA PROCESSING

The raw images were calibrated with bias, flats and darks using the standard procedures of MaxIm DL (2016) software. The dataset was processed with MPO Canopus software (Warner, 2015). Differential photometric measurements were performed using the *Comp Star Selector* (CSS) procedure in MPO Canopus, which allows selecting up to five comparison stars with a near solar color. The magnitudes of the comparison stars were taken from the CMC-15 catalogue. For direct measurement of the asteroid and reference star brightness, a measuring aperture size of two times FWHM was used. Further, the period analysis was performed using MPO Canopus software (Warner, 2015), which includes uses the FALC (*Fourier Analysis for Lightcurves*) algorithm (Harris *et al.*, 1989).

4. RESULTS

Our main interest was to characterize the synodical period at different observational runs of minor planet (3122) Florence. We found that the synodic period varies from night to night, and that all our observations could not be fitted into a single period. Almost every night the observational time span exceeded the synodical period already reported in the literature and we could see the full rotation of the minor planet.

The lightcurve is bimodal, with a maximum that is 0.1 magnitudes brighter than the other. The amplitude of the brightness variation spans the range of 0.2 to 0.4 magnitudes. We found that the synodical period varies to a degree that makes it difficult to combine lightcurves made on subsequent days.

A Fourier fit for all the observing sessions yielded a period of 2.615 ± 0.003h, a value that is not in close agreement with previous results. It is obvious from Figure 2 that the data can not be fitted into a single period, the data from December 21st being

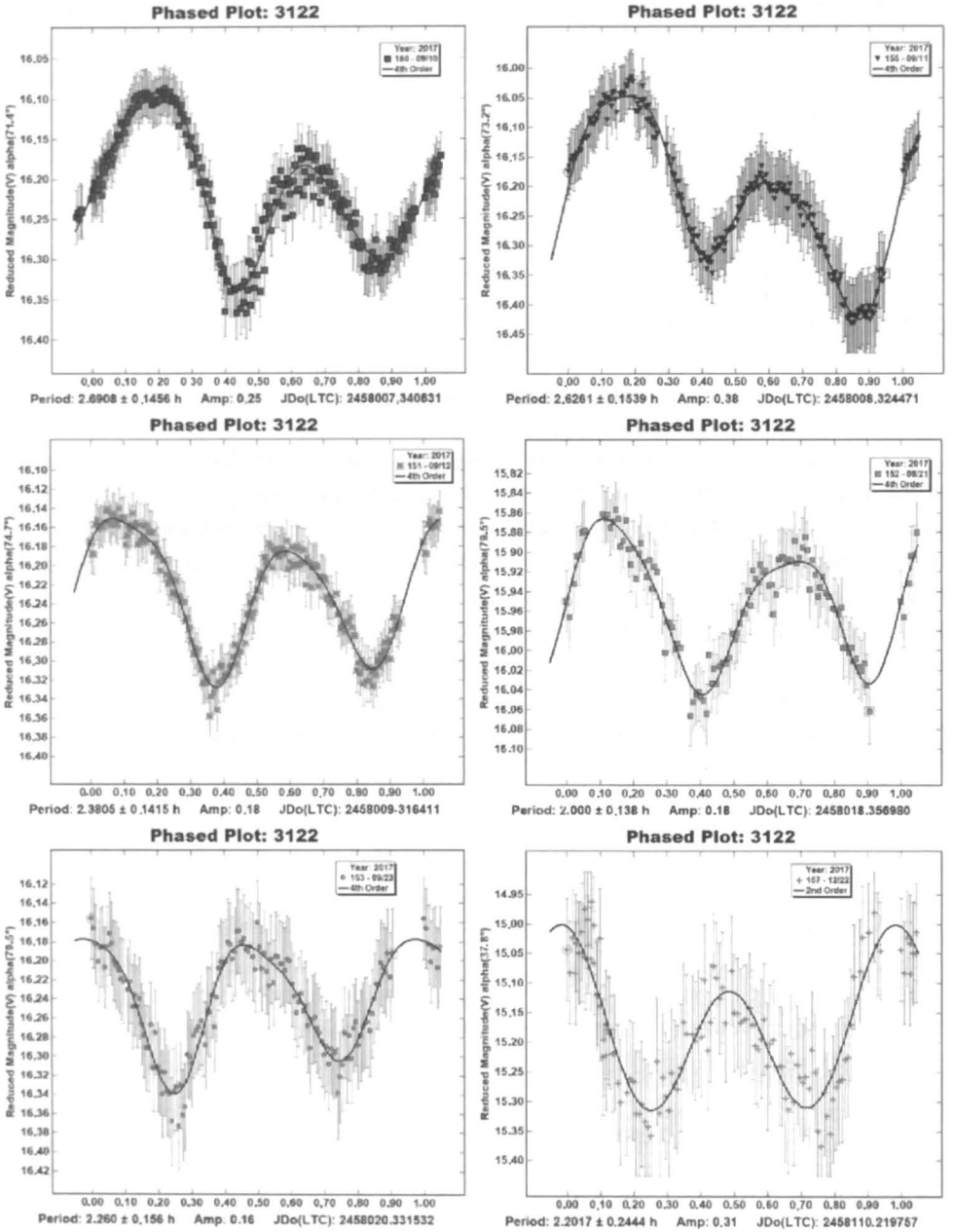

Fig. 1 – Period determination for every night of observation. The plot shows the magnitude errors and a spline fit through data points.

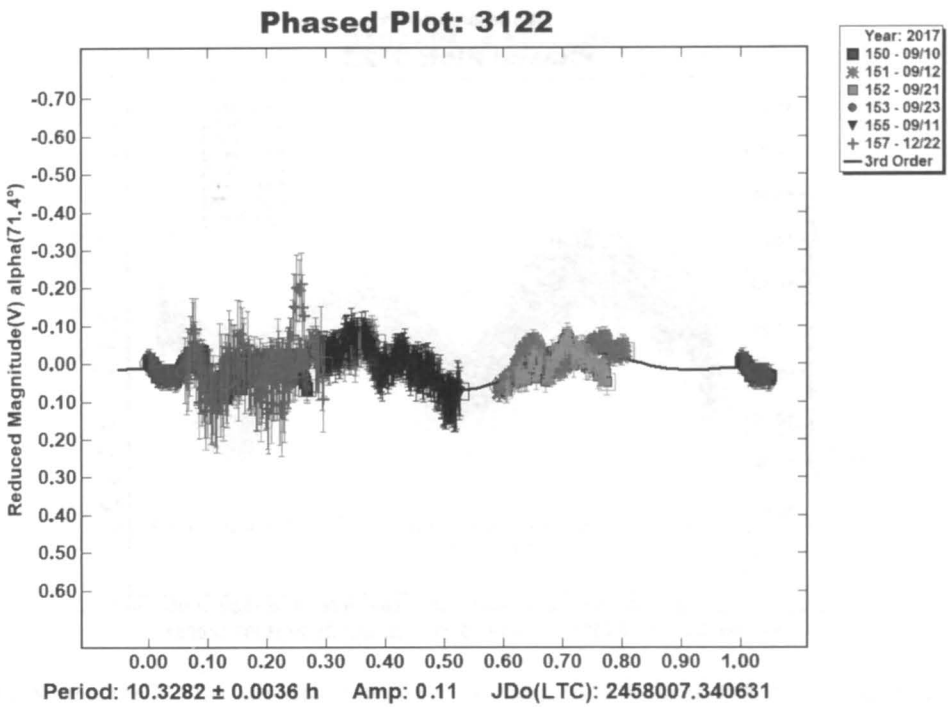

Fig. 2 – Second period of (3122) Florence.

shifted from the observations made in September. A variable synodical period will induce a time displacement when we try to fold different lightcurves on a medium period and, due to the variable rotational period, a common time of minima could not be found.

Knowing that there are two satellites around (3122) Florence gave us a reason to try and find their synodical periods in our data. We used the Dual period search option in Canopus, an algorithm based on the work of Pravec *et al.* (2006). After we have determined the main synodical period, we subtract it from the lightcurve in order to see the variations due to the satellites. We were unable to find the periods of 8 or 25 hours (periods of the satellites), but we found a second period of 10.328 ±0.0036h, a result in good agreement with the one of Warner (2016). After we subtracted the second period, we found the same synodical period that was discovered the first time and the Fourier fit of the data was much improved.

Using the maximum V magnitude for every night of observation we managed to determine the absolute magnitude (H) and the slope parameter (G) of Florence, by using H-G calculator tool in MPO Canopus, a tool based upon FAZ algorithm developed by (Harris, 1989). Our H and G estimates (13.542 ± 0.188 for H and

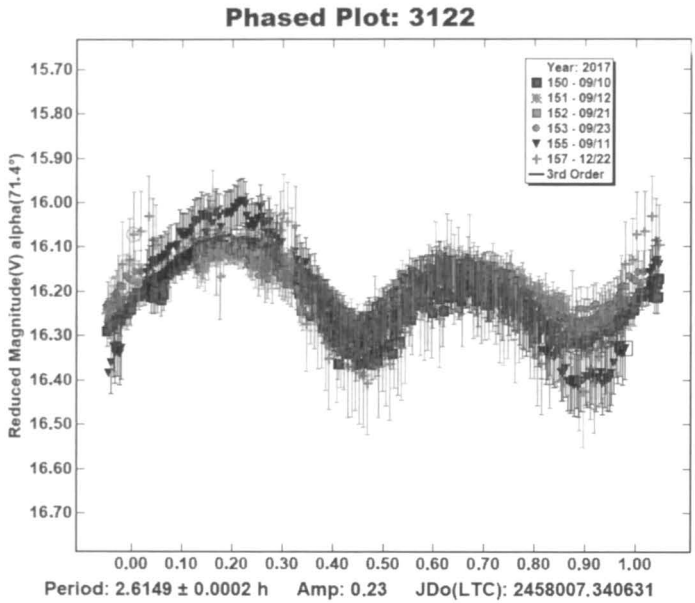

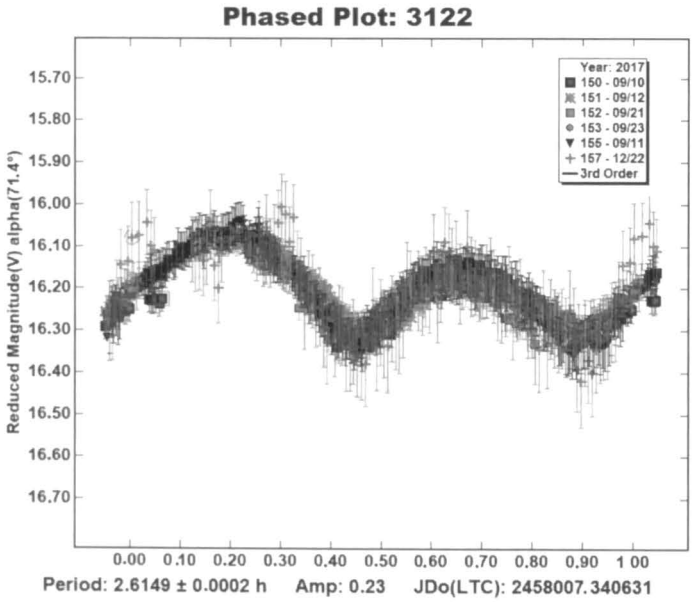

Fig. 3 – Sinodical period and Fourier fit of the data before (left) and after (right) the second period was subtracted.

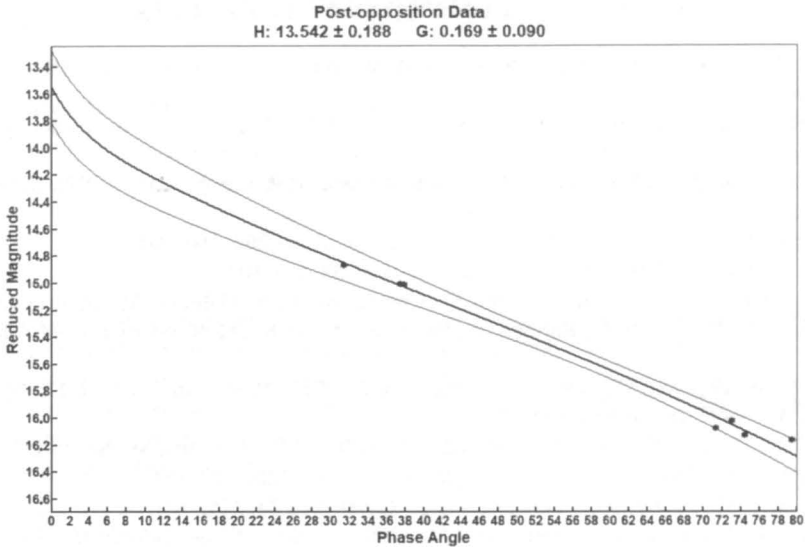

Fig. 4 – H and G plot for (3122) Florence on Johnson V magnitude system.

0.169 ± 0.09 for G) are based only on post-opposition data and should be treated with caution.

5. CONCLUSIONS

The minor planet (3122) Florence has been observed from Bucharest for nine nights, from mid September 2017 to late January 2018, just after its close approach to Earth. For this study we used data only from six nights and we found different synodical periods for every night. We were not able to find a common synodical period that fits well enough all these nights and this fact might be a hint that the minor planet has a variable synodical period. For every night a bimodal lightcurve was found, with a maximum that is higher than the other one with 0.1 magnitudes. A common synodical period of 2.6149 ± 0.003 h was found but this result should be treated with caution. We also found a second period of 10.328±0.0036h, which allowed us to improve the shape of the lightcurve. From the phase curve we determined the parameters H = 13.542 ± 0.188 and G = 0.169 ± 0.09.

Acknowledgements. This work was supported by grants of the Ministry of National Education and Scientific Research, RDI Program for Space Technology and Advanced Research - STAR, project number 513 and ARGOSS – MCI Contract No. 11 PS/2017.

REFERENCES

Binzel, R. P., Rivkin, A. S., Stuart, J. S., Harris, A. W., Bus, S. J., Burbine, T. H.: 2004, *Icarus* **170**, 259-294.

Birlan, M., Popescu, M., Irimiea, L., & Binzel, R.: 2016, AAS/Division for Planetary Sciences Meeting Abstracts #48, 325.17

de León, J., Licandro, J., Serra-Ricart, M., Pinilla-Alonso, N., & Campins, H.: 2010, *Astron. Astrophys.* , 517, A23

DeMeo, F.E., Binzel, R.P., Slivan, S.M., Bus, S.J.: 2009, *Icarus* **202**, 160-180.

Elenin, L.,Molotov, I.: 2012, *The Minor Planet Bulletin* **39**, 101-102.

Franco, L., Bacci, P. , Maestripieri, M., Baj, G., Casalnuovo, G. B., Galli, G., Marchini, A., Noschese, A., Valvasori, A., Caselli, C., Barbieri, L., Facchini, M.: 2018, *The Minor Planet Bulletin* **45**, 174-177.

Gherase, R. M., Popescu, M., Sonka, A. B., Parschiv, P.: 2017, *Romanian Astron. J.* **27**, 91.

Harris, A. W.: 1997, *Icarus* **126**, 450-454.

Harris, A.W., Young, J.W., Bowell, E., Martin, L.J., Millis, R.L., Poutanen, M., Scaltriti, F., Zappala, V., Schober, H.J., Debehogne, H., and Zeigler, K.W.: 1989, *Icarus* **77**, 171.

Harris, A. W.: 1989, *Lunar and Planetary Science Conference* **20**, 375.

Daniel A. Klinglesmith III, D.A., Hendrickx, S.: 2018, *The Minor Planet Bulletin* **45**, 61-63.

Mainzer, A., Bauer, J., Grav, T., Masiero, J., Cutri, R. M., Dailey, J., Eisenhardt, P., McMillan, R. S., Wright, E., Walker, R., Jedicke, R., Spahr, T., Tholen, D., Alles, R., Beck, R., Brandenburg, H., Conrow, T., Evans, T., Fowler, J., Jarrett, T., Marsh, K., Masci, F., McCallon, H., Wheelock, S., Wittman, M., Wyatt, P., DeBaun, E., Elliott, G., Elsbury, D., Gautier IV, T., Gomillion, S., Leisawitz, D., Maleszewski, C., Micheli, M., Wilkins, A.: 2011, *Astrophys. J.* **731.1**, 53.

*: 2016, Maxim DL software manual, `http://www.diffractionlimited.com/help/maximdl/MaxIm-DL.htm`.

Popescu, M., Birlan, M., Nedelcu, D. A.: 2012, *Astronomy & Astrophysics* **544**, 130.

Pravec, P., Scheirich, P., Kusnirák, P., Sarounova, L., Mottola, S., Hahn, G., Brown, P., Esquerdo, G., Kaiser, N., Krzeminski, Z. and Pray, D.P.: 2006, *Icarus* **181**, 63-93.

Pravec, P., Wolf, M., Sarounova, L.: 2002, `http://www.bluemountainsobservatory.com.au/asteroid/nea.html`, accessed on April 2018.

Rodrigo, O., Fornas, G., Arce, E., Mas, V., Carreño, A., Brines, P., Fornas, A., Herrero, D., Lozano, J., García, F.: 2018, *The Minor Planet Bulletin* **45**, 120-121.

Thomas, C.A., Trilling, D.E., Emery, J.P., Mueller, M., Hora, J.L., Benner, L.A.M., Bhattacharya, B., Bottke, W.F., Chesley, S., Delbó, M., Fazio, G., Harris, A.W., Mainzer, A., Mommert, M., Morbidelli, A., Penprase, B., Smith, H.A., Spahr, T.B., and Stansberry, J.A.: 2011, *The Astronomical Journal* **142**, 85.

Tomassini, A., Scardella, M., Franceschini, F., Pierri, F.: 2018, *The Minor Planet Bulletin* **45**, 11-13.

Warner 2015, B.D.: 2015, *MPO Canopus software* v10.7.0.6, Bdw Publishing, www.MinorPlanetObserver.com.

Warner, B.D.: 2016, *The Minor Planet Bulletin* **43**, 240-250.

Received on 25 May 2018

ORBIT ANALYSIS OF *GOLIAT* CUBESAT

TIBERIU OPROIU[1], MIHAI BARBOSU[2], VLAD TURCU[1], LIVIU MIRCEA[1]

[1]*Astronomical Observatory, Cluj-Napoca, Romania*
[2]*Rochester Institute of Technology, School of Mathematical Sciences, Rochester, NY, USA, E-mail: mxbsma@rit.edu*

Abstract. The *Goliat* nanosatellite was launched from Kourou on 13 February 2012 at 10:00 (UTC) by the new European launch vehicle Vega. The date of re-entry was December 31, 2014. The CubeSat weighed 1 kg and was developed at the University of Bucharest, Romania. This was Romania's first satellite. Its ballistic coefficient has been estimated on the basis of historical sets of orbital elements TLE, which covered the satellite's lifetime in orbit.

Key words: Celestial mechanics – space sciences – CubeSat.

1. INTRODUCTION

The satellite GOLIAT, having the COSPAR code number 2012-006-D, is a nanosatellite based on the American Cubesat standard, cube-shaped $10 \times 10 \times 10cm$ and weighting $1kg$ (see http://www.n2yo.com/satellite/?s=38080).

The characteristics of its orbit shortly after launch, according to RAE Table of Earth Satellites (www.satlist.nl/), were the following:

- Date of orbital determination: 2012 Feb 13.85
- a (semi-major axis) = 7254 km,
- e (orbital eccentricity) = 0.078,
- i (orbital inclination) = 69.48^o,
- h_A (apogee height) = 1441 km,
- h_P (perigee height) = 309 km
- T_N (nodal period) = 102.47 min
- ω (argument of perigee) = 44^o.

and orbital elements on December 31, 2014, the date of the re-entry, were:

- Date of orbital determination: 2014 Dec 31.69

- a (semi-major axis) = 6533 km,
- e (orbital eccentricity) = 0.002,
- i (orbital inclination) = 69.39^o,
- h_A (apogee height) = 166 km,
- h_P (perigee height) = 144 km
- T_N (nodal period) = 87.58 min
- ω (argument of perigee) = 53^o.

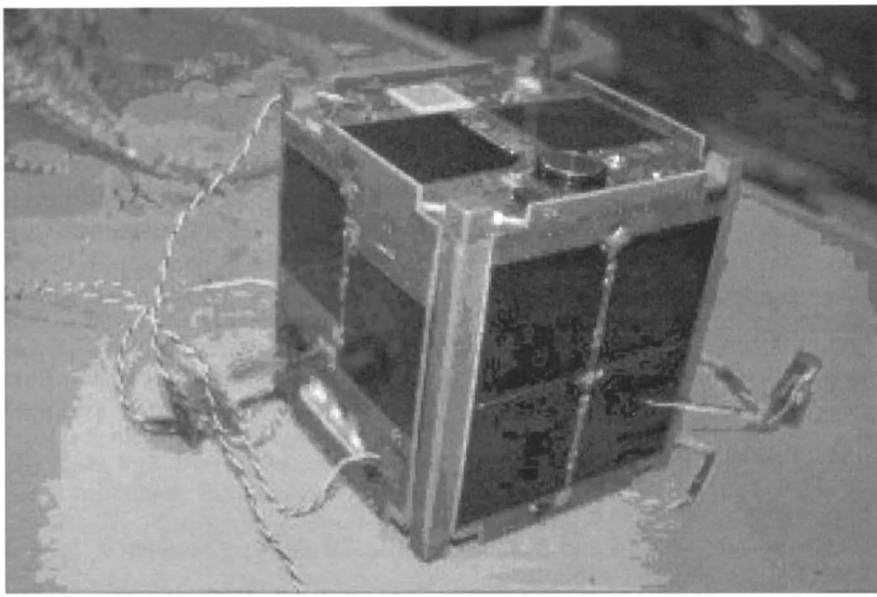

Fig. 1 – Satellite Goliat (Balan *et al.* (2009), Trusculescu *et al.* (2008)).

2. ORBITAL EVOLUTION

For the analysis of orbital evolution, we used *Two-Line Elements* (TLE). The TLE elements were obtained from the US Space Surveillance Network. The Epoch of TLEs is conventionally the time of the satellite passing through the ascending node preceding the observation.

2.1. SEMI-MAJOR AXIS

The semi-major axis was computed from TLEs using (Gaposchkin (1966)):

$$a = (\frac{\mu}{n^2})^{1/3} [1 + \frac{1}{3} \frac{J}{p^2} \sqrt{1-e^2}(-1 + \frac{3}{2} \sin^2 i)], \quad (1)$$

where

$$p = (\frac{\mu}{n^2})^{1/3}(1-e^2), \quad (2)$$

is semi-latus rectum of the mean ellipse, and

$$J = \frac{3}{2} (a_e)^2 J_2 \ (\mathrm{Mm}^2). \quad (3)$$

where J_2 is the second zonal harmonics of the Earth gravitational field ($J_2 = 1.08626 \times 10^{-05}$ and a_e is the mean equatorial radius, $a_e = 6378.14$ km.

This process represents a conversion from TLE mean-mean motion n to a semi-major axis (a) averaged with respect to the mean anomaly (Kozai (1959)).

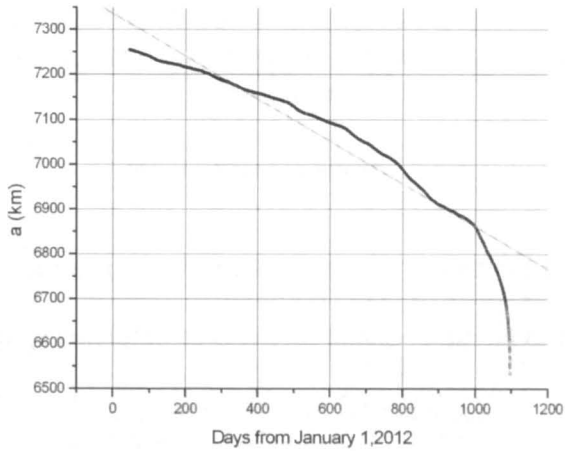

Fig. 2 – Semi-major axis a *vs.* time.

The evolution of the semi-major axis is given in Figure 2.

Through linear regression ($Y = A + B * X$), for the semi-major axis a versus time (t in days) we obtained the following results: $A = 7335.90855$ km ± 1.88616, $B = -0.47443$ km/day ± 0.00283.

2.2. APOGEE AND PERIGEE HEIGHT

The height of the perigee and apogee, respectively, are given by

$$h_P = a(1-e) - a_e(1-0.00335\sin^2\omega\sin^2 i),$$
$$h_A = a(1+e) - a_e(1-0.00335\sin^2\omega\sin^2 i), \tag{4}$$

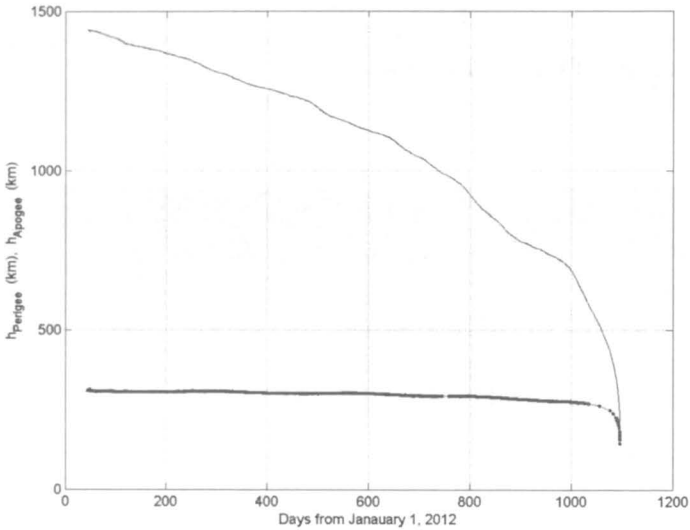

Fig. 3 – Apogee and perigee height.

2.3. ECCENTRICITY AND ARGUMENT OF PERIGEE

The trajectory in the (q,k)- plane describes an unfolding spiral.

2.4. SPACE WEATHER CONDITIONS

In the current Solar cycle 24 and in the first months of the 2012 year, there have been a few periods of time of intense space weather activity:

- large sunspots regions,
- intense solar flares,
- particle events,

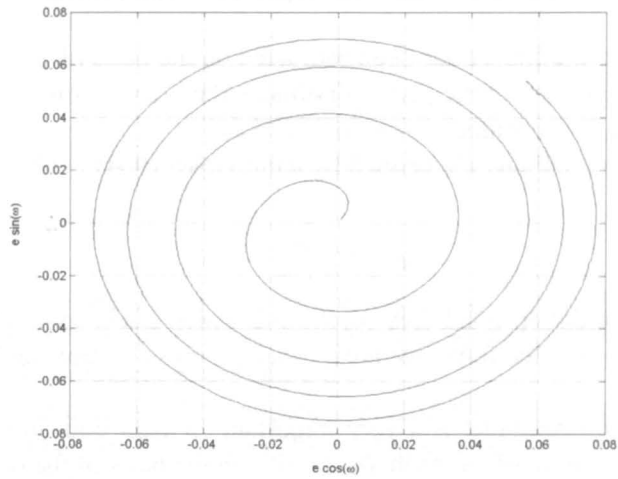

Fig. 4 – Evolution of the eccentricity and argument of the perigee - via ($q = e\cos\omega$, $k = e\sin\omega$).

- geomagnetic disturbances.

For example, on March 7th 2012 a storm started from CME, generated by the X1.1 flare on March 5th; this was a G2-type storm. The solar wind velocity rapidly increased from 500 to 700 km/s, with a peak value of 800 km/s. Note that the geomagnetic indexes D_{st} and K_p are widely used in space weather forecasts.

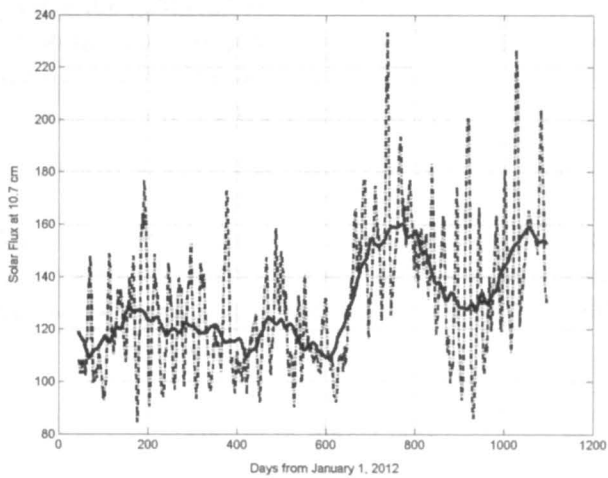

Fig. 5 – Solar Flux at 10.7 cm: here, the dash-dot line represents the observed solar flux and the solid line represents an 81-day averaged solar flux.

3. ESTIMATION OF THE BALLISTIC COEFFICIENT

The ballistic coefficient has been estimated on the basis of 2310 sets of orbital elements, which covered a time period of almost 1062 days, from 13 February 2012 (55970 MJD) to 31 December 2014 (57022 MJD).

The ballistic coefficient is defined by King-Hele (1964):

$$\delta = C_D \frac{A}{m}, \tag{5}$$

where C_D is a non-dimensional drag coefficient, which can be assumed constant and taken usually 2.2. A is the reference area, usually a cross-section, and m is the mass of the satellite.

The ballistic coefficient is a very important element both in cosmic ballistic and in the determination of atmospheric density on the basis of the orbital drag data. However, it is difficult to estimate an exact value of δ at a given moment. The incertitude which appears in the determination of this parameter has the following causes:

- the inexact knowledge of A (especially for a satellite with an irregular shape and an uncontrollable spin motion),
- the possible variations of the drag coefficient C_D,
- the possible dependence of δ of solar activity.

For the determination of the ballistic coefficient there are several methods (see for instance, Goral (1972), Goral (1968)), based on the estimation of the variation (dissipation) of the total energy of the satellite due to aerodynamic drag. We assumed that the variation of the total satellite energy (per unit of mass) decreases from E to E_1 during K revolutions. Then, the variation per one revolution can be estimated as:

$$\Delta E = \frac{E_1 - E}{K}. \tag{6}$$

On the other hand, the ΔE variation of energy (per one revolution and mass unit) can be estimated on the basis of the mechanical work (per revolution) done by drag, on the satellite, over the entire length l of the orbit; here we used the following formula:

$$\Delta E = \frac{1}{2}\delta \int_0^l \rho V^2 \mathrm{d}s, \tag{7}$$

where ρ, in (kg/m^3), is the air density calculated with the $CIRA72$ atmosphere model as a function of solar and geomagnetic activity, local time, day of the year, altitude and latitude (Cârşmaru and Oproiu (1993), Cârşmaru and Oproiu (1994)).

Taking into account the fact that $\mathrm{d}s = V\mathrm{d}t$ and $\mathrm{d}t = (r^2/\sqrt{\mu p})\mathrm{d}u$, Eq. (7) can be written as:

$$\Delta E = \frac{1}{2}\delta \frac{J}{C}, \tag{8}$$

where J, using Goral's notation (Goral (1968)), has the form:

$$J = \int_0^{2\pi} \rho\, V^3 r^2 \mathrm{d}u, \tag{9}$$

with $C = \sqrt{\mu p}$ - the angular momentum constant (of areas), μ - the Earth's gravitational parameter, r - the radius vector, V - the velocity of the satellite, p - semi-latus rectum and u - the argument of the latitude.

The above integral can be computed numerically, by taking into account that the density ρ can be found from the $CIRA$ 72 model, while V and r ar determined from the formulas of the perturbed motion. From Eq. (8) we have

$$\delta = 2\,\Delta E \frac{C}{J}, \tag{10}$$

In the paper (Goral (1968)), it is suggested that relation (8) could be used for the determination of an average value of the aerodynamic drag parameter:

$$\overline{\delta} = 2\,\overline{\Delta E}\,(\frac{C}{Jn})_{mean}, \tag{11}$$

where $\overline{\Delta E}$ is the daily decrease of the total energy (per mass unit) due to air drag, the index $"mean"$ signifies the average value of the denominator over the considered time interval, and n is the mean motion of the satellite.

Using the information about the TLE-orbital elements of GOLIAT, first we determined the quantities:

$$t_i\,(in\ MJD\ days),\ E_i,\ (C/Jn)_i,\ i = \overline{1,N}$$

The total energy for the epochs of the orbital elements has been determined from $E = -\mu/(2a)$, while the density ρ has been estimated by means of the $CIRA-1972$ model.

For every two consecutive epochs t_i, t_{i+1}, with $i = \overline{1,N-1}$, the following average values have been computed:

$$\begin{cases} \overline{t_i} = (t_i + t_{i+1})/2, \\ \overline{\Delta E_i} = (E_{i+1} - E_i)/(t_{i+1} - t_i), \\ (Jn/C)_{mean,i} = ((Jn/C)_{mean,i} + (Jn/C)_{mean,i+1})/2 \end{cases}$$

With these values, using Eq. (11), we determined the mean value δ for each time interval $[t_i, t_{i+1}]$:

$$\overline{\delta_i} = 2\,\overline{\Delta E_i}\,(\frac{Jn}{C})_{mean,i},\ i = \overline{1, N-1}, \tag{12}$$

corresponding to $\overline{t_i}$.

A mean value for the whole time interval covered by the sets of TLE orbital elements was determined from:

$$\overline{\delta}_{mean} = \sum_{i=1}^{N-1} \frac{\overline{\delta_i}}{N-1}, \tag{13}$$

with $r.m.s$:

$$\sigma^2 = \frac{\sum_{i=1}^{N-1}(\overline{\delta}_i - \overline{\delta}_{mean})^2}{(N-1)(N-2)}. \tag{14}$$

Individual values of the ballistic coefficient, computed from the TLEs, are given in Figure 6.

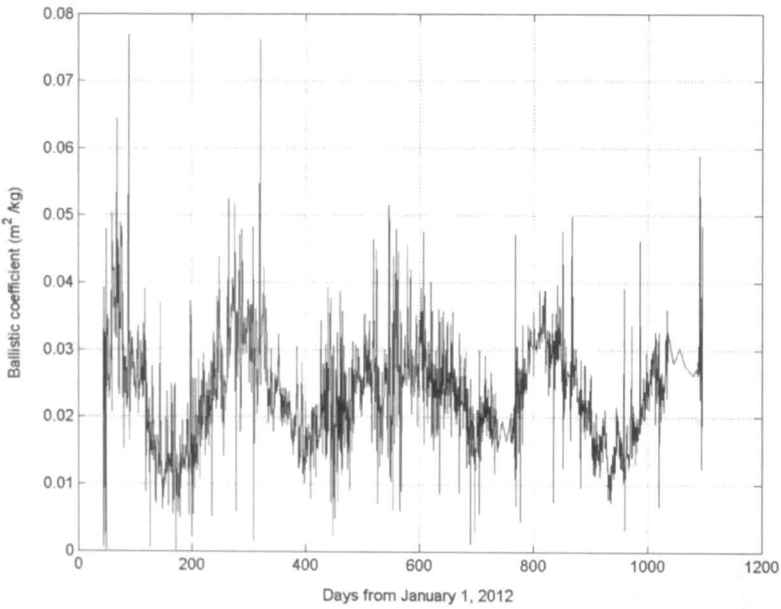

Fig. 6 – Ballistic coefficient.

The mean value for the whole time interval covered by the TLE orbital elements is:

$$\overline{\delta}_{mean} = 0.02461 \mathrm{m}^2/\mathrm{kg}$$

with the standard deviation /root mean square (r.m.s) $= \pm 0.01934$.

If in Eq. (5) we take $C_D = 2.2$, $A = 0.01 \mathrm{m}^2$ (minimum cross-section area) and $m = 1$ kg we obtain

$$\delta = 0.022 \mathrm{m}^2/\mathrm{kg}$$

If we take $A = 0.015 \mathrm{m}^2$ (mean cross-section area), we get

$$\delta = 0.033 \mathrm{m}^2/\mathrm{kg}$$

These values are in good agreement with the value, obtained from the TLE orbital elements.

REFERENCES

M. Balan *et al.*:2009, *GOLIAT Space Mission: Earth Observation and Near Earth Environment Monitoring Using NanoSatellites*,in 60th IAC B4. 13th Small Satellite Missions Symposium, Daejon, Korea.

Cârşmaru, M., Oproiu, T.: 1993, *Rom. Astron. J.*, **3**, 2, 181.

Cârşmaru, M., Oproiu, T.: 1994, *Rom. Astron. J.*, **4**, 2, 201.

CIRA-72, *COSPAR International Reference Atmosphere 1972*, Academie Verlag, Berlin, 1972

Gaposchkin, E. M.: 1966, *SAO Special Report* **200**,Volume 1, 77.

Goral, W.: 1968, *Artificial Satellites* **4**, No. 1, 16.

Goral, W.: 1972, *Artificial Satellites* **7**, No. 2, 123.

King-Hele, D.G.: 1964, *Theory of Satellite Orbits in an Atmosphere*, Butther- worths, London.

Kozai, Y.: 1959, *Astron. Journ.* **64**, 367.

Trusculescu, M., Balan, M., Dragasanu, C., Pandele, A. and Piso, M.-I.: 2008, *Nanosatellites: 2008, The Tool for Earth Observation and Near Earth Environment Monitoring*, Proceedings of the 59th International Astronautical. Congress, 1995-6258, Glasgow, Scotland, October 2008 (www.intechopen.com/download/pdf/27165)

Received on 30 May 2018

TIMELIKE GEODESICS AROUND A GHGMS BLACK HOLE

CRISTINA BLAGA[1], PAUL A. BLAGA[2]

[1] *Babeş-Bolyai University, Faculty of Mathematics and Computer Science*
Kogălniceanu Street 1, 600410, Cluj-Napoca, Romania
Email: cpblaga@math.ubbcluj.ro
[2] *Babeş-Bolyai University, Faculty of Mathematics and Computer Science*
Kogălniceanu Street 1, 600410, Cluj-Napoca, Romania
Email: pablaga@cs.ubbcluj.ro

Abstract. In this note we take a dynamical systems approach to the equations of motion of a free test particle moving around a spherically symmetric static dilaton black hole, written in the Einstein frame. The equations of motion are obtained using the Euler-Lagrange formalism. Using the first integrals of motion, we reach the conclusion that the free test particles are moving in a plane, named *plane of motion*. In it we analyze the existence and nature of the equilibrium points and compare the behavior of free test particles near the equilibrium points using the dynamics systems approach. The study revealed that in the exact phase-plane exist distinct regions of motion, separated through a curve named *separatrix*. In the end we obtained a relation between the parameters describing the black hole and the free test particle that holds on a parabolic separatrix.

Key words: General Relativity – Gravitation – Black holes.

1. INTRODUCTION

In classical theory of general relativity, the spacetime near a charged black hole is described using the Reissner-Nordstrøm metric.

At the end of the eighties, especially after the publications of the classical monograph Green, Schwarz and Witten (1987), there was much interest in the investigation of black holes within string theory. The metric we use in this paper is a solution of the Einstein-Maxwell-dilaton equations, based on an action containing, beside gravity, a scalar field, called *dilaton*, and the electromagnetic field, coupled to the graviton. More specifically, the action has the form

$$S = \frac{1}{16\pi}\int \mathrm{d}^4x\sqrt{-g}\left[R - 2(\nabla\Phi)^2 - e^{-2\Phi}F_{\mu\nu}F^{\mu\nu}\right] \tag{1}$$

where g is the determinant of the metric, R is the scalar curvature, Φ is the dilaton field, while $F_{\mu\nu}$ is the strength of the electromagnetic field.

The action (1) corresponds to the low-energy limit of the action for the heterotic string. It is written in the so-called *Einstein frame*. In this approach, as one can see easily, the action is, simply, the action for pure gravity, with an energy-momentum defined by the electromagnetic fied and the dilaton (Einstein-Hilbert action). There

is, also, an alternative approach, where the action is written in the so-called *string frame*. In this approach, the metric from the action (1) is replaced by another metric, conformally equivalent to the metric from the Einstein frame. In this paper, we shall work exclusively in the Einstein frame and postpone for another paper the discussion of the string frame. We notice, nevertheless, that the spacetimes obtained from the two actions are not isometric, they are just conformally equivalent. For more information about the two frames, see Casadio and Harms (1999) or the monograph Frolov, Novikov (1998).

The first static spherically symetric black hole solution in dilaton gravity was found by Gibbons and Maeda (1988) and, three years later, independently, by Garfinkle, Horowitz and Strominger (1991). This solution, known as Gibbons–Maeda–Garfinkle–Horowitz–Strominger (GMGHS) black hole, was later reconstructed by Horowitz (1993), through a Harrison-like transformation, starting from the Schwarzschild solution.

In this article we perform a phase-plane analysis of the equations of motion of a free test particle around a GMGHS black hole. In section 2 we obtain the second order nonlinear equation. The phase-plane analysis for the corresponding two-dimensional system of first order equations of motion is performed in section 3. We obtain the equilibrium points and determine their nature. In the following section we represent several phase-plane diagrams and analyze the separatrix, curve which divide the phase-plane into distinct regions of motion.

2. EQUATIONS OF MOTION

The equations of motion of a free test particle moving around a GMGHS black hole are derived from the line element:

$$ds^2 = -\left(1-\frac{2M}{r}\right)dt^2 + \frac{dr^2}{\left(1-\frac{2M}{r}\right)} + r\left(r-\frac{Q^2}{M}\right)d\theta^2 + \sin^2\theta\, d\varphi^2) \qquad (2)$$

where Q is related to the electrical charge of the black hole and M to its mass. For $Q^2 < 2M^2$, the black hole has an events horizon. If $Q^2 = 2M^2$, the solution describes a naked singularity. The latter case is known as extremal GMGHS black hole.

The Lagrangian corresponding to the line element (2) is

$$2\mathcal{L} = -\left(1-\frac{2M}{r}\right)\dot{t}^2 + \frac{\dot{r}^2}{\left(1-\frac{2M}{r}\right)} + r\left(r-\frac{Q^2}{M}\right)\left(\dot{\theta}^2 + \sin^2\theta\,\dot{\varphi}^2\right) \qquad (3)$$

where dot means differentiation with respect to τ - an affine parameter along the geodesic. The parameter is chosen such that $2\mathcal{L} = -1$ along a timelike geodesics, $2\mathcal{L} = 0$ along a null geodesics and $2\mathcal{L} = 1$ along a spacelike geodesics.

The equations of motion of a free test particle are the Euler-Lagrange equations

of the Lagrangian (3) (see Chandrasekhar (1983)). The coordinates t and φ do not appear explicitly in (3), they are cyclic coordinates. Thus, one finds two integrals of motion. The first is derived from $\partial L/\partial t = 0$, named the energy integral

$$\left(1 - \frac{2M}{r}\right)\dot{t} = E \tag{4}$$

where E is a real constant – the total energy of the particle. The second integral, obtained from $\partial L/\partial\varphi = 0$,

$$2\sin^2\theta \cdot r\left(r - \frac{Q^2}{M}\right)\dot{\varphi} = \text{constant} \tag{5}$$

is the angular momentum integral.

The Euler-Lagrange equation for θ is

$$\frac{\mathrm{d}}{\mathrm{d}\tau}\left[r\left(r - \frac{Q^2}{M}\right)\dot{\theta}\right] = r\left(r - \frac{Q^2}{M}\right)\sin\theta\cos\theta \cdot \dot{\varphi}^2. \tag{6}$$

If $\theta = \pi/2$, when $\dot{\theta} = 0$, then from (6) $\ddot{\theta} = 0$ and $\theta = \pi/2$ along the geodesic. And, thus, if at the beginning the free test particle lies in the equatorial plane and $\dot{\theta} = 0$, its motion is confined in the equatorial plane. The motion is planar like in the Schwarzschild spacetime or in the Newtonian gravitational field.

If $\theta = \pi/2$, the angular momentum integral (5) leads us to

$$r\left(r - \frac{Q^2}{M}\right)\dot{\varphi} = L \tag{7}$$

where the real constant L is the angular momentum about an axis normal at the plane in which the motion took place.

Using the integrals of motion in the constancy of the Lagrangian we get a non-linear first order differential equation in r

$$\left(\frac{\mathrm{d}r}{\mathrm{d}\tau}\right)^2 + \left(1 - \frac{2M}{r}\right)\left(\frac{L^2}{r\left(r - \frac{Q^2}{M}\right)} - \epsilon\right) = E^2 \tag{8}$$

where $\epsilon = -1$ for timelike geodesics, $\epsilon = 0$ for null geodesics and $\epsilon = +1$ for spacelike geodesics. In this article we are interested in the motion of free test particles around a GMGHS black hole, therefore we consider $\epsilon = -1$.

In analogy with the motion of a particle in the Newtonian gravitational field, the second term from the left-hand side of the relation (8) is named *effective potential*. For the timelike geodesics it is given by

$$V = \left(1 - \frac{2M}{r}\right)\left(\frac{L^2}{r\left(r - \frac{Q^2}{M}\right)} + 1\right). \tag{9}$$

3. PHASE-PLANE ANALYSIS

Denoting $x = r_S/r$, where $r_S = 2M$ is the Schwarzschild radius, the relation (8) becomes

$$\left(\frac{\mathrm{d}x}{\mathrm{d}\varphi}\right)^2 = 2\sigma(1-bx)^2\left(E^2-\Lambda\right)-(1-bx)\Lambda x^2 \tag{10}$$

where

$$\sigma = \frac{1}{2}\left(\frac{r_S}{L}\right)^2, \quad b = \frac{Q^2}{2M^2} \quad \text{and} \quad \Lambda = 1-x \tag{11}$$

We note that $\sigma > 0$, $b \in [0,1]$, $b = 0$ is the Schwarzschild black hole, $b = 1$ an extremal GMGHS black hole and outside the black hole $x \in [0,1]$.

We seek the solution $x = x(\varphi)$. Differentiating the equation (10), with respect to φ, we get

$$\frac{\mathrm{d}x}{\mathrm{d}\varphi} = 0 \tag{12}$$

or

$$\frac{\mathrm{d}^2x}{\mathrm{d}\varphi^2} = a_3x^3 + a_2x^2 + a_1x + a_0 \tag{13}$$

with

$$\begin{aligned} a_3 &= -2b, & a_2 &= \frac{3}{2}\left(2\sigma b^2 + b + 1\right), \\ a_1 &= 2\sigma b^2(E^2-1) - 4\sigma b - 1, & a_0 &= 2\sigma b(1-E^2) + \sigma. \end{aligned} \tag{14}$$

The equation (12) has the the particular solution $x =$ constant or r is constant, *i.e.* circular orbits, which were discussed in Blaga (2013). In this article, we study the equation (13) using the dynamical systems approach (see Jordan and Smith (1999) or Strogatz (1994)).

3.1. EQUILIBRIUM POINTS

We introduce the variable $y = \mathrm{d}x/\mathrm{d}\varphi$, to transform the second order, nonlinear, inhomogeneous differential equation (13) into a first order differential system of equations

$$\begin{cases} x' = y \\ y' = a_3x^3 + a_2x^2 + a_1x + a_0 \end{cases} \tag{15}$$

where prime denotes the differentiation with respect to φ and a_i, $i \in \{0,1,2,3\}$ are the coefficients of equation (13), given by (14).

The equilibrium points of the system (15) are given by $x' = y' = 0$. To find them, we solve simultaneously the equations for x and y. The equation $x' = 0$ has the

solution $y^\star = 0$. If we write E^2 in terms of x, σ and b from (10) for $\mathrm{d}x/\mathrm{d}\varphi = x' = 0$, we get

$$E^2 = (1-x)\left[1 + \frac{x^2}{2\sigma(1-bx)}\right] \tag{16}$$

and replacing (16) in the second equation of the system (15), we obtain

$$y' = -bx^3 + \left(\sigma b^2 + \frac{1}{2}b + \frac{3}{2}\right)x^2 - (2\sigma b + 1)x + \sigma. \tag{17}$$

From $y' = 0$, we get a cubic equation in x, with coefficients depending on b and σ. The leading coefficient is equal to b. If $b = 0$, (17) becomes a quadratic equation in x. The case $b = 0$, represents a Schwarzschild black hole and it was analyzed, by using dynamical systems, by Dean (1999).

If $b \neq 0$, the abscissae of the equilibrium points are the roots of the cubic equation $y' = 0$. Using Cardan's formula (see for example Kurosh (1980)) these are

$$x_1^\star = d + u + v,\ x_2^\star = d - \frac{u+v}{2} + \frac{u-v}{2}\sqrt{-3},\ x_3^\star = d - \frac{u+v}{2} - \frac{u-v}{2}\sqrt{-3} \tag{18}$$

where

$$d = \frac{2\sigma b^2 + b + 3}{6b},\ u = \sqrt[3]{-\frac{q}{2} + \sqrt{\Delta}},\ v = \sqrt[3]{-\frac{q}{2} - \sqrt{\Delta}},\ \Delta = \frac{q^2}{4} + \frac{p^3}{27} \tag{19}$$

and

$$p = -\frac{w^2}{12b^2},\ q = -\frac{w^3 + 54(1-b)}{108b^3},\ w = 2\sigma b^2 + b - 3. \tag{20}$$

The nature of roots of the cubic equation $y' = 0$ depends on the sign of the discriminant Δ, which, after some algebra, becomes

$$\Delta = \frac{(1-b)[8b^4\sigma^3 + 12b^2(b-3)\sigma^2 + 6(b-3)^2\sigma + b - 9]}{432b^4}. \tag{21}$$

If $\Delta > 0$ the equation has one real and two conjugate complex roots, if $\Delta = 0$ it has three real roots, at least two equal and if $\Delta < 0$ it has three distinct, real roots.

In our analysis, $0 < b \leq 1$ and $\sigma > 0$, therefore the sign of discriminant is the sign of second factor from the numerator. We consider it as a fourth order polynomial in b, with real coefficients, depending on the parameter σ, denoted with $h(b,\sigma)$. We can write it as

$$h(b,\sigma) = 8\sigma^3 b^4 + 12\sigma^2 b^3 - 6\sigma(6\sigma - 1)b^2 + (1 - 36\sigma)b + 9(6\sigma - 1). \tag{22}$$

with $h(0,\sigma) = 9(6\sigma - 1)$ and $h(1,\sigma) = 8(\sigma - 1)^3$. Using the Sturm method (see for example Kurosh (1980)) we establish the number of roots of this polynomial for $b \in [0,1]$ and $\sigma > 0$. In the Sturm's sequence, the first term is $h(b,\sigma)$. The second term is the first derivative of $h(b,\sigma)$ with respect to b,

$$h'(b,\sigma) = 32\sigma^3 b^3 + 36\sigma^2 b^2 - 12\sigma(6\sigma - 1)b + (1 - 36\sigma). \tag{23}$$

Table 1

The number of sign changes for $b = 0$ and $\sigma \geq 0$

σ	0		1/36		0.12		1/6		1.39	
h	-	-	-	-	-	-	0	+	+	+
h'	+	+	0	-	-	-	-	-	-	-
h_2	+	+	+	+	0	-	-	-	-	-
h_3	0	+	+	+	+	+	+	+	+	+
h_4	-	-	-	-	-	-	-	-	0	+
Sign changes		2		2		2		3		2

The third term is the reminder after dividing h by h', with reversed sign,

$$h_2(b,\sigma) = \frac{3}{32\sigma}[192b^2\sigma^3 + 4b^2\sigma^2 + 4b\sigma(54b+1) - 576\sigma^2 + 60\sigma + 1] = \frac{3}{32\sigma}h_{2s}, \tag{24}$$

followed by the reminder after dividing h' by h_{2s}, with reversed sign,

$$h_3(b,\sigma) = \frac{576\sigma^2}{(48\sigma+1)^2}[-4\sigma(24\sigma+1)b + 144\sigma + 1] = \frac{576\sigma^2}{(48\sigma+1)^2}h_{3s} \tag{25}$$

and the reminder after dividing h_{2s} by h_{3s}, with reversed sign,

$$h_4(b,\sigma) = \frac{9(48\sigma+1)^2}{4(24\sigma+1)^2}(64\sigma^2 - 88\sigma - 1). \tag{26}$$

During division process we have multiplied and divided by arbitrary positive quantities, because only the sign of the reminder matters in the Sturm method.

The change of sign for these polynomials if $b \in \{0,1\}$ and $\sigma \geq 0$ is given in Table 1 and Tabel 2. If b goes from 0 to 1, the Sturm sequence loses one change in sign if $\sigma \in [1/6,1]$, therefore we conclude that $h(b,\sigma) = 0$ has one root in the interval $b \in [0,1]$ for $\sigma \in [1/6,1]$. And so, if $b \in [0,1]$ and $\sigma > 0$ then

I. for $0 < \sigma \leq 1/6$, then $\forall b \in [0,1], h(\sigma,b) < 0$,

II. for $1/6 < \sigma < 1$, $\exists \bar{b} \in [0,1]$ so that $h(\sigma,\bar{b}) = 0$ and

   a. if $b \in [0,\bar{b})$ then $h(\sigma,b) > 0$ or

   b. if $b = \bar{b}$ then $h(\sigma,\bar{b}) = 0$ or

   c. if $b \in (\bar{b},1]$ then $h(\sigma,b) < 0$,

III. for $\sigma \geq 1$ then $h(\sigma,b) > 0$.

We recall that the number of roots of the equation $y' = 0$, depends on the sign of the discriminant Δ, which is the same with the sign of $h(\sigma,b)$. The roots of the cubic equation $y' = 0$ are the abscissae of the equilibrium points of the system (27). The

Table 2

The number of sign changes for $b = 1$ and $\sigma \geq 0$

σ	0		0.04		0.22		1		1.39		1.47		1.59		1.65	
h	-	-	-	-	-	-	0	+	+	+	+	+	+	+	+	+
h'	+	+	0	-	-	-	-	-	-	-	-	-	0	+	+	+
h_2	+	+	+	+	0	-	-	-	-	-	-	-	-	-	0	+
h_3	0	+	+	+	+	+	+	+	+	+	0	-	-	-	-	-
h_4	-	-	-	-	-	-	-	-	0	+	+	+	+	+	+	+
Sign changes		2		2		2		3		2		2		2		2

ordinates vanish for all the equilibrium points. Therefore, there are: three equilibrium points in the cases I and II.c, two equilibrium points for II.b and one equilibrium point for II.a and III. In the case II.b, one root of the equation $\Delta = 0$ is a double root and the corresponding equilibrium point is a cusp.

Remark 1 . *The equilibrium points of the system (15) are the extremal points of the effective potential (9).*

The function (9) has always a minimum point, inside the events horizon (see Blaga (2013)). If V admits three extremal points, the other two are outside the events horizon, one is a minimum and the other a maximum. If there are two extremal points, the point outside events horizon is an inflection point for the potential.

3.2. LINEAR STABILITY ANALYSIS

A classification of the equilibrium points could be obtained using the linear stability analysis. First, we expand in Taylor series the right hand side of the equations

$$\begin{cases} x' = y \\ y' = -bx^3 + \left(\sigma b^2 + \frac{1}{2}b + \frac{3}{2}\right)x^2 - (2\sigma b + 1)x + \sigma \end{cases} \tag{27}$$

about the fixed points, in small parameters $\delta x = x - x^\star$ and $\delta y = y - y^\star$. Dropping the second order terms, we get the first order linear equations near the equilibrium point $(x^\star, y^\star)$

$$\begin{cases} \delta x' = \delta y \\ \delta y' = \left[-3bx^{\star 2} + (2\sigma b^2 + b + 3)x^\star - 2\sigma b - 1\right]\delta x. \end{cases} \tag{28}$$

The general solution of the system (28) is an exponential. The nature of equilibrium points of the linearized system (28), depends on the eigenvalues of matrix

$$A = \begin{pmatrix} 0 & 1 \\ -(1 - bx^\star)(2\sigma b + 1 - 3x^\star) & 0 \end{pmatrix}, \tag{29}$$

which are

$$\lambda_{1,2} = \frac{1}{2}\left(\tau \pm \sqrt{\tau^2 - 4D}\right) \tag{30}$$

where τ is the trace of the matrix A and D its determinant. The trace of the matrix $\tau = 0$ and its determinant is

$$D = (1 - bx^*)(2\sigma b + 1 - 3x^*). \tag{31}$$

Therefore, the eigenvalues of matrix A are

$$\lambda_{1,2} = \pm\sqrt{-(1 - bx^*)(2\sigma b + 1 - 3x^*)}. \tag{32}$$

If $D < 0$, the eigenvalues are real numbers, with opposite sign and the equilibrium point is an unstable saddle. Its stability is not affected by small nonlinear terms. If $D > 0$, the eigenvalues are purely imaginary and the fixed point is a center. The orbits around it are ellipses. Thus, we conclude that, among the solutions of nonlinear system (27), one can find precessing ellipses.

Having in mind that if the equilibrium point is outside the events horizon, its abscissa $x^* < 1$, and the sign of D is the sign of second factor from (31). It is easy to check that if $x^* > 1$, for $b \in [0,1]$ and $\sigma > 0$, both factors from (31) are negative and $D > 0$. Therefore, the equilibrium point, situated inside the events horizon, is a center.

In the end, let us recall that if the dynamical system is conservative, *i.e* admits a function that is constant on trajectories, then the equilibrium points coincide with the extremal points of that function (Jordan and Smith, 1999). In our case the constant function is the effective potential, therefore the equilibrium points are minima or maxima of V. A minimum point of the potential is a center, a maximum point is a saddle point. An inflection point is a cusp. Based on these observations and the study of effective potential V done in Blaga (2013), we can conclude that if the system (15) admits three equilibrium points, two are centers and one is a saddle point. If there are only two equilibrium points, one is a cusp and the other is a center. Outside the events horizon is the cusp, obtained through the merging of a center and the saddle point.

3.3. PHASE PLANE DIAGRAM

Using the linear stability analysis we obtain information about the behavior of the solution near the equilibrium points. The global features of the orbits around the black hole are revealed by the phase plane diagram for the nonlinear system (15). The phase paths satisfy the separable differential equation

$$\frac{dy}{dx} = \frac{a_3x^3 + a_2x^2 + a_1x + a_0}{y}, \tag{33}$$

where a_i, $i = \overline{0,3}$ are given by (14), which give us, through integration, the level curves

$$y^2 = \frac{1}{2}a_3x^4 + \frac{2}{3}a_2x^3 + a_1x^2 + 2a_0x + C, \tag{34}$$

where $C = 2\sigma(E^2 - 1)$ according to the equation (10). A complete study of the level curves for $b = 0$, a Schwarzschild black hole, was done by Dean (1999).

In Figure 1 we have represented the phase-plane diagram for different values of the parameters σ and b. In the first plot from Figure 1 we sketched the exact phase plane diagram for a black hole with $\sigma = 1/7$ and $b = 1/2$, for different values of energy, outside the events horizon. In this case, representative for the case I, $\sigma \leq 1/6$, from section 3.1, there are always three equilibrium points. The homoclinic path which joins the saddle point $x_2^\star$ to itself, named *separatrix*, is plotted with dashed line in Figure 1. This phase path gives a graphic representation of the relation between black hole, angular momentum and energy on the unstable circular orbit and separates distinct regions in the phase plane. Inside it, is located the equilibrium point $x_1^\star$ – a node for the linearized system (28). The third equilibrium point, $x_3^\star$ (a node), is inside the events horizon.

The rest of the plots from Figure 1 contain examples for the case II: $1/6 < \sigma < 1$, from section 3.1. We choose $\sigma = 1/5$, for which $\bar{b} = 0.289$, therefore we have considered $b \in \{1/5, 0.289, 1/2\}$. For $b = 1/5$, Figure 1b there is only an equilibrium point, inside events horizon. In Figure 1c, $b = \bar{b} = 0.289$, and the equilibrium points outside events horizon coincides, the point $x_1^\star = x_2^\star$ being a cusp. For $b = 1/2$, Figure 1d, there are three equilibrium points, two of them outside the horizon. If $\sigma \geq 1$, case III in section 3.1, the phase portrait looks like that from Figure 1b, because in that case, the only equilibrium point of the system (27) is inside the events horizon.

We rewrite the terms from the right hand side of the level curve (34) like

$$y^2 = 2\sigma(1 - bx)^2(E^2 - 1 + x) - (1 - bx)(1 - x)x^2 \tag{35}$$

to analyze the intersection of the separatrix with the Oy axis. If $x = 0$ in (35), we get $y^2 = 2\sigma(E^2 - 1)$ and recalling that $\sigma > 0$, we obtain that the separatrix intersect the Oy axis if and only if $E^2 \geq 1$, E being the energy of the test particle for the unstable circular orbit.

If $x = 0$, r goes to infinity, thus if the separatrix cuts the Oy axis, the motion is unbounded. If $E^2 = 1$, the orbit is a parabola, and if $E^2 > 1$ it is a segment of hyperbola. These results are in good agreement with the numerical investigation performed by Olivares and Villanueva (2013) and Blaga (2015).

If the separatrix is a parabolic orbit, $E^2 = 1$, the level curve (35) becomes

$$y^2 = x(1 - bx)[x^2 - (2\sigma b + 1)x + 2\sigma], \tag{36}$$

and it should go through the points $(0,0)$ and $(x_2^\star, 0)$. Thus, among the roots of the

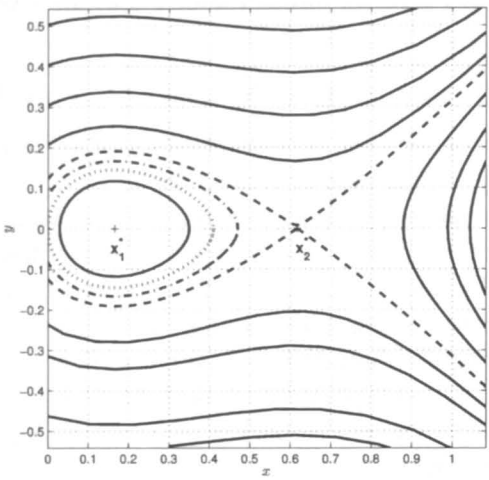

(a) $\sigma = 1/7$ and $b = 1/2$

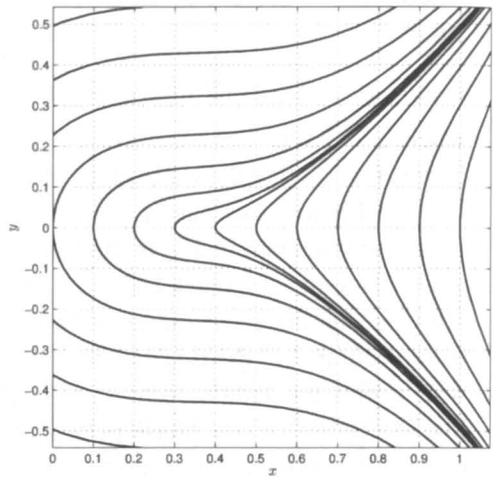

(b) $\sigma = 1/5$ and $b = 1/5$

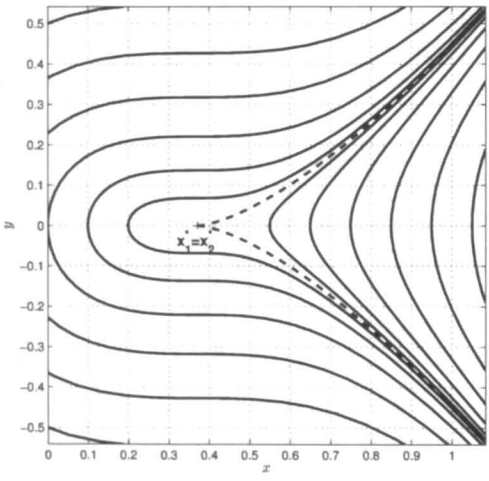

(c) $\sigma = 1/5$ and $b = \bar{b} = 0.289$

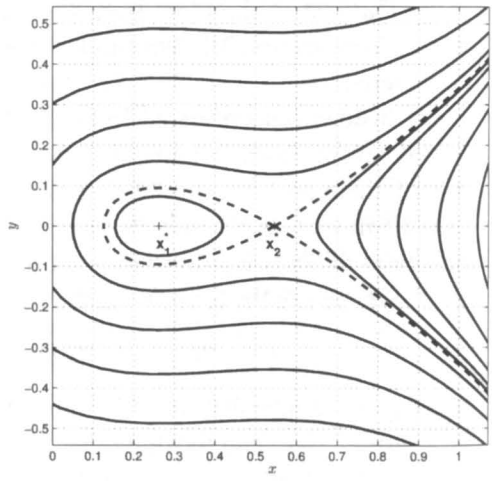

(d) $\sigma = 1/5$ and $b = 1/2$

Fig. 1 – Phase portrait for different values of σ and b. We have represented with $+$ the equilibrium points situated outside the horizon, with dashed line the separatrix and, in (a) and (d), inside it, with solid line an elliptic orbit and in (d) with dotted line the parabolic orbit and with dashdot line a hyperbolic orbit.

equation obtained substituting in (36) $y = 0$, we should find $x = 0$ and $x = x_2^\star$. But $0 < b \leq 1$ and $\sigma > 0$, therefore $x_2^\star$ should be a solution of the third factor in (36), the

following quadratic equation in x

$$x^2 - (2\sigma b + 1)x + 2\sigma = 0. \tag{37}$$

Let us remember that x_2^* is a root of the cubic equation (17). Two polynomials with arbitrary coefficients have a common root if and only if their resultant is zero (see for example Kurosh (1980)). The resultant the quadratic and cubic polynomials on hand, R, is

$$R = \frac{1}{2}\sigma(-1+b)\left(4\sigma^2 b^2 + 4\sigma b + 1 - 8\sigma\right), \tag{38}$$

and, having in mind that $\sigma > 0$ and $b \in (0,1]$ we obtain that it is equal with zero if $b = 1$ or if

$$4\sigma^2 b^2 + 4\sigma b + 1 - 8\sigma = 0. \tag{39}$$

On one hand, we note that the expression from the left side of the relation (39) is the discriminant of the quadratic equation (37). If it is zero, (37) admits a double root, $x = (2\sigma b + 1)/2$.

On the other hand, having in mind the meaning of the parameters b and σ, introduced by the relation (11), for a black hole, specified through b, and a free particle, defined through σ, if (39) holds, the particle moves on a parabolic separatrix. Let us mention that if $b = 0$, from (39), we get $\sigma = 1/8$ on the parabolic separatrix, result obtained by Dean (1999).

4. CONCLUSIONS

Using the dynamical systems approach we studied the equations of motions around a spherically symmetric static dilaton black hole. Compared to the classical methods, like expression of the solution in terms of elliptic $\wp$-Weierstrass function or numerical integration, the main features of the motion are revealed more easily, using knowledge of dynamical systems and algebra. In the exact phase-plane there are distinct regions of motion, separated by the separatrix. Analyzing it we have obtained a relation between the parameters describing the black hole and the particle, which holds on the parabolic separatrix, the border between the bounded and unbounded motion.

REFERENCES

Blaga C.: 2013, *Automat. Comp. Appl. Math.*, **22**, 41.
Blaga C.: 2015, *Serb. Astron. J.*, **190**, 41.
Casadio R. and Harms B.:1999, *Mod. Phys. Lett.*, **A14**, 1089
Chandrasekhar S.: 1983, *The Mathematical Theory of Black Holes*, Oxford University Press.
Dean B.H.: 1999, *Am. J. Phys.*, **67**, 78.
Frolov V.P. and Novikov I.D.:1998, *Black Holes: Basic Concepts and New Developments*, Kluwer Academic Publishers

Garfinkle T., Horowitz G.A. and Strominger A.: 1991, *Phys. Rev. D*, **43**, 3140.
Gibbons G.W. and Maeda K.: 1988, *Nucl. Phys.*, **B298**, 741.
Green M.B., Schwarz J.H. and Witten E.: *Superstring Theory*, vols. I-II, Cambridge University Press
Jordan D.W. and Smith P.: 1999, *Nonlinear Ordinary Differential Equations*, Oxford University Press, Oxford.
Horowitz G.A.:1993 in *Directions in General Relativity*, vol. II, eds. B.L. Hu and T.A. Jacobson, Cambridge University Press, 157.
Kurosh A.: 1980, *Higher Algebra*, Mir Publishers, Moskow.
Olivares M. and Villanueva J.R.: 2013, *Eur. Phys. J. C*, **73**, 2659.
Strogatz S.: 1994, *Nonlinear Dynamics and Chaos*, Perseus Books Publishing, Cambridge MA.

Received on 15 September 2018

PSEUDO MÜCKET TREDER POTENTIAL

D. R. CONSTANTIN[1], D. PRICOPI[2], A. A. MOCANU[3], E. VEREBELYI-VARGA[4]

[1]*Astronomical Institute of Romanian Academy*
Str. Cutitul de Argint 5, 040557 Bucharest, Romania
Email: diana@aira.astro.ro

Abstract. Within the two-body problem associating of the famous Mücket-Treder type field, we study a potential obtained by the replacement of logarithm-term with square-root term, and we call it the pseudo-Mücket-Treder (pMT-potential). Working in the analytic frame, we investigate some mathematical aspects such as: (i) we find a proper McGehee transformation in order to remove the singularity from motion equations and the first integrals corresponding of the pMT-potential; (ii) inter-playing h-the energy and C-the angular momentum values, we identify the equilibria admitted cases.

Key words: celestial mechanics – dynamical system – Mücket-Treder potential – equilibria..

1. INTRODUCTION

Mücket-Treder gravitational field has been introduced as a revision of the classical (Newtonian) field in order to explain the observed secular advance of Mercury's perihelion (Mücket, 1977). Into the Mücket-Treder type problem, Constantin at all initiated a studied motion within the framework of B-C 's model for the Sun and neighborhood of Solar System's origin (Constantin, 2018).

In the present paper, in the frame of two-body problem, we propose a similar Müucket-Treder type potential (Pricopi, 2016) which has the following form:

$$V(r) = \frac{1}{\gamma} \cdot (\frac{\beta}{r} + \frac{1}{\sqrt{r}}), \tag{1}$$

where $\beta = 2$, $\gamma = \frac{1}{\mu}$, $\mu = GM$ (G being the Newtonian constant of gravitation), M is the mass of field generated body, and $r = |\mathbf{r}|$ is the distance between two point-like masses.

In the Sections 2 and 3, we approach to the problem associated to the pMT-potential like some mathematical aspects corresponded to this potential such as the equilibrium admitted cases for a transformation of McGehee type proposed to solve the singularity which yields into motion equitations associated to pseudo Mücket-Treder type problem.

2. BASIC EQUATIONS

The Hamilton-Jacobi system associated to the two-body problem is described by the equations:

$$\dot{\mathbf{q}} = \frac{\partial H(\mathbf{q},\mathbf{p})}{\partial \mathbf{p}}, \dot{\mathbf{p}} = -\frac{\partial H(\mathbf{q},\mathbf{p})}{\partial \mathbf{q}}. \tag{2}$$

and the Hamiltonian is:

$$H(\mathbf{q},\mathbf{p}) = \frac{|\mathbf{p}|^2}{2} - \frac{(\beta + \sqrt{|\mathbf{q}|})}{\gamma \cdot |\mathbf{q}|} \tag{3}$$

We mention that $\mathbf{q} = (q_1, q_2) \in \mathbf{R}^2 \setminus \{(0,0)\}$ and $\mathbf{p} = (p_1, p_2) \in \mathbf{R}^2$ are the position vector and the momentum vector of a particle with respect to the field center, respectively.

These motion equations (2.1) admit two first integrals such as energy and angular momentum:

$$H(\mathbf{q},\mathbf{p}) = h = constant \tag{4}$$

$$L(\mathbf{q},\mathbf{p}) = q_1 p_2 - q_2 p_1 = C = constant \tag{5}$$

The Hamilton-Jacobi system associated to pMT-potential has the following form:

$$\dot{\mathbf{q}} = \mathbf{p}, \dot{\mathbf{p}} = V_{,|\mathbf{q}|} \cdot \frac{\mathbf{q}}{|\mathbf{q}|}, \tag{6}$$

where

$$V_{,|\mathbf{q}|} = \frac{-1}{\gamma \cdot |\mathbf{q}|} \cdot \left(\frac{\beta}{|\mathbf{q}|} + \frac{3}{2} \cdot \frac{1}{\sqrt{|\mathbf{q}|}}\right). \tag{7}$$

3. MCGEHEE TYPE TRANSFORMATIONS

By the introduction of polar coordinates (r,θ), we obtain after some computation the following relations:

$$r = |\mathbf{q}|, \theta = \arctan\left(\frac{q_2}{q_1}\right), \xi = \dot{r} = \frac{q_1 p_1 + q_2 p_2}{|\mathbf{q}|}, \eta = r\dot{\theta} = \frac{q_1 p_2 - q_2 p_1}{|\mathbf{q}|}, \tag{8}$$

and

$$\dot{\xi} = \frac{\eta^2}{|\mathbf{q}|} + V_{,|\mathbf{q}|}, \dot{\eta} = -\frac{\eta \cdot \xi}{|\mathbf{q}|} \tag{9}$$

We observe that the potential, equations of motion, and the integral of energy have an isolated singularity at the origin $\mathbf{q} = (0,0)$ (see also Mioc (2001)). To remove this singularity, we use the following McGehee type transformations:

$$x = r \cdot \xi, y = r \cdot \eta, \mathrm{d}\tau = r^{-2} \cdot \mathrm{d}t. \tag{10}$$

Writing $(*)' = \mathrm{d}(*)/\mathrm{d}\tau$, the equations of motion (3.1) and (3.2) become:

$$r' = r \cdot x, \theta' = y, x' = x^2 + y^2 + r^3 \cdot V_{,r}, y' = 0. \tag{11}$$

(We recall that $V_{,r} = V_{,|\mathbf{q}|}$.)

Furthermore, we obtain the new expressions of the first integrals, namely for energy and angular momentum:

$$x^2 + y^2 = 2 \cdot r^2 \cdot (h + V(r)), \tag{12}$$

$$y = C \tag{13}$$

($V(r)$ being defined in the expression (1.1)).

4. THE EQUILIBRIUM CONDITIONS

Starting with the first integrals:

$$x^2 = 2r^2(h + V) - C^2 \geq 0, \tag{14}$$

we obtain the inequality:

$$h \geq \frac{C^2}{2r^2} - V. \tag{15}$$

So, we can define the effective potential:

$$V_{eff} = \frac{C^2}{2r^2} - V \leq h. \tag{16}$$

Taking in account the equilibrium conditions:

$$x = 0, x' = 0, \tag{17}$$

the 3rd equations of array field (3.4) becomes as following:

$$\tilde{y}^2 + \tilde{r}^3 V_{,\tilde{r}} = 0 \tag{18}$$

and the first integrals become:

$$2\tilde{r}^2(h + V) - \tilde{y}^2 = 0, \tilde{y} = C \tag{19}$$

In the case of $r > 0$, we obtain the compatibility relations:

$$C^2 + \tilde{r}^3 \cdot V_{,\tilde{r}} = 0, 2\tilde{r}^2(h + V) - C^2 = 0 \tag{20}$$

Adding the compatibility relations at equilibrium, we obtain following important equations:

$$\tilde{x}^2 = f(\tilde{r}) = 2\tilde{r}^2(h+V) - C^2 = 2\tilde{r}^2(h+V) + \tilde{r}^3 V_{\tilde{r}}, \tag{21}$$

$$g(\tilde{r}) = 2\tilde{r}^2 h - \tilde{r}\frac{\sqrt{\tilde{r}}}{\gamma} + C^2 = 0. \tag{22}$$

In the last formula we observe for $M \longrightarrow \infty$ it is necessary $h < 0$.

5. DISCUSSION

Applying McGehee transformations in the pseudo-Mücket-Treder problem, we have removed the isolated singularity at the origin $\mathbf{q} = (0,0)$ from the equations of motion and the integral of energy. Further, at equilibria we obtain the compatibility relations in which it is seen as the pMT-potential admits equilibria when $h = 0, h < 0$ and when $h > 0$ only if $\tilde{r} < \left(\frac{1}{2h\gamma}\right)^2$. In the future papers, we will continue to study the dynamical aspects associated to the potential introduced in the present paper.

Acknowledgements. This work was supported by a grant of the Romanian National Authority for Scientific Research and Innovation, CNCS/CCCDI - UEFISCDI, project number PN-III-P2-2.1-PED-2016-1189, within PNCDI III and also, by a grant of the Ministry of National Education and Scientific Research, RDI Programe for Space Technology and Avanced Research - STAR, project number 513.

REFERENCES

Constantin, D. R., Pricopi, D., Mocanu, A. A., Verebelyi-Varga, E., Niculescu, V. I.: 2018, *BSG Proceedings* **25**, 30.
Mioc, V., Blaga, C.: 2001, *Rom. Astron. J.* **11**, 45.
Mücket, J.P., Treder, H. -J.: 1977, *Astron. Nachr.* **298**, 65.
Pricopi, D., Suran, M. D.: 2016, *Rom. Astron. J.* **26**, 21.

Received on 23 September 2018

STATISTICAL ANALYSIS OF ASTRO-GEODETIC DATA THROUGH PRINCIPAL COMPONENT ANALYSIS, LINEAR MODELLING AND BOOTSTRAP BASED INFERENCE

ANDREEA IOANA GORNEA[1,2], ALEXANDRU CALIN[1], PAUL DANIEL DUMITRU[1], DAN ALIN NEDELCU[2], RADU STEFAN STOICA[3]

[1]*Technical University of Civil Engineering Bucharest*
Lacul Tei Bvd. 122 - 124, 020396 Bucharest, Romania, gornea.andreea@gmail.com
[2]*Astronomical Institute of Romanian Academy*
Str. Cutitul de Argint 5, 040557 Bucharest, Romania
[3]*Université de Lorraine, Institut Elie Cartan de Lorraine*
54506 Vandoeuvre-lés-Nancy Cedex, France

Abstract. The paper demonstrates the application of statistical based methodology for the analysis of the vertical deviation angle. The studied data set contains astro-geodetic observations. The Principal Component Analysis and the Multiple Linear Regression models are embedded within a bootstrap procedure, in order to overcome the difficulties related to data correlation, while taking advantage of all the information provided. The methodology is applied on real data. The obtained results indicate that the pressure, the temperature and the humidity are variables that may influence the measure of the vertical deviation.

Key words: vertical deviation – astro-geodetic data – principal component analysis – multi-linear regression – bootstrap – statistics.

1. INTRODUCTION

The vertical deviation angle is a notion of great interest in the field of Geodesy, since it is used to establish a link between two surfaces that approximate the shape of the Earth: the geoid and the ellipsoid. The vertical deviation is defined by the angle between the direction of the plumb line and the normal to the ellipsoid through the same point on the surface of Earth (Featherstone, 1999).

The vertical deviation angle can be obtained with a geodetic total station that has attached a CCD camera and GNSS (*Global Navigation Satellite System*) receiver. This type of ensemble measures the azimuth, the zenith distance of a star that crosses its reticular wires and the time of these intersections. The horizontal coordinates are transformed into astronomic coordinates (Φ, Λ) of the observation location. The geodetic coordinates (φ, λ) of the observation location are obtained with a GNSS instrument (which has as reference surface an ellipsoid). The vertical deviation orthogonal components are obtained with the equation (1), where ξ is the meridian component - on North South direction and η is the prime vertical component - on

Table 1

Data set

Star	P (HPa)	T (°C)	H (%)	rms1 (px)	img	rms2 (px)	A (°...)	z (°...)	V (°/h)
1	2	3	4	5	6	7	8	9	10
αCas	1002.1	8.6	50.0	0.15	161	0.2	322.28286	60.91284	8.27
αOri	1002.3	8.0	50.0	0.21	312	0.16	231.03903	48.43744	14.87
γCep	1002.3	7.4	50.0	0.21	263	0.23	350.05359	55.17984	3.21
αHya	1002.4	7.1	50.0	0.24	523	0.19	176.01978	53.27512	14.82

1 - Observed star, 2 - Pressure, 3 - Temperature, 4 - Humidity, 5 -root mean square 1 in pixels, 6 - number of images taken by the CCD camera, 7 - root mean square 2 in pixels, 8 - Azimuth, 9 - Zenith distance, 10 - Star apparent velocity

East West direction.

$$\xi = \Phi - \varphi \quad ; \quad \eta = (\Lambda - \lambda)cos\varphi \tag{1}$$

The data set analysed in the paper is a large table containing the vertical deviations and its associate measures. These data were recorded on the concrete pilaster from the roof of the *Faculty of Geodesy of the Technical University of Civil Engineering Bucharest* (FG-TUCEB) on twelve nights. The data structure is given in Table 1. To each deviation angle nine quantitative variables are attached. Columns 2, 3 and 4 contain the atmospheric parameters, columns 5 and 7 contain errors given by the CCD image acquisition software. These values represent the errors resulted after the trajectory of the star in the field of view was reconstructed based on all the CCD images. Columns 8, 9 and 10 are variables that characterise the observed star. The data contained in Table 1 is not normalised.

Figure 1 shows the behaviour of the measured values ξ and η given the deviation angle. The present paper has two aims. The first one is to exhibit possible linear relations between the deviation angle values and their associate measures, respectively. The second one attempts to establish which of these measures plays an important role in the variability of the deviation angle. The answer to these questions are formulated proposing a bootstrap based statistical analysis based on *Principal Component Analysis* (PCA) and *Multi-Linear Regression* (MLR). The vertical deviation components behaviour resembles the one of a statistical series. Within this assumption, the present paper aims to study the variability of the data set that contains the vertical deviation components.

The structure of the paper is as follows. The next two sections present the PCA and MLR methods and results applied to our data set, together with their associate bootstrap procedure respectively. Finally, conclusions and perspectives are depicted.

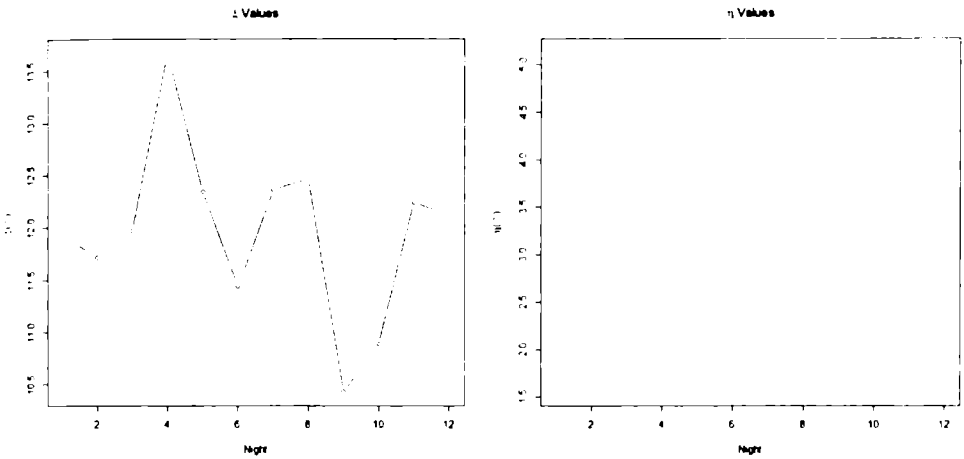

Fig. 1 – ξ and η values variation. Values from all observation nights (12) - FG - TUCEB show a significant variation relative to the value size

2. PRINCIPAL COMPONENT ANALYSIS

Principal Component Analysis (PCA) is a statistical method allowing numerical and visual description of relevant features in multidimensional data (Husson *et al.*, 2011). The data set from the present study has 510 rows (individuals = measurements) and 9 columns (quantitative variables). Additionally, the data set contains two supplementary quantitative variables - the two components of the vertical deviation angle and two qualitative variables - the observation night and the observed star.

PCA was applied on the standardised data set because the variables did not have the same measurement unit. Standardisation means considering $\frac{x_{ik}-\bar{x_k}}{s_k}$ instead of x_{ik} and choosing standard deviation $s_k = \sqrt{\frac{1}{I-1}\sum_{i=1}^{I}(x_{ik}-\bar{x_k})^2}$ as a unit of measurement for each variable k. Connecting these new values with the normal distribution can highlight possible outliers or extreme values. Table 2 contains a few standardised values for all nine quantitative variables. The measures higher than 2 in absolute value are coloured in blue. Assuming a Gaussian character for the observed data, the following variables may be considered rather extreme: humidity, number of images, root mean square 2 and velocity.

PCA considers the data set to be analysed as a point cloud in a multidimensional space. Through PCA the best viewpoint is searched by finding the dimensions (axes) on which the variability of the point cloud is higher. Whenever the individuals are studied, the data set is seen as a point cloud in a space with 9 dimensions (the

Table 2

Suggested extreme values in standardised data set

Ind	Star	P	Temp	Hum	rms1	No img	rms2	A	z	V
1	2	3	4	5	6	7	8	9	10	11
56	αHya	0.30	-1.85	–0.13	–0.44	3.73	–0.89	0.04	–0.44	0.81
57	βUMi	–1.94	–1.62	–0.13	1.95	1.85	4.14	–1.47	–0.79	–1.93
58	βUMi	–1.83	–1.64	–0.13	–0.44	3.37	0.52	–1.47	–0.82	–1.93
59	βUMi	–1.85	–1.64	–0.13	0.04	2.12	0.52	–1.47	–0.84	–1.93
60	βUMi	–1.85	–1.65	–0.13	1.00	1.86	2.57	–1.47	–0.85	–1.93
61	βUMi	–1.83	–1.68	–0.13	0.52	4.88	1.15	–1.47	–0.88	–1.93
62	βUMi	–1.81	–1.69	–0.13	–0.44	2.89	0.52	–1.47	–0.90	–1.93
63	βUMi	–1.81	–1.71	–0.13	–0.28	2.12	0.68	–1.47	–0.92	–1.93
64	βUMi	–1.81	–1.71	–0.13	0.20	2.42	2.57	–1.47	–0.93	–1.93
506	ηUMa	1.96	–0.52	3.73	1.00	0.00	0.37	1.35	0.63	–0.48
507	ηUMa	1.96	–0.52	3.73	0.84	0.01	0.21	1.35	0.66	–0.48
508	αUMi	1.96	–0.55	3.94	0.20	–0.46	–0.11	1.83	–1.59	–2.93
509	αUMi	1.96	–0.58	4.14	1.00	0.20	0.21	–1.66	–1.60	–2.93
510	αUMi	1.96	–0.58	4.14	1.00	0.20	0.21	–1.66	–1.60	–2.93

number of active quantitative variables). Whenever the variables are studied the data set is considered as a point cloud in a space with 510 dimensions (the number of individuals).

The Figure 2 shows the projection of the data set point cloud on the axes given by the PCA analysis. It can be observed that the majority of points tend to be concentrated in a rather compact region around the origin, while the rest of them tend to spread further away from it within a certain degree of variability. The variability of a dimension is measured as the ratio of the inertia of the cloud projected on the considered dimension over the total inertia of the cloud. Correlating Table 2 and Figure 2 reveal which individuals can be considered as extreme or outliers.

The variability percentages caught by each dimension, respectively, are presented in Table 3. The axes are usually, ordered and presented in decreasing order with respect to the variability. This PCA feature allows the reduction of the number of dimensions, since we may consider only those dimensions that have an important contribution to the total cloud inertia.

Table 3

Percentage of inertia for each dimension and cumulative percentage of inertia

Dimension	Percentage of inertia	Cumulative percentage of inertia
1	23.04%	23.04%
2	18.62%	41.66%
3	16.56%	58.23%
4	12.74%	70.98%
5	9.53%	80.51%
6	7.25%	87.77%
7	5.36%	93.14%
8	3.74%	96.89%
9	3.11%	100%

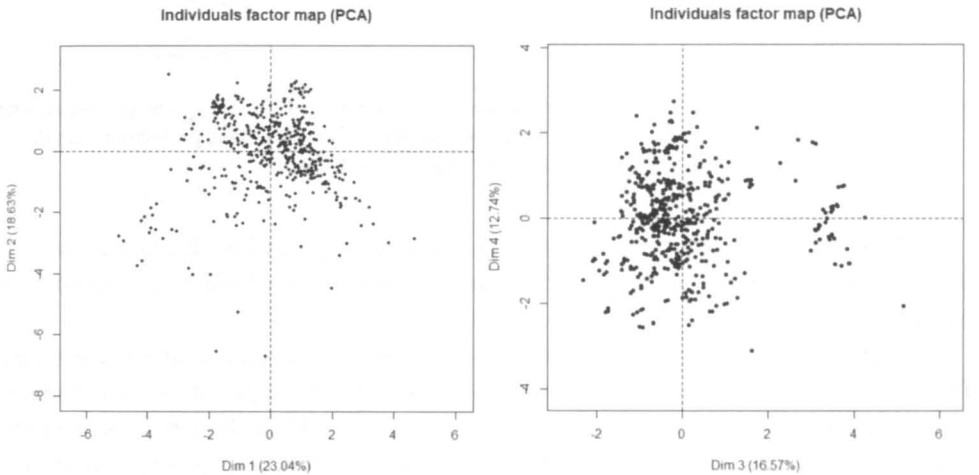

Fig. 2 – Visualisation of the first four axes given by the PCA, $(D_i), i = 1, \ldots, 4$. Left plot : the data point cloud projected on the (D_1, D_2) plane. Right plot : the data point cloud projected on the (D_3, D_4) plane.

The PCA enables to see whether different measures tend to exhibit a certain pattern within the data set point cloud. The left plot in Figure 3 shows the point cloud projected on the (D_2, D_3) plane, while the points are labelled depending on the night the measure was obtained. The right plot in Figure 3 shows the point cloud projected on the (D_1, D_2) plane, while the points are labelled depending on the observed star. A clustered pattern depending on the observation is observed in the left plot. The pattern in the right plot appears to be less clustered, much more mixed, and it does not allow to affirm just by visual inspection how the choice of the observed star influences the distribution of points in the cloud.

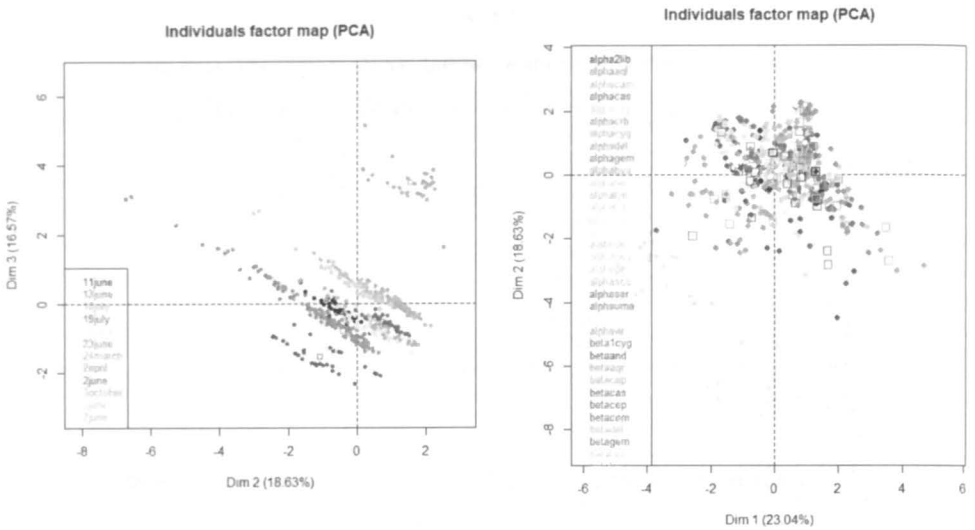

Fig. 3 – Color coded projection of the data set point cloud. Left plot : (D_2, D_3) plane projection with the colours representing the observation nights. Right plot : (D_1, D_2) plane projection with the colours representing the observed star.

It is legitimate to ask whether these patterns appeared by chance or not. In order to answer this question, a statistical test based on a bootstrap procedure is implemented.

The test works as follows. First, for each cluster the median centre is computed. This choice is adopted against the most common one of the gravity centre, in order to use a measure much more robust to extreme values. Then the labels of the point cloud were changed uniformly, while keeping the point positions fixed. A number of 50 such samples was obtained. For each such simulated data set the median centres were computed. This allows testing whether the observed median centres may be considered as the outcome of "completely random" distribution of labels.

Tables 4 contains the quantile interval, defined by the second highest median coordinate (column 4) and second lowest median coordinate (Column 3) of the rearranged groups of individuals defined by the observation night. Column 5 contains the initial medians and the ones that are highlighted are inside the quantile interval. If the initial median is outside the quantile interval, the test rejects the null hypothesis, that the clustered structure from Figure 3 occurred by chance. As it can be observed in most of the cases, the medians are outside the intervals. Hence, in these situations, there is statistical evidence that the clusters induced by the observation do not occur simply by chance.

Table 5 contains the confidence/quantile intervals for the median coordinates of the groups of individuals defined by the observed star. . For this case most of the me-

Table 4

Confidence intervals for each individual group defined by the observation night - dimensions 2 and 3

Group/Date	Dimension	Q_{50}^{2}	Q_{50}^{49}	Initial median
1	2	3	4	5
24-Mar	2	–0.2121	0.4235	1.2785
	3	–0.4537	–0.0761	–0.1209
02-Apr	2	–0.2441	0.5379	–1.6020
	3	–0.5381	–0.0122	0.2494
02-Jun	2	–0.2006	0.5055	0.8056
	3	–0.5244	0.0567	–0.5717
05-Jun	2	–0.1800	0.6150	0.1404
	3	–0.4142	–0.0383	0.3114
07-Jun	2	–0.3461	0.4347	0.7221
	3	–0.4935	0.1442	0.2037
11-Jun	2	–0.2945	0.4752	–0.5074
	3	-0.4429	0.0039	–0.2412
13-Jun	2	–0.2730	0.5352	–0.6396
	3	–0.4399	–0.0477	–0.5899
22-Jun	2	–0.4111	0.5344	0.3883
	3	–0.4530	0.0138	–0.6743
23-Jun	2	–0.3357	0.5199	–0.1127
	3	–0.3987	–0.0296	–0.9632
18-Jul	2	–0.4434	0.5082	0.5518
	3	–0.5748	0.0622	–0.6809
19-Jul	2	–0.1517	0.7270	–1.1975
	3	–0.5790	0.0540	–1.5421
03-Oct	2	–0.4188	0.5411	1.7935
	3	–0.5648	0.0394	3.4696

Table 5

Confidence intervals for individual groups defined by the observed star - dimensions 1 and 2

	$\alpha 2Lib$				ζVir		
	Q_{50}^{2}	Q_{50}^{49}	Median		Q_{50}^{2}	Q_{50}^{49}	Median
1	2	3	4		233	234	235
Dim.1	–1.37365	1.13447	1.12740		–0.88601	1.17979	1.95559
Dim.2	–0.95837	0.81787	–0.24940		–0.98032	0.99207	–0.10296
Dim.3	–0.87625	0.4393	–0.24627	...	–0.8321	0.28378	–1.03948
Dim.4	–0.96603	1.01562	0.21106		–0.7906	0.97161	–0.07010
Dim.5	–0.63005	0.38843	–0.28810		–0.9134	0.64677	–0.16855
Dim.6	–0.65236	0.85768	–0.34874		–0.57335	0.66941	0.45769
Dim.7	–0.69171	0.40592	0.71968		–0.40571	0.32182	0.64569
Dim.8	–0.37297	0.3473	0.23813		–0.41065	0.53837	0.05889
Dim.9	–0.55583	0.31309	0.19781		–0.37045	0.48317	0.06883

Table 6

Variables coorrelations with the first four dimesnions

Variable	Dim.1	Dim.2	Dim.3	Dim.4
P	0.22	0.61	0.51	–0.35
T	0.52	–0.06	–0.35	–0.65
H	0.03	0.38	0.83	0.04
rms1	0.67	–0.44	0.39	0.03
img	–0.77	–0.23	0.20	0.07
rms2	0.38	–0.71	0.32	0.22
A	0.11	0.55	–0.25	0.46
Z	0.37	0.08	–0.04	0.56
velocity	0.64	0.29	–0.22	0.16

dians are inside the quantile intervals (more than 70% of the medians). The structure defined by the observed star is not as strong as the one defined the observation night. The quantile intervals from Tables 4 and 5 correspond to a 96% probability. The stars can be identified in Table 5 with their Bayer designation (Greek letter followed by the abbreviation of the parent constellation's Latin name - *e.g.*,ζVir).

The linear correlation coefficient between the data set variables and the PCA axes, respectively, contains useful information. It reveals the contribution of one variable to the variability of the point cloud within a considered axis. The variables that are strongly correlated with the first four PCA dimensions are highlighted in Table 6. All nine variables have the absolute value of the estimated linear correlation coefficient higher than 0.5 for at least two dimensions. Among them, the pressure P and the temperature T influence the variability of at least two PCA dimensions. The other way around, the axes D_1 and D_2 are strongly correlated with at least three variables, each.

Since the correlation coefficient takes values in the interval $[-1, 1]$, the correla-

tion coefficients between the data set variables and the PCA axes can be represented on a hyper-sphere. Figure 4 shows correlation coefficients of the variables with the first four dimensions. The closer the correlation arrow is to the circle border, the stronger the linear dependence between the considered variable and axis. The η and ξ correlations were added to the plot. Hence from Figure 4 it can be concluded to what variables are the two vertical deviation components correlated with. The ξ variable is strongly correlated with the variables "H", "A", "P", "velocity", "Z", "T" and "rms1" and the η variable is correlated with the variables "img", "rms2", "T". This information may be important whenever linear modelling is considered.

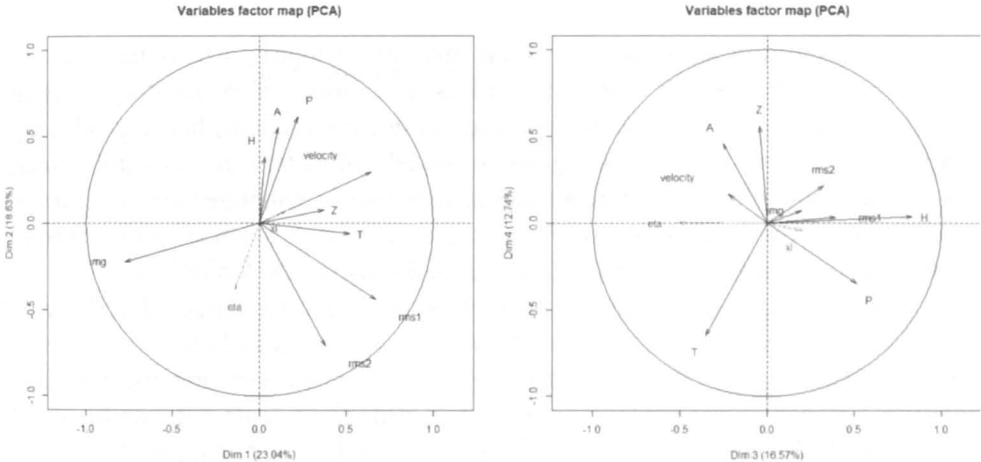

Fig. 4 – Correlation circles for the first four PCA axes (1^{st} and 2^{nd} dimensions - right, 3^{rd} and 4^{th} dimensions - left, together with the two vertical deviation components.

3. MULTIPLE LINEAR REGRESSION MODELLING

PCA results are an extremely useful exploratory tool. Nevertheless, in order to get more reliable inference the integration of this information should be done. This can be achieved through statistical modelling. In this section linear modelling is used to check which of the variables in the data set that may explain the behaviour of the vertical deviation values.

The considered linear models are given by the regression equations:

$$\xi_i = \beta_0^{\xi} + \sum_{j=1}^{p} X_{ij}\beta_j^{\xi} + \epsilon_i^{\xi} \tag{2}$$

and

$$\eta_i = \beta_0^\eta + \sum_{j=1}^{p} X_{ij}\beta_j^\eta + \epsilon_i^\eta \tag{3}$$

where (X_{ij}) are the elements of the design matrix given by Table 1, the βs are the corresponding model parameters, p is the order of the model and the ϵs are the corresponding errors, which here are assumed to be Gaussian i.i.d with their variances σ_η^2 and σ_ξ^2, respectively.

The data set presented in Table 1 contains a total of 510 measures obtained during 12 observation nights. Several measures are recorded during one night. The measures corresponding to one observation night are highly correlated with each other. In order to reduce the data correlation while taking into consideration all the available data, a bootstrap procedure is implemented, for solving the regression systems (2) and (3).

The procedure is as follows. First, the design matrix size is fixed to 12×9, where 12 is the number of nights and 9 is the number of explanatory variables. Second, for each night a measure is chosen uniformly random, hence producing a random design matrix. Next, the regression model parameters are estimated. Finally, the last two steps of the procedure are repeated 100 times, enabling the approximation of the probability distributions of the multiple linear regression outputs. This was applied on the standardised data as it was used during the PCA analysis.

Figure 5 shows the outputs of the method applied to the model (2). The model fits poorly the data. This is indicated by the $p-$values distribution of the Fisher test that does not reject the constant model. In agreement with this, the confidence intervals outlined by the model's coefficients distributions contain 0 with high probability. Still, the histogram of the R^2 coefficient indicates that more than 50% of the variation of the deviation angle may be explained by linear regression of the explanatory variables. The coefficient distributions corresponding to the pressure, the temperature and the humidity exhibit an asymmetric behaviour. This character may be interpreted as a particular weight that these variables may contribute within the variation of the deviation angle. Nevertheless, at this point, in order to be able to perform more reliable analysis more data is needed.

Following Jacques and Fraix-Burnet (2015), the previous method was applied, while the design matrix for the models (2) and (3), respectively, was given by the PCA coordinates associated to each element in the data set. The results are shown in Figure 6. The results analysis is similar to the preceding one. It appears that again, the model coefficients of the dimensions exhibiting asymmetric distributions are the ones that are the most correlated with variables such that the pressure, the temperature and the humidity.

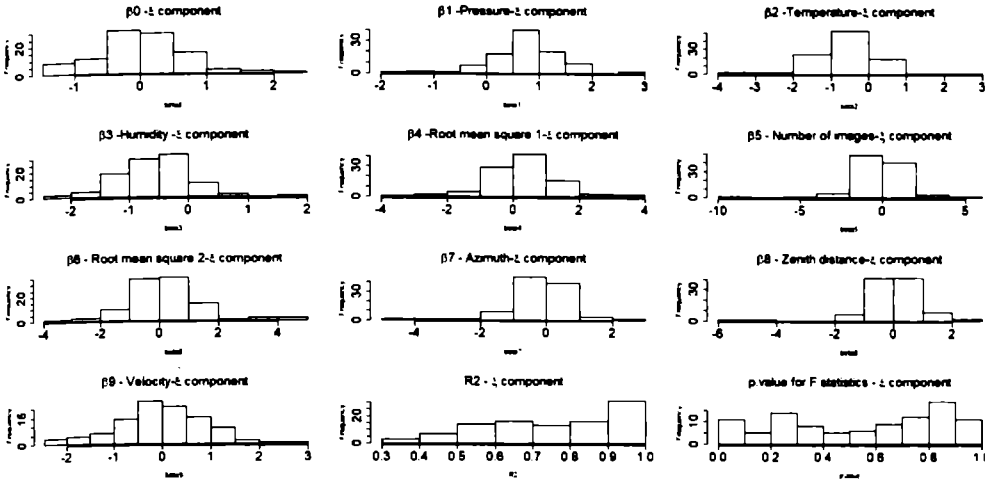

Fig. 5 – Estimation distributions of the model (2).

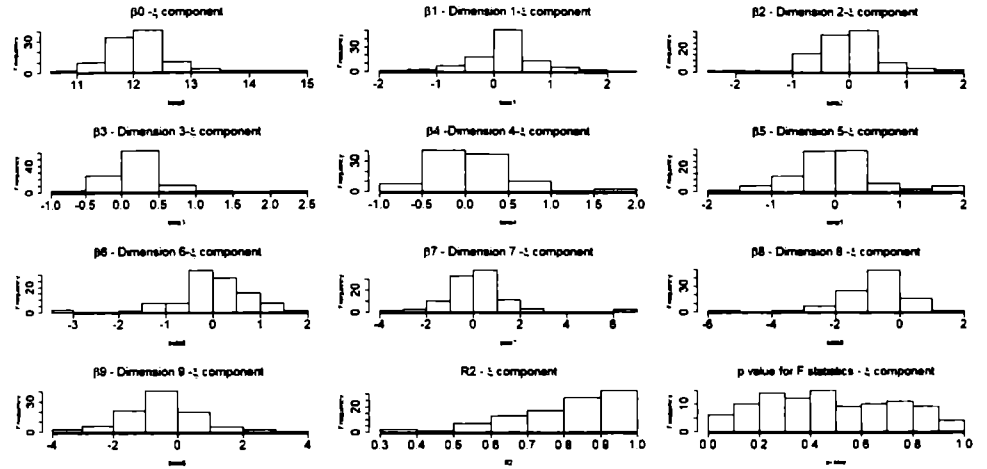

Fig. 6 – Estimation distributions of the model (2) applied to the PCA transformation of the design matrix.

4. CONCLUSIONS

This work presented the application of statistical based methodology for the analysis of the vertical deviation angle. The ingredients of the methodology were : Principal Component Analysis and the Multiple Linear Regression models. In order to overcome the difficulties related to data correlation, while taking advantage by all the information provided, theses two classical techniques were embedded within a bootstrap procedure.

The methodology was applied on real data. The obtained results indicated that the pressure, the temperature and the humidity are variables that may influence the measure of the vertical deviation.

The preliminary results presented here are the starting point of an ongoing project. The campaign of collecting data should continue in order to improve the quality of the obtained results. Since the quantity and the quality of the data will increase recent statistical methods should be considered Hastie *et al.* (2009).

Acknowledgements. The first and the last author are extremely grateful to Dr. Octavian Badescu, for helping with the data collection and for the fruitful scientific discussions.

This work was supported by a grant of the Ministry of National Education and Scientific Research, RDI Program for Space Technology and Advanced Research - STAR, project number 513

REFERENCES

Featherstone, W.E.: (1999). *Sixth South East Asian Surveyors' Congress Fremantle*, 1-6 November 1999, The use and abuse of vertical deflections Western Australia.

T. Hastie, R. Tibshirani and J. Friedman: *The elements of statistical learning data mining, inference, and prediction - second edition*, Springer.

Husson, F., Lê, S., Pagès, J.: 2011, *Exploratory Multivariate Analysis by Example Using R*, Chapman & Hall/CRCC.

Jacques, J., and Fraix-Burnet, D.: 2015, *Linear regression in high dimension and/or for correlated inputs. Methods and applications of the regression* (eds. D. Fraix-Burnet and D. Valls-Gabaud), European Astronomical Society Publication Series EDP Sciences.

Received on 27 September 2018

FINITE SIZE SCALING TECHNIQUE AND APPLICATIONS – ULYSSES DATA

EMIL POPESCU[1,2], NEDELIA A. POPESCU[2]

[1]*Technical University of Civil Engineering, Bd. Lacul Tei 124, 020396 Bucharest, Romania*
Email: emil.popescu@aira.astro.ro
[2]*Astronomical Institute of Romanian Academy, Str. Cutitul de Argint 5, 040557 Bucharest, Romania*

Abstract. The study of statistical properties of the interplanetary magnetic field fluctuations represents an important issue in space research. These fluctuations are in connection with acceleration processes and energy transport in the solar wind, providing an important understanding on the solar wind turbulent cascade. In this paper the finite size scaling technique is applied on the Ulysses/VHM data for the years 2002-2003, in order to study the scaling of the interplanetary magnetic field magnitude (B) and magnetic energy density (B^2) fluctuations, at different scales (time lags $\tau_n = 2^n$ days, $n = 0, 1, 2, ...$).

Key words: Solar wind turbulence – solar wind plasma parameters and interplanetary magnetic field fluctuations – probability distribution function – intermittent behavior.

1. MATHEMATICAL MODEL

The fractional diffusion equations provide a suitable mathematical framework for the multiscale behavior, reflecting the connection and similarities between processes occurring on different spatial and temporal scales.

The statistics of several quantities in space plasmas are in agreement with some models based on space-time fractional derivative equations. Fractional derivative equations are abstract partial differential equations that contain fractional derivatives in space and time. They are useful to model a wide variety of phenomena in physics, chemistry, biology, etc. connected with anomalous diffusions. The fractional calculus is a good approach modeling of typical anomalous features that are observed in solar wind turbulence.

A space-time fractional diffusion equation is obtained from the standard diffusion equation by replacing the second order space-derivative by a fractional Riesz derivative of order $\alpha > 0$ and skewness θ, and the first order time-derivative by a fractional derivative of order $\beta > 0$ in Caputo or Riemann-Liouville sense:

$$\frac{\partial^\beta F}{\partial t^\beta}(x,t) = \frac{\partial^\alpha F}{\partial x^\alpha}(x,t),\ 0 < \alpha \leq 2,\ 0 < \beta \leq 2,\ -\infty < x < \infty,\ t \geq 0, \quad (1)$$

with $u(x,0) = \Delta(x)$.

In the cases $0 < \alpha < 2$. $\beta = 1$ or $\alpha = 2$, $0 < \beta < 2$ or $0 < \alpha = \beta \leq 2$, the fundamental solution (or Green function) $F_{\alpha,\beta}(x,t)$ of the equation can be interpreted as a spatial probability density function (PDF) evolving in time. It is well known that for the standard diffusion ($\alpha = 2$, $\beta = 1$) the Green function is the Gaussian PDF. The scaling property of the Green function allows to express it in terms of a function of a single variable, the reduced Green function $R_{\alpha,\beta}(x)$ (see Mainardi *et al.* (2001)). We observe that $R_{\alpha,1}(x)$ are the stable distributions. Some computational forms of $R_{\alpha,\beta}(x)$ are as follows:

i) if $\alpha = \beta$ then

$$R_{\alpha,\alpha}(x) = \frac{1}{\pi x}\sum_{n=0}^{\infty}(-x^{\alpha})^{n}\sin\left[\frac{n\pi}{2}(\theta-\alpha)\right], \quad 0 < x < 1 \tag{2}$$

and

$$R_{\alpha,\alpha}(x) = \frac{1}{\pi x}\sum_{n=0}^{\infty}(-x^{-\alpha})^{n}\sin\left[\frac{n\pi}{2}(\theta-\alpha)\right], \quad x > 1. \tag{3}$$

ii) for $\alpha < \beta$ we have

$$R_{\alpha,\beta}(x) = \frac{1}{\pi x}\sum_{n=1}^{\infty}(-x^{-\alpha})^{n}\frac{\Gamma(1+n\alpha)}{\Gamma(1+n\beta)}\sin\left[\frac{n\pi}{2}(\theta-\alpha)\right], \quad x > 0. \tag{4}$$

Thus we are able to plot the probability density functions (PDFs) for different values of α and β.

In classical diffusion, particles spread in a normal bell-shaped pattern according to Gaussian probability distribution. Anomalous diffusion occurs when the growth rate or the shape of the particle distribution is different than Gaussian. Fractional derivatives in space are associated with very large particle jumps. Very long waiting times lead to fractional derivatives in time. Empirical evidence reveals that the waiting time between jumps is correlated with the next size of the particle jumps. For these models, a coupled space-time fractional derivative equation rules the limiting particle distribution.

A purpose of this study is to show that the PDF's are well adapted to model the random characteristic of the interplanetary magnetic field in different cases of configurations.

2. STATISTICAL SCALING PROPERTIES OF THE MAGNETIC FIELD INTENSITY AND MAGNETIC ENERGY DENSITY FLUCTUATIONS

In this section is presented the analysis of the magnetic field intensity ($B(t)$) and magnetic energy density ($B^2(t)$) fluctuations at different scales, using the interplanetary magnetic field data recorded by the magnetometer VHM/FGM on board Ulysses mission, for the years 2002-2003. In this interval of time Ulysses mission, being at the beginning of its third solar orbit, was situated at heliocentric distances between 2.5859-5.305 AU (astronomical units).

2.1. STATISTICAL SCALING PROPERTIES OF TIME SERIES

We consider a time series $x(t)$ sampled at times $t_1 < t_2 < ... < t_N$. Let $\Delta = t_k - t_{k+1}$, $k = 1, ..., N$. We can construct a differenced time series with respect to the time increment $\tau = s\,\Delta$, $s \in \mathbf{R}$. In this case we have: $y(t,\tau) = x(t+\tau) - x(t)$.

For N succesive values, we obtain:

$$\begin{aligned} y(t_1,\Delta) &= x(t_1+\Delta) - x(t_1) \\ y(t_2,\Delta) &= x(t_2+\Delta) - x(t_2) \\ &\dots \\ y(t_{N-1},\Delta) &= x(t_{N-1}+\Delta) - x(t_{N-1}) \\ y(t_N,\Delta) &= x(t_N+\Delta) - x(t_N) \end{aligned}$$

and

$$x(t_N) = x_0 + \sum_1^N y(t_k,\Delta), \tag{5}$$

where the initial point $x_0 = x(t_N - (N-1)\Delta)$. We assume that $y(t,\tau)$ is a stochastic variable, so that $x(t+\tau) = x(t) + y(t,\tau)$ is a random walk. We define:

$$\begin{aligned} y^{(1)}(t_1,2\Delta) &= y(t_1+\Delta) + y(t_2,\Delta) \\ y^{(1)}(t_2,2\Delta) &= y(t_2+\Delta) + y(t_3,\Delta) \\ &\dots \\ y^{(1)}(t_k,2\Delta) &= y(t_k+\Delta) + y(t_{k+1},\Delta) \\ &\dots \\ y^{(1)}(t_{N/2},2\Delta) &= y(t_{N/2}+\Delta) + y(t_{N/2+1},\Delta) \end{aligned}$$

Thus $x(t_N) = y^{(1)}(t_1,2\Delta) + ... + y^{(1)}(t_k,2\Delta) + ... + y^{(1)}(t_{N/2},2\Delta)$.

By this procedure with N and n arbitrarily large, we obtain:

$$x(t_N) = y^{(n)}(t_1,2^n\Delta) + ... + y^{(n)}(t_k,2^n\Delta) + ... + y^{(n)}(t_{N/2^n},2\Delta). \tag{6}$$

We assume that y are scaling with α: $y\prime = 2^\alpha y$, $\tau\prime = 2\tau$.

This means that: $y^{(n)} = 2^{n\alpha} y$, $\tau = 2^n\Delta$.

For arbitrary y we can write: $y'(t,\tau) = \tau^\alpha y(t,\Delta)$, where we considered the normalization $\tau \equiv \tau/\Delta$. Then, for the stochastic variable y, there exists a probability distribution function (PDF), P, which is unchanged under the above transformation. We have $P(y'\tau^{-\alpha})\tau^{-\alpha} = P(y)$.

2.2. FINITE SIZE SCALING TECHNIQUE

We apply the finite size scaling technique on Ulysses data in order to study the scaling and intermittency of the magnetic field intensity and magnetic energy density

fluctuations.

Intermittency denotes the statistical comportment of the fluctuations in the spatial domain. In case of the validity of the Taylor hypotheses (*i.e.* a turbulent structure transits the spacecraft at a time which is small in comparison with its own evolution - see Taylor (1938)), time differences are equivalent to space differences. The deviation of the probability distribution function (PDF) of fluctuations from a Gaussian distribution underlines the intermittency.

In our study the considered technique is based on differencing of the original time series over a range of temporal scales τ. The fluctuations on temporale scale τ can be taken by a set of differences $dS(t,\tau) = S(t+\tau) - S(t)$, where $S(t)$ represents a given time series (see Frisch (1995)).

The basic quantities considered in this section are the changes in the magnetic field intensity (B), respectively magnetic energy density (B^2), at different scales (time lags $\tau_n = 2^n$ days, $n = 0, 1, 2, ...$) (see also previous subsection).

First step in our calculation is represented by the determination of:

a) magnetic field intensity increments at a given scale τ_n through:

$$dB_n = dB_n(t_i, \tau_n) = [B(t_i + \tau_n) - B(t_i)], \tag{7}$$

where t_i - the time (days of the year); $B(t_i)$- the daily average of B;

b) magnetic energy density increments at a given scale τ_n through:

$$dB_n^2 = dB_n^2(t_i, \tau_n) = \left[B^2(t_i + \tau_n) - B^2(t_i)\right], \tag{8}$$

where t_i - the time (days of the year); $B^2(t_i)$- the daily average of B.

The second step consists in the normalization of these quantities (which represent characteristic fluctuations across eddies at the scales τ_n) to their variance, σ^2, obtaining data sets of normalized fluctuations of the magnetic field intensity, respectively magnetic energy density.

3. MAGNETIC FIELD AND MAGNETIC ENERGY DENSITY FLUCTUATIONS ANALYSIS AND RESULTS

In Figure 1 are presented the magnetic field intensity profile (top panel) and solar wind velocity profile (bottom panel), during 2002-2003 (a total of 730 days of data recorded by Ulysses). The magnetic field strength signal observed by Ulysses during 2002-2003 is depicted in Figure 2.

We considered scales ranging from $\tau_0 = 1$ day to $\tau_5 = 2^5 = 32$ days, and obtained six normalized data sets $dB_n(t_i, \tau_n)$. At scales of 1, 2, and 4 days, the fluctuations $dB_0(t)$, $dB_1(t)$ and $dB_2(t)$ are intermittent with spikes (pulse of extremely short duration), superposed on a signal with bursts (abrupt increase in the amplitude of the signal) of fluctuations, especially for the year 2002 (days 1-365). At larger

scales the fluctuations are less intermittent (less bursty and spiky).

We have to mention that the intermittency (which is connected with sudden occurrence of large amplitude variations of magnetic field intensity) is usually pointed out as a departure of the PDFs from a Gaussian distribution. The intermittency is the triggering process for increased probabilities of large amplitude fluctuations at smaller scales.

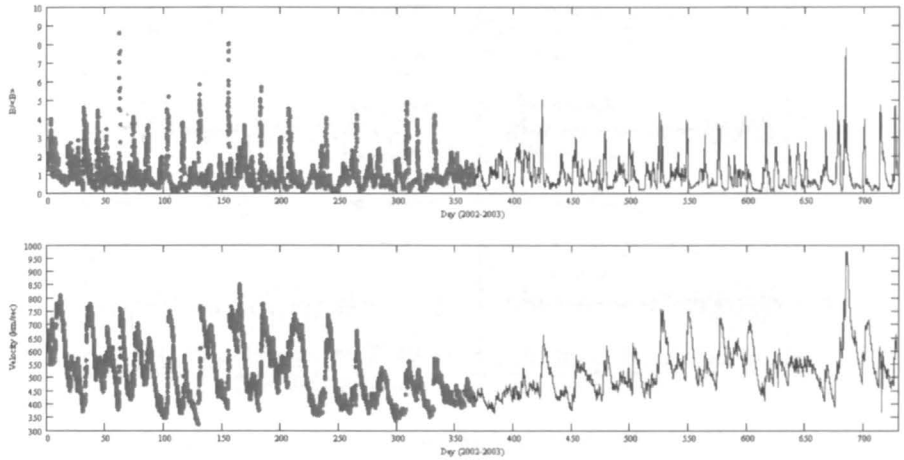

Fig. 1 – Time series of magnetic field intensity B (top panel); solar wind velocity v (bottom panel) during 2002-2003 years of data recorded by Ulysses.

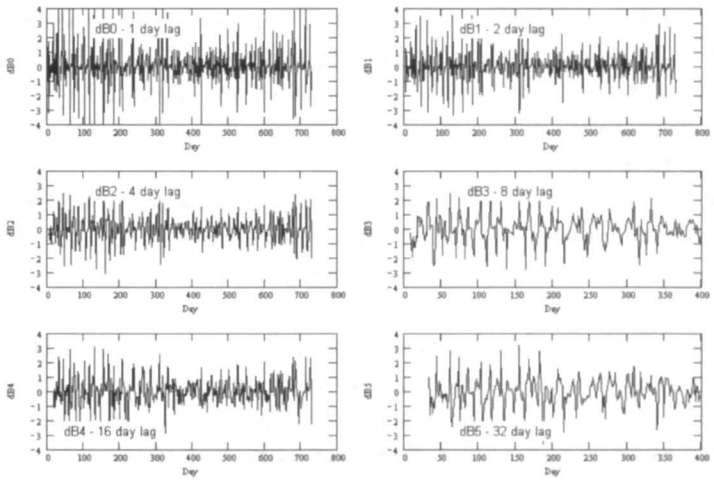

Fig. 2 – The determined dB_n for the scales $n = 0, ..., 5$.

Figure 3 presents the magnetic energy density signal, observed by Ulysses during 2002–2003, for scales ranging from $\tau_0 = 1$ day to $\tau_5 = 2^5 = 32$ days. We obtained six normalized data sets $dB_n^2(t_i, \tau_n)$.

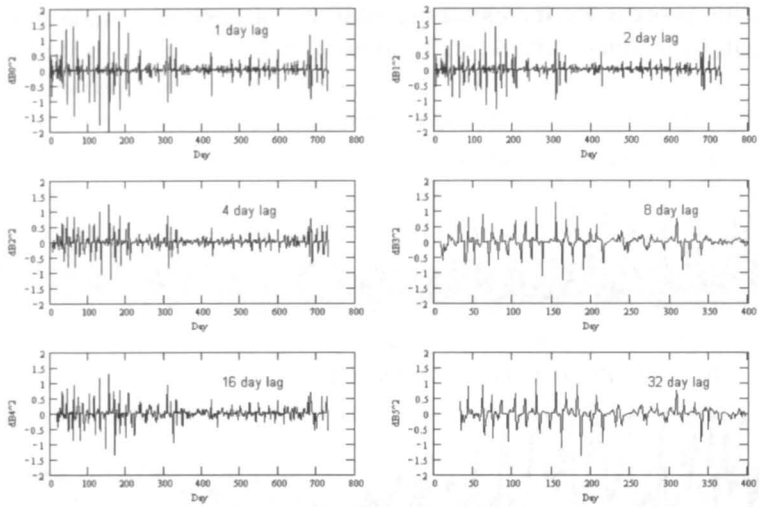

Fig. 3 – The determined dB_n^2 for the scales $n = 0, ..., 5$.

Magnetic field intensity and magnetic energy density fluctuations at different time scales are quantitatively described by the PDFs. These are represented by the normalized histograms of $dB_n(t_i, \tau_n)$, respectively $dB_n^2(t_i, \tau_n)$.

In Figure 4, respectively Figure 5, from top to bottom, are presented the PDFs of the normalized fluctuations of the magnetic field intensity, respectively magnetic energy density, measured by Ulysses, on time scales of 1, 2, 4, 8, 16, 32 and 64 days.

In order to reveal the shape of PDFs, these are separated by 0.1 differences in Figure 4, respectively 0.3 difference in Figure 5. The presence of heavy tails is obvious for all time scales.

Figure 6 presents the observational (points) and theoretical PDFs (continuous lines) for 8, 32 and 64 days time scales. The theoretical PDFs, fdB_3 and fdB_5, are obtained for $\alpha = \beta \leq 0.2$ using the formulae (2) and (3).

In order to point out the heavy tails, the logarithmic scale is considered. At large scales the PDFs are almost Gaussian, and the tails of the distributions grow up as the scale becomes smaller. The presence of intermittency is obvious for fdB_3 and fdB_5, where the PDFs of fluctuations increasingly depart from a Gaussian distribution with decreasing temporal scale. The observational (points) and theoretical PDFs (continuous lines) for 1, 4, 8 and 32 days time scales are presented in Figure 7. The theoretical PDF fdB_0 is obtained for $\alpha = 0.35$, $\beta = 0.7$, $\theta = -0.25$ with formula (4).

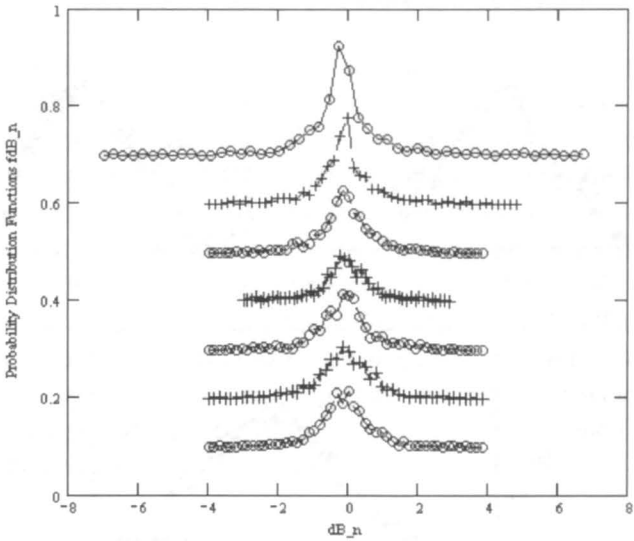

Fig. 4 – The observational PDFs - fdB_n - for the scales $n = 0, 1, 2, ..., 6$, for the magnetic field intensity fluctuations.

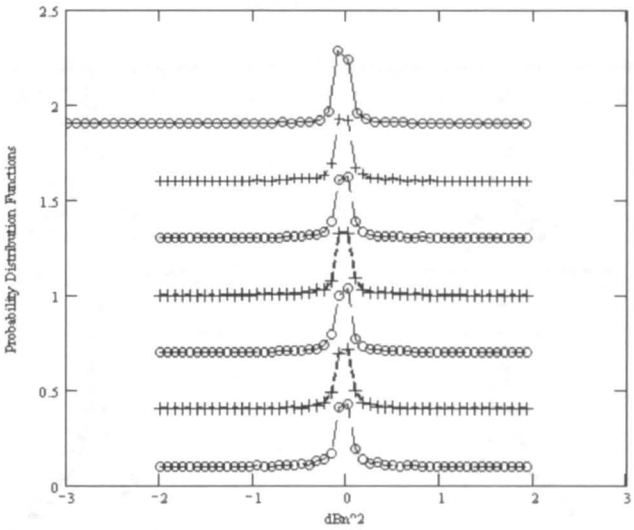

Fig. 5 – The observational PDFs for the scales $n = 0, 1, 2, ..., 6$, for the magnetic energy density fluctuations.

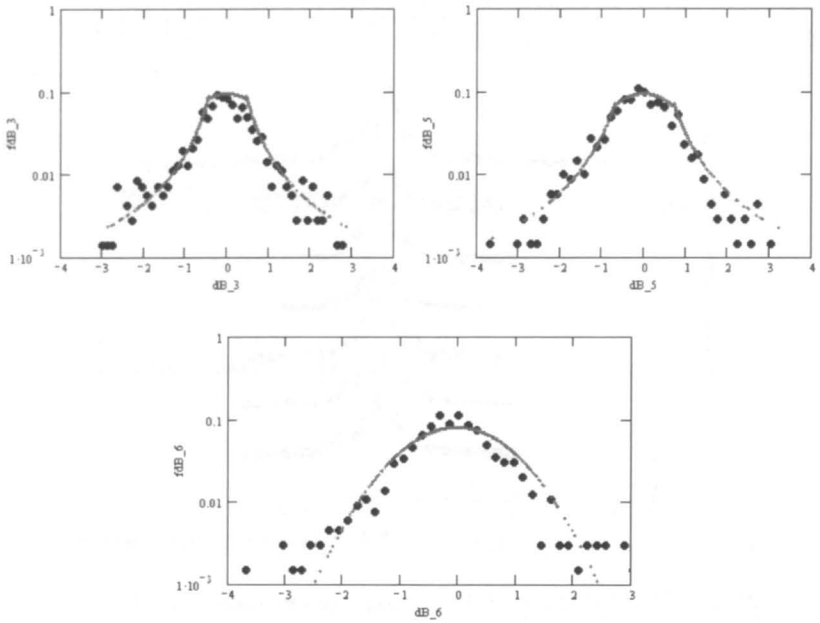

Fig. 6 – The observational (points) and theoretical PDFs - fdB_n, for the scales$n = 3, 5, 6$.

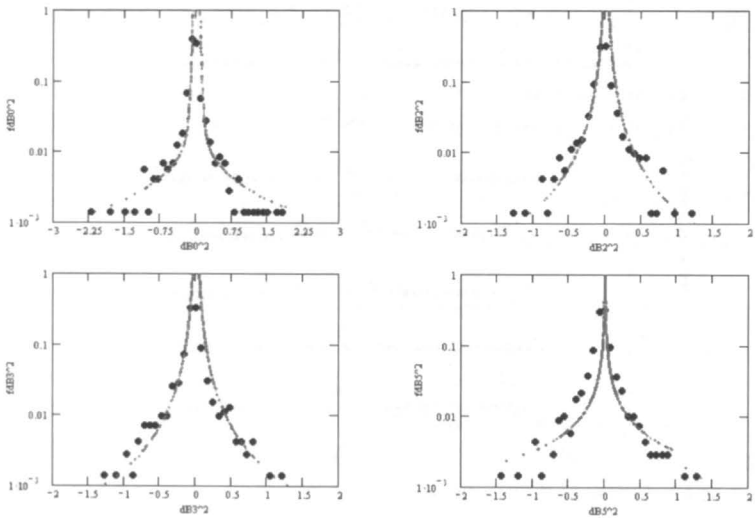

Fig. 7 – The observational (points) and theoretical PDFs - fdB_n^2 - for the scales $n = 0, 2, 3, 5$

4. CONCLUSIONS

Numerical solutions of space-time fractional diffusion equations have been used to analyze the presence or absence of heavy tails, typically associated with multiscale behavior, in the case of the interplanetary magnetic field data recorded by Ulysses mission (for the years 2002–2003). Analysis of the magnetic field intensity and magnetic energy density fluctuations shows that at larger scales the fluctuations are less intermittent than at small scales (here the fluctuations present spikes and bursts indicating intermittency). The changes of B and B^2 at different scales have been studied by means of PDFs, good fits of the observational PDFs being obtained. The probability distribution functions of the magnetic field intensity and magnetic energy density present non-Gaussian properties on small time scales, and uncorrelated features at large scale. Probabilistic predictions can be done for the dynamics and multiscale behaviour of the interplanetary magnetic field.

Acknowledgements. This work was supported by a grant of the Ministry of National Education and Scientific Research, RDI Program for Space Technology and Advanced Research - STAR/C3, project number 513 - Contract STAR Nr. 118/2016, ASTRES.

REFERENCES

Frisch, U.: 1995, *Turbulence. The legacy of A.N. Kolmogorov*, Cambridge University Press.
Mainardi, F., Luchko, Y. and Pagnini, G.: 2001, *Fractional Calculus Appl. Anal.* **4**, 153.
Taylor, G.I.: 1938, *Proc. R. Soc.Lon.Ser-A* **164**, 476.

Received on 30 October 2018

STABILITY OF REGULAR POLYGON SOLUTIONS IN n-BODY PROBLEMS WITH LOGARITHM POTENTIAL

ELI CAVAN[1], CRISTINA STOICA[2]

[1] *Wilfrid Laurier University, Waterloo, Canada*
Email: cava0920@mylaurier.ca
[2] *Wilfrid Laurier University*
Waterloo, Canada Email: cstoica@wlu.ca

Abstract. We show that in the n-body problem with logarithm binary interaction, regular n-gon solutions are linearly stable for $n = 3, 4, 7$ and unstable for $n = 6, 8, 9$ and any $n \geq 10$, n even. We study the linear stability of solutions with regular polygon configurations in the equal mass n-body problem with logarithm interaction. We find that the regular n-gon solution is linearly stable for $n = 3, 4, 7, 8$ and unstable for $n = 6, 9$ and any $n \geq 10$, n even. This is different with respect to the gravitational case, where such solutions are unstable for all n.

Key words: n-body problem – relative equilibria – regular n-gon stability – logarithm interaction.

1. INTRODUCTION

In this paper we study the spectral stability of solutions with regular polygon configurations in equal mass n-body problems with logarithm interaction. Specifically, we consider regular n-gon solutions of the system associated to the Hamiltonian

$$H(\mathbf{x}_1, \mathbf{x}_2, \ldots, \mathbf{x}_n, \mathbf{p}_1, \mathbf{p}_2, \ldots, \mathbf{p}_n) = \frac{1}{2}\sum_{j=1}^{n} \mathbf{p}_j^2 + \sum_{1 \leq j < k \leq n} \ln(|\mathbf{x}_j - \mathbf{x}_k|), \qquad (1)$$

where $\mathbf{x}_j \in \mathbb{R}^2$, $j = 1, 2, \ldots, n$, are the coordinates, and $\mathbf{p}_j$ the corresponding momenta.

The n-body problem with logarithmic interaction is often employed in astrophysics for the modeling of *planar* galaxies with large n-point masses; see, for instance, the book of Binney and Tremaine (1987). (Recall that that the solutions of the gravitational Poisson equation in $\mathbb{R}^2$ is the logarithm function.) The study of the orbital structure of the logarithmic potential was initially motivated by the need to construct self-consistent models of galaxies (see Schwarzschild (1979)). Numerical

investigations revealed the rich orbital structure of the dynamics, including the presence of the major orbit families, resonances and stochastic orbits. The general dynamics in a logarithm potential is a Hamiltonian systems with $H : \left(\mathbb{R}^{2n} \setminus \{\text{collisions}\}\right) \times \mathbb{R}^{2n} \to \mathbb{R}$

$$H(\mathbf{x}_1, \mathbf{x}_2, \ldots, \mathbf{x}_n, \mathbf{p}_1, \mathbf{p}_2, \ldots, \mathbf{p}_n) = \sum_{j=1}^{n} \frac{\mathbf{p}_j^2}{2m_j} + \sum_{1 \le j < k \le n} G m_j m_k \ln(|\mathbf{x}_j - \mathbf{x}_k|). \quad (2)$$

It is clear that of all points have unit mass, after some re-scaling, the Hamiltonian above coincide to that given in formula (1).

Another problem where the dynamics associated to the Hamiltonian (1) is relevant is the evolution of nearly parallel vortex filaments in fluid. Vortex filaments are thin curves or lines of vorticity embedded within a fluid caused by the rotational fluid motion, for example, by convection currents. When the interaction or containment forces are inadequate to keep the filaments perfectly parallel, one may approximates the filaments' disposition as considering them nearly parallel; for more on the modeling of filaments see the book of Andersen and Lim (1973).

In a standard cartesian $Oxyz$ system of coordinates, given n nearly parallel vortex filaments with parameterized positions

$$(\tau, z) \to \mathbf{x}_j(\tau, z) = (x_j(\tau, z), y_j(\tau, z)) \in \mathbb{R}^2.$$

The the equations for interacting filaments with *circulations* of strength Γ_k are

$$\frac{\partial \mathbf{x}_j}{\partial \tau} = \mathbb{J}\left[\alpha_j \Gamma_j \frac{\partial^2}{\partial z^2}\mathbf{x}_j + \sum_{k \ne j}^{N} 2\Gamma_k \frac{\mathbf{x}_j - \mathbf{x}_k}{|\mathbf{x}_j - \mathbf{x}_k|^2}\right], \quad (3)$$

where τ denotes time, $\mathbb{J} = \begin{bmatrix} 0 & 1 \\ -1 & 0 \end{bmatrix}$ is the symplectic operator and α_j are given constants. Considering $\alpha_j = 2$ for all j, simplifying by $\mathbb{J}$ and changing the notation of the coordinate z by t, the steady state solutions (*i.e.* solutions such that $\partial \mathbf{x}_j / \partial \tau \equiv 0$ for all τ) of the PDE above are found by solving the ODE system

$$\Gamma_j \frac{d\mathbf{x}_j}{dt^2} = -\sum_{k \ne j}^{n} \Gamma_k \frac{\mathbf{x}_j - \mathbf{x}_k}{|\mathbf{x}_j - \mathbf{x}_k|^2}, \quad j = 1, 2, \ldots, n. \quad (4)$$

Provided $\Gamma_j \ne 0$ for all j, the above equations correspond to those associated to a classical mechanical system with Hamiltonian $H : \left(\mathbb{R}^{2n} \setminus \{\text{overlaps}\}\right) \times \mathbb{R}^{2n} \to \mathbb{R}$,

$$H(\mathbf{x}_1, \mathbf{x}_2, \ldots, \mathbf{x}_n, \mathbf{p}_1, \mathbf{p}_2, \ldots, \mathbf{p}_n) = \sum_{j=1}^{n} \frac{\mathbf{p}_j^2}{2\Gamma_j^2} + \sum_{1 \le j < k \le n} \Gamma_j \Gamma_k \ln(|\mathbf{x}_j - \mathbf{x}_k|). \quad (5)$$

It is clear that for equal circulations $\Gamma_j = 1$ we retrieve the Hamiltonian (1).

For future reference we note that the Hamiltonian (1) leads to the equations of motion

$$\dot{\mathbf{x}}_j = \mathbf{p}_j\,, \qquad \dot{\mathbf{p}}_j = -\sum_{k=1,k\neq j}^{n} \frac{\mathbf{x}_j - \mathbf{x}_k}{|\mathbf{x}_j - \mathbf{x}_k|^2} \tag{6}$$

or, equivalently, to the second order ODE system

$$\ddot{\mathbf{x}}_j = -\sum_{k=1,k\neq j}^{n} \frac{\mathbf{x}_j - \mathbf{x}_k}{|\mathbf{x}_j - \mathbf{x}_k|^2}\,. \tag{7}$$

It is easy to observe (or reason from a physical standpoint), that, as in the classical n-body problem, the dynamics of (1) is invariant with respect to rotations of the coordinates and the velocities (or momenta) about the centre of mass. In general, given a n-body-type problem with rotational symmetry, equilibria and relative equilibria, *i.e.* rigidly rotating configurations (or, equivalently, equilibria in a uniformly rotating system), are the simplest solutions that can be determined. As organizing centres of the dynamics, their stability properties are essential and determine landscape features of the phase space. In general, an equilibrium is stable if solutions that start nearby remain nearby. Computationally, the most common way to determine stability consists in calculating the spectrum of the associated linear system; the latter is given by the algebraic roots of the characteristic polynomial of the linearization matrix.

An equilibrium is called *spectrally* stable if its eigenvalues are all pure imaginary and *linearly* stable, if in addition, the associated matrix is diagonalizable (and so, its nilpotent part is null). Linear stability does not ensure stability in the nonlinear system, but guarantees the stability (of the equilibrium) in the associated linear system; practically it leads to the the existence of the local normal modes, i.e. a decomposition of the local dynamics in simple harmonic motions. Reciprocally, spectral (and linear) instability predicts instability (for details on the stability of dynamical systems, see for instance, the textbook of Meiss (2007)).

In this paper, since we are dealing with a Hamiltonian system, the characteristic polynomial is even and consequently, equilibrium points are never asymptotically stable (Meyer and Hall (1992)). Also, within the class of n-body-type problems considered, the linearization at any relative equilibrium will have two zero eigenvalues that count for the conservation of the centre of weight (*i.e.* the centre of mass, or centre of circulations, depending on the problem). Thus, no relative equilibrium will ever be linearly stable. However, if one ignores the block of the two zero eigenvalues,

the remaining matrix is semi-simple (and so diagonalizable); it is a convention within the celestial mechanics community to call a relative equilibrium of the n-body problem linearly stable if the remaining block is diagonalizable (see Moeckel (1992)); we adopt this convention here.

It is known that the regular polygon solutions for problems with gravitational potential (and no central mass) and for $n \geq 4$ are always unstable (see, for instance, Robers (2000)). Also, the equilateral Lagrange triangle solution *with equal masses* is unstable (see, for instance, Schmah and Stoica (2006) and references within). In contrast, we find that when dealing with the logarithm interaction, the regular n-gon solutions are linearly stable for $n = 3, 4, 7$. Further, we show that regular polygonal solutions are unstable for $n = 6, 8, 9$ and any $n \geq 10$, n even. We leave for future investigations the case of $n \geq$ odd, as well as studies on the stability of the regular n-gon solutions with an additional weight positioned in centre.

To prove our results we follow closely the methodology in Vanderbei (2008). In Section 2 we determine the relationship between the angular velocity and the radius of a regular n-gon relative equilibrium. Next we calculate the matrix linearization and use its particular structure to determine the formula of the characteristic polynomial. We continue in Section 5 with calculating the eigenvalues associated to the first two deformation modes (where by a mode we understand a 4×4 block of the linearization matrix describing phase space deformations in two particular directions) and also those associated to the mode responsible for the lack of stability in the case $n \geq 10$, n even. Further, we calculate stability in the particular cases $n = 3, 4, \ldots, 9$.

2. EXISTENCE OF REGULAR n-GON-SHAPED REGULAR EQUILIBRIA

We start by introducing the complex plane and define $\mathbf{x}_j = (x, y) \equiv z = x_j + iy_j \in \mathbb{C}$ as coordinates. Next, we make the anzatz that the solutions of (7) take the form:

$$z_j = re^{i(\omega t + \theta_j)}, \ j = 0, 1, \ldots, (n-1) \tag{8}$$

where $\theta_j := \frac{2\pi j}{n}$. Note that

$$\begin{aligned} z_j - z_0 &= re^{i(\omega t + \theta_j)} - re^{i(\omega t)} = re^{i(\omega t)} e^{i\left(\frac{\theta_j}{2}\right)} \left(e^{i\left(\frac{\theta_j}{2}\right)} - e^{-i\left(\frac{\theta_j}{2}\right)} \right) \\ &= re^{i(\omega t)} e^{i\left(\frac{\theta_j}{2}\right)} 2i \sin\left(\frac{\theta_j}{2}\right), \end{aligned}$$

and so

$$|z_j - z_0| = 2r \sin\left(\frac{\theta_j}{2}\right).$$

We differentiate (8) to find the velocity and acceleration of the vortices

$$\dot{z}_j = i\omega r e^{i(\omega t+\theta_j)}, \quad \ddot{z}_j = -\omega^2 r e^{i(\omega t+\theta_j)} \text{ for } j = 0, 1, \ldots (n-1). \tag{9}$$

(10)

Substituting (10) into (7), we obtain:

$$-\omega^2 r^2 = \sum_{k=1, k\neq j}^{n-1} \frac{e^{i\theta_k} - 1}{|e^{i\theta_k} - 1|^2} = \sum_{k=1, k\neq j}^{n-1} \frac{1}{2} + \sum_{k=1}^{n-1} \frac{i \cos\frac{\theta_k}{2}}{\sin\frac{\theta_k}{2}}.$$

It can be shown that the imaginary part of the sum above is zero. Thus we obtain the relation between the angular velocity ω and the radius of a regular polygon solution

$$\omega^2 = \frac{1}{2r^2}(n-1). \tag{11}$$

3. FIRST AND SECOND ORDER VARIATIONS

We perform a counter rotation of the system by redefining our coordinates. In this frame, the vortices of strength Γ are stationary, and lie on the x axis of the complex plane; also radial perturbations occur on the real axis while azimuthal perturbations occur on the imaginary axis. For $j = 0, 1, \ldots, n$ we define new coordinates:

$$w_j = u_j + iw_j = e^{-i(\omega t+\theta_j)} z_j. \tag{12}$$

Taking time derivatives we find:

$$\dot{w}_j = -i\omega e^{-i(\omega t+\theta_j)} z_j + e^{-i(\omega t+\theta_j)} \dot{z}_j$$

$$\ddot{w}_j = \omega^2 w_j - 2i\omega \dot{w}_j + e^{-i(\omega t+\theta_j)} \ddot{z}_j.$$

Substituting into the equations (7) we obtain

$$\ddot{w}_j = \omega^2 w_j - 2i\omega \dot{w}_j + \sum_{k=0, k\neq j}^{n-1} \frac{\epsilon_{k,j}}{|\epsilon_{k,j}|^2}, \tag{13}$$

where

$$\epsilon_{k,j} := e^{i\theta_{k-j}} w_k - w_j. \tag{14}$$

Taking the variations of (13) we have

$$\delta\ddot{w}_j = \omega^2 \delta w_j - 2i\omega \delta \dot{w}_j + \sum_{k=0, k\neq j}^{n-1} \delta \frac{\epsilon_{k,j}}{|\epsilon_{k,j}|^2}. \tag{15}$$

For future reference, we observe that

$$\epsilon_{k,j} = e^{i\theta_{k-j}} w_k - w_j = r(e^{i\theta_{k-j}} - 1),\ k,j = 0,1,\ldots,(n-1), \tag{16}$$

$$\epsilon_{n,j} = -r,\ j = 0,1,\ldots,(n-1), \tag{17}$$

$$|\epsilon_{k,j}| = 2r\sin\left(\frac{\theta_{k-j}}{2}\right),\ k,j = 0,1,\ldots,(n-1), \tag{18}$$

$$|\epsilon_{n,j}| = r,\ j = 0,1,\ldots,(n-1), \tag{19}$$

$$\delta\epsilon_{k,j} = e^{i\theta_{k-j}}\delta w_k - \delta w_j, \tag{20}$$

$$\delta\epsilon_{\bar{k},j} = e^{-i\theta_{k-j}}\delta\bar{w}_k - \delta\bar{w}_j, \tag{21}$$

and further, since

$$\delta\left(|\epsilon_{k,j}|^2\right) = \delta\left(\epsilon_{k,j}\epsilon_{\bar{k},j}\right) = \epsilon_{k,j}\delta\epsilon_{\bar{k},j} + \epsilon_{\bar{k},j}\delta\epsilon_{k,j} \quad \text{and} \quad \delta\left(|\epsilon_{k,j}|^2\right) = 2|\epsilon_{k,j}|\delta\left(|\epsilon_{k,j}|\right).$$

that

$$|\epsilon_{k,j}|\delta\left(|\epsilon_{k,j}|\right) = \frac{1}{2}\left(\epsilon_{k,j}\delta\epsilon_{\bar{k},j} + \epsilon_{\bar{k},j}\delta\epsilon_{k,j}\right). \tag{22}$$

Using the above, we obtain

$$\begin{aligned}
\delta\left(\frac{\epsilon_{k,j}}{|\epsilon_{k,j}|^2}\right) &= \frac{\delta\epsilon_{k,j}}{|\epsilon_{k,j}|^2} - \frac{2\epsilon_{k,j}\delta(|\epsilon_{k,j}|)}{|\epsilon_{k,j}|^3} \\
&= \frac{\delta\epsilon_{k,j}}{|\epsilon_{k,j}|^2} - \frac{2\epsilon_{k,j}|\epsilon_{k,j}|\delta(|\epsilon_{k,j}|)}{|\epsilon_{k,j}|^4} \\
&= \frac{\delta\epsilon_{k,j}}{|\epsilon_{k,j}|^2} - \frac{\epsilon_{k,j}\left(\epsilon_{k,j}\delta\epsilon_{\bar{k},j} + \epsilon_{\bar{k},j}\delta\epsilon_{k,j}\right)}{|\epsilon_{k,j}|^4} \\
&= \frac{\delta\epsilon_{k,j}}{|\epsilon_{k,j}|^2} - \frac{\epsilon_{k,j}^2\delta\epsilon_{\bar{k},j}}{|\epsilon_{k,j}|^4} - \frac{\epsilon_{k,j}\epsilon_{\bar{k},j}\delta\epsilon_{k,j}}{|\epsilon_{k,j}|^4} = -\frac{\epsilon_{k,j}^2\delta\epsilon_{\bar{k},j}}{|\epsilon_{k,j}|^4}.
\end{aligned} \tag{23}$$

Also, using (16) – (21), we get

$$\delta\left(\frac{\epsilon_{k,j}}{|\epsilon_{k,j}|^2}\right) = -\frac{\epsilon_{k,j}^2\delta\epsilon_{\bar{k},j}}{|\epsilon_{k,j}|^4} = \begin{cases} \dfrac{\delta\bar{w}_k - e^{-i\theta_{k-j}}\delta\bar{w}_j}{4r^2\sin^2\left(\frac{\theta_{k-j}}{2}\right)} & \text{for } k,j = 0,1,\ldots,(n-1), k \neq j, \\ \dfrac{\delta\bar{w}_n - e^{-i\theta_{n-j}}\delta\bar{w}_j}{r^2} & \text{for } j = 0,1,\ldots,(n-1). \end{cases} \tag{24}$$

Substituting into (15) we calculate for each $j = 0,1,\ldots,(n-1)$

$$\delta\ddot{w}_j = \omega^2\delta w_j - 2i\omega\delta\dot{w}_j + \sum_{k=0,k\neq j}^{n-1} \frac{\delta\bar{w}_k - e^{-i\theta_{k-j}}\delta\bar{w}_j}{4r^2\sin^2\left(\frac{\theta_{k-j}}{2}\right)}. \tag{25}$$

4. THE LINEARIZED SYSTEM AND THE EIGENVALUE EQUATIONS

The conjugate of (25) is

$$\delta\ddot{\bar{w}}_j = \omega^2\delta\bar{w}_j + 2i\omega\delta\dot{\bar{w}}_j + \sum_{k=0,k\neq j}^{n-1} \frac{\delta w_k - e^{i\theta_{k-j}}\delta w_j}{4r^2\sin^2\left(\frac{\theta_{k-j}}{2}\right)}. \tag{26}$$

Let W_j be the vector $\begin{pmatrix} w_j \\ \bar{w}_j \end{pmatrix} \in \mathbb{C}\times\mathbb{C}$. Let us denote by I and $0_{2,2}$ the 2×2 identity and zero matrices, respectively. Then (25)-(26) can be written in matrix form as

$$\frac{\mathrm{d}}{\mathrm{d}t}\begin{pmatrix} \delta W_0 \\ \delta W_1 \\ \delta W_2 \\ \dots \\ \delta W_{n-1} \\ \delta\dot{W}_0 \\ \delta\dot{W}_1 \\ \delta\dot{W}_2 \\ \dots \\ \delta\dot{W}_{n-1} \end{pmatrix} =$$

$$= \left[\begin{array}{ccccc|ccccc} & & \mathbf{0}_{2n,2n} & & & I & 0_{2,2} & 0_{2,2} & 0_{2,2} & \dots \\ & & & & & 0_{2,2} & I & 0_{2,2} & 0_{2,2} & \dots \\ & & & & & \dots & \dots & \dots & \dots & \dots \\ & & & & & 0_{2,2} & 0_{2,2} & 0_{2,2} & \dots. & I \\ \hline D & N_1 & N_2 & \dots & N_{n-1} & \Omega & 0_{2,2} & 0_{2,2} & 0_{2,2} & \dots \\ N_{n-1} & D & N_1 & N_2 & \dots & 0_{2,2} & \Omega & 0_{2,2} & 0_{2,2} & \dots \\ \dots & \dots & \dots & \dots & \dots & \dots & \dots & \dots & \dots & \dots \\ N_1 & N_2 & & N_{n-1} & D & 0_{2,2} & 0_{2,2} & 0_{2,2} & & \Omega \end{array}\right] \cdot \begin{pmatrix} \delta W_0 \\ \delta W_1 \\ \delta W_2 \\ \dots \\ \delta W_{n-1} \\ \delta\dot{W}_0 \\ \delta\dot{W}_1 \\ \delta\dot{W}_2 \\ \dots \\ \delta\dot{W}_{n-1} \end{pmatrix} \tag{27}$$

with

$$D = \omega^2\begin{pmatrix} 1 & 0 \\ 0 & 1 \end{pmatrix} - \begin{pmatrix} 0 & A \\ \bar{A} & 0 \end{pmatrix}, \quad N_k = \frac{1}{4r^2\sin^2\frac{\theta_k}{2}}\begin{pmatrix} 0 & 1 \\ 1 & 0 \end{pmatrix}, \quad \Omega = 2i\omega\begin{pmatrix} -1 & 0 \\ 0 & 1 \end{pmatrix}, \tag{28}$$

where we calculate

$$A_j := \sum_{k=0,k\neq j}^{n-1} \frac{e^{-i\theta_{k-j}}}{4r^2 \sin^2 \frac{\theta_{k-j}}{2}} = \sum_{k=1}^{n-1} \frac{e^{-i\theta_k}}{4r^2 \sin^2 \frac{\theta_k}{2}} \tag{29}$$

$$= \frac{1}{4r^2}\left(\sum_{k=1}^{n-1} \frac{1}{\sin^2 \frac{\theta_k}{2}} - 2(n-1)\right)$$

$$= \frac{1}{4r^2}\left(\sigma_n - 2(n-1)\right) \tag{30}$$

$$= \frac{1}{4r^2}\left(\frac{n^2-1}{3} - 2(n-1)\right)$$

$$= \frac{(n-1)(n-5)}{12r^2}$$

$$= \frac{(n-1)(n-5)}{12}\frac{2\omega^2}{(n-1)}$$

$$= \frac{\omega^2(n-5)}{6} =: A \tag{31}$$

and use that

$$\sigma_n := \sum_{k=1}^{n-1} \frac{1}{\sin^2 \frac{\theta_k}{2}} = \frac{n^2-1}{3}, \tag{32}$$

and that $\sin \dfrac{\theta_{k-j}}{2} = \sin \dfrac{\theta_{n+k-j}}{2}$ if $k-j<0$. Consider

$$M := \begin{bmatrix} D & N_1 & N_2 & \dots & N_{n-1} \\ N_{n-1} & D & N_1 & N_2 & \dots \\ \dots & \dots & \dots & \dots & \dots \\ N_1 & N_2 & & N_{n-1} & D \end{bmatrix}. \tag{33}$$

The eigenvalues $\lambda \in \mathbb{C}$ and eigenvectors $(U\ V) \in \mathbb{C}^{2n} \times \mathbb{C}^{2n}$ of the linearization matrix (27) are found by solving

$$\left[\begin{array}{c|c} \operatorname{diag} 0_{2,2} & \operatorname{diag} I \\ \hline M & \operatorname{diag} \Omega \end{array}\right] \begin{pmatrix} U \\ V \end{pmatrix} = \lambda \begin{pmatrix} U \\ V \end{pmatrix}. \tag{34}$$

We deduce that

$$V = \lambda U, \quad \text{and } MU + (\operatorname{diag}\Omega)V = \lambda V \tag{35}$$

from where

$$MU + \lambda(\operatorname{diag}\Omega)U = \lambda^2 U. \tag{36}$$

Given that M is a circulant matrix, the eigenvectors can be found by assuming that they take the form

$$U = \begin{pmatrix} \xi \\ \rho\xi \\ \vdots \\ \rho^{n-1}\xi \end{pmatrix} \tag{37}$$

where $\rho_j = e^{i2\pi j/n} = e^{i\theta_j}$ for some $j \in \{0, 1, ,\ldots, (n-1)\}$ fixed (*i.e.* ρ is a n-th root of unity) and $\xi = (\xi_1\ \xi_2) \in \mathbb{C} \times \mathbb{C}$. Substituting into (36) and recalling the definition of M we find that we need to solve

$$(D + \rho_j N_1 + \rho_j^2 N_2 + \ldots + \rho_j^{n-1} N_{n-1})\xi + \lambda\Omega\xi = \lambda^2\xi\,. \tag{38}$$

This system has nontrivial solutions if

$$\det(D + \rho_j N_1 + \rho_j^2 N_2 + \ldots + \rho_j^{n-1} N_{n-1} + \lambda\Omega - \lambda^2 I) = 0\,, \tag{39}$$

that is

$$\det\begin{pmatrix} -\lambda^2 + \omega^2 - 2\omega i\lambda & C_j - A \\ C_j - \bar{A} & -\lambda^2 + \omega^2 + 2\omega i\lambda \end{pmatrix} = 0\,. \tag{40}$$

where we denote

$$C_j := \sum_{k=1}^{n-1} \frac{\rho_j^k}{4r^2 \sin^2 \frac{\theta_k}{2}} \tag{41}$$

The above is equivalent to

$$\lambda^4 + 2\omega^2\lambda^2 + \omega^4 - (C_j - A)\left(C_j - \bar{A}\right) = 0 \tag{42}$$

which leads to

$$\lambda^4 + 2\omega^2\lambda^2 + \omega^4 - \left[C_j^2 - 2C_j\,\mathrm{Re}A + |A|^2\right] = 0\,. \tag{43}$$

For each root of unity, ρ_j, there are four values of λ that solve this equation (counting multiplicites). That makes a total of $4n$ eigenvalues and therefore provides all eigenvalues of the linearization matrix in (27).

Taking onto account the formula (31) of A, the equation (43) becomes

$$\lambda^4 + 2\omega^2\lambda^2 + \omega^4 - \left(C_j^2 - 2C_jA + A^2\right) = 0\,. \tag{44}$$

Denoting $y := \lambda^2$, the equation above writes

$$y^2 + 2\omega^2 y + \omega^4 - (C_j - A)^2 = 0\,. \tag{45}$$

The (44) equation has all roots purely imaginary only if the equation (45) above has both roots y_1 and y_2 (real and) negative. Otherwise, some roots have non-zero real

part and so the associated equilibrium is unstable. The discriminant of the above quadratic is:

$$\Delta_j = 4\,(C_j - A)^2 \geq 0. \tag{46}$$

and so the equation (45) always has real roots. These are negative only if each $S_j = y_1 + y_2$ and the product $P_j := y_1 y_2$ are, respectively, negative and positive for all j. We calculate

$$S_j = y_1 + y_2 = -2\omega^2 \leq 0 \tag{47}$$

so it is sufficient for the P_j to be are negative. We have

$$P_j := y_1 y_2 = \omega^4 - (C_j - A)^2 \tag{48}$$

which we will use for further calculations.

5. EXPLICIT FORMULAE FOR VARIOUS MODES

5.1. EXPLICIT FORMULAE FOR $j = 0$

For $j = 0$, since $\rho_0 = 1$, we calculate:

$$C_0 = \sum_{k=1}^{n-1} \frac{\rho_0^k}{4r^2 \sin^2 \frac{\theta_k}{2}} = \sum_{k=1}^{n-1} \frac{1}{4r^2 \sin^2 \frac{\theta_k}{2}} = \frac{\sigma_n}{4r^2} = \frac{n^2-1}{12r^2} = \frac{n^2-1}{12} \frac{2\omega^2}{(n-1)} = \\ = \frac{\omega^2(n+1)}{6}. \tag{49}$$

Thus

$$P_0 = \omega^4 - (C_0 - A)^2 = \omega^4 - \left(\frac{\omega^2(n+1)}{6} - \frac{\omega^2(n-5)}{6} \right)^2 \\ = \omega^4 - \frac{\omega^4}{36} [n+1-(n-5)]^2 = \omega^4 - \omega^4 = 0 \geq 0. \tag{50}$$

So $y_1 = 0$ and, since $\mathrm{Sum}_0 < 0$, we have $y_2 < 0$. Thus all eigenvalues associated to $j = 0$ are zero or imaginary. In fact, these eigenvalues can be calculate and they are

$$\lambda_{1,2} = \pm i\omega\sqrt{2}, \quad \lambda_{3,4} = 0. \tag{51}$$

5.2. EXPLICIT FORMULAE FOR $j = 1$

For $j = 1$, since $\rho_1 = e^{i\theta_1} = e^{\frac{2i\pi}{n}}$, we obtain

$$C_1 = \sum_{k=1}^{n-1} \frac{\rho_1^k}{4r^2 \sin^2 \frac{\theta_k}{2}} = \sum_{k=1}^{n-1} \frac{e^{i\theta_k}}{4r^2 \sin^2 \frac{\theta_k}{2}} = \frac{\sigma_n - 2(n-1)}{4r^2} = \frac{\omega^2(n-5)}{6}. \tag{52}$$

Thus

$$P_1 = \omega^4 - (C_1 - A)^2 = \omega^4 - \left(\frac{\omega^2(n-5)}{6} - \frac{\omega^2(n-5)}{6}\right)^2$$
$$= \omega^4 - 0 = \omega^4 \geq 0. \tag{53}$$

Thus all eigenvalues associated to $j = 0$ are zero or imaginary. In fact, these eigenvalues can be calculate and they are

$$\lambda_{1,2,3,4} = \pm i\omega. \tag{54}$$

5.3. EXPLICIT FORMULAE FOR $j = n - 1$

For $j = n - 1$, we have since $\rho_{n-1} = e^{i\theta_{n-1}} = e^{\frac{2(n-1)\imath\pi}{n}} = e^{\frac{-2\imath\pi}{n}} = e^{-i\theta_1} = e^{i(-\theta_1)}$ and so, since

$$C_{n-1} = \sum_{k=1}^{n-1} \frac{\rho_{n-1}^k}{4r^2 \sin^2 \frac{\theta_k}{2}} = \sum_{k=1}^{n-1} \frac{e^{i(-\theta_k)}}{4r^2 \sin^2 \frac{\theta_k}{2}} =$$
$$= \sum_{k=1}^{n-1} \frac{e^{i\theta_{(-k)}}}{4r^2 \sin^2 \frac{\theta_k}{2}} = \sum_{k=1}^{n-1} \frac{e^{i\theta_{(n-k)}}}{4r^2 \sin^2 \frac{\theta_k}{2}} = \sum_{j=1}^{n-1} \frac{e^{i\theta_j}}{4r^2 \sin^2 \frac{\theta_k}{2}}$$

the case $j = 1$ coincides to the case $j = n - 1$.

5.4. EXPLICIT FORMULAE FOR $j = n/2$ FOR n EVEN

Let $n = 2p$ for some $p \in \mathbb{N}$, $p \geq 2$. Thus $j = n/2 = p$, and so $\rho_{n/2} = e^{\frac{2\imath\pi n}{2n}} = e^{\frac{2i\pi 2p}{4p}} = e^{i\pi} = -1$ and so,

$$C_{n/2} = \frac{(-1)^p}{4r^2} = \frac{(-1)^p \omega^2}{2(n-1)}. \tag{55}$$

Thus

$$P_{n/2} = \omega^4 - \omega^4 \left(\frac{(-1)^p}{2(n-1)} - \frac{n-5}{6}\right)^2 = \omega^4 \left[1 - \left(\frac{(-1)^p}{2(n-1)} - \frac{n-5}{6}\right)^2\right]$$
$$= \omega^4 \left(1 - \frac{(-1)^p}{2(n-1)} + \frac{n-5}{6}\right)\left(1 + \frac{(-1)^p}{2(n-1)} - \frac{n-5}{6}\right)$$
$$= \omega^4 \left(1 - \frac{(-1)^p}{2(n-1)} + \frac{n-5}{6}\right)\left(1 + \frac{(-1)^p}{2(n-1)} - \frac{n-5}{6}\right)$$
$$= \begin{cases} -(n^2-4)(n^2-12n+8) & \text{for } p \text{ even}, \\ -(n^2+2)(n^2-12n+14) & \text{for } p \text{ odd}. \end{cases} \tag{56}$$

We obtain that $P_{n/2} < 0$ for all $n \geq 10$, n even and so

Lemma 5.1 *The regular n-gon-shaped solution is unstable for any $n \geq 10$ even.*

6. PARTICULAR CASES

In this section we calculate linear stability for the regular n-gon solutions of (7) for $n = 3, 4, \ldots 9$. To ease notation, we use $C_{n,j}$, $P_{n,j}$ to denote (41) and (48) for the corresponding n.

6.1. THE CASES $n = 3$ AND $n = 4$

Applying the results of the Subsections 5.1, 5.2 and 5.3 all eigenvalues are purely imaginary and so the equilateral triangle and square solutions of (7) are linearly stable.

6.2. THE CASE $n = 5$

It is immediate that for $j = 0, 1, 4$ all eigenvalues are imaginary. We calculate

1. for $j = 2$:

$$C_{5,2} = \sum_{k=1}^{4} \frac{(e^{4i\pi/5})^k}{4r^2 \sin^2 \frac{\theta_k}{2}} = \frac{e^{4i\pi/5}}{4r^2 \sin^2(\pi/5)} + \frac{e^{8i\pi/5}}{4r^2 \sin^2(2\pi/5)} + \frac{e^{12i\pi/5}}{4r^2 \sin^2(3\pi/5)} + \frac{e^{16i\pi/5}}{4r^2 \sin^2(4\pi/5)} = -\frac{1}{r^2}$$

and

$$P_{5,2} = \omega^4 - [C_{5,2} - A] = \frac{(5-1)^2}{4r^4} - \left[-\frac{1}{r^2} - \frac{(5-1)(5-5)}{12r^2}\right]^2 = \frac{4}{r^4} - \frac{1}{r^4} = \frac{3}{r^4} > 0$$

hence all associated eigenvalues are imaginary;

2. for $j = 3$, by symmetry, we have

$$C_{5.3} = C_{5.2}$$

and so $P_{5,3} = P_{5,2} > 0$. Hence all associated eigenvalues are imaginary.

Thus, since all eigenvalues are imaginary, the regular pentagon solution is linearly stable.

6.3. THE CASE $n = 6$

The eigenvalues corresponding to $j = 0, 1, 3, 5$ are imaginary. We calculate

1. for $j = 2$:

$$C_{6,2} = \sum_{k=1}^{5} \frac{(e^{4i\pi/6})^k}{4r^2 \sin^2 \frac{\theta_k}{2}} = -\frac{13}{12r^2}$$

and

$$P_{6,2} = \omega^4 - [C_{6,2} - A]^2 = \frac{(6-1)^2}{4r^4} - \left[-\frac{13}{12r^2} - \frac{(6-1)(6-5)}{12r^2}\right]^2 =$$
$$= \frac{25}{4r^4} - \frac{36}{r^4} < 0$$

hence two associated eigenvalues have non-zero real part.

Overall, we obtain that the regular hexagon solution is unstable.

6.4. THE CASE $n = 7$

The eigenvalues corresponding to $j = 0, 1, 6$ are imaginary. We calculate

1. for $j = 2$:

$$C_{7,2} = \sum_{k=1}^{6} \frac{(e^{4i\pi/7})^k}{4r^2 \sin^2 \frac{\theta_k}{2}} = -\frac{1}{r^2}$$

and

$$P_{7,2} = \omega^4 - [C_{7,2} - A]^2 = \frac{(7-1)^2}{4r^4} - \left[-\frac{1}{r^2} - \frac{(7-1)(7-5)}{12r^2}\right]^2 =$$
$$= \frac{36}{4r^4} - \frac{9}{4r^4} > 0$$

hence the associated eigenvalues are imaginary;

2. for $j = 3$:

$$C_{7,3} = \sum_{k=1}^{5} \frac{(e^{6i\pi/7})^k}{4r^2 \sin^2 \frac{\theta_k}{2}} \simeq -\frac{3.12}{4r^2}$$

and

$$P_{7,3} = \omega^4 - [C_{7,3} - A]^2 \simeq \frac{(7-1)^2}{4r^4} - \left[-\frac{3.12}{4r^2} - \frac{(7-1)(7-5)}{12r^2}\right]^2$$
$$\simeq \frac{9}{r^4} - \frac{(7.12)^2}{16r^4} > 0$$

hence the associated eigenvalues are imaginary;

3. for $j = 4$: by symmetry $C_{7,4} = C_{7,3}$, $P_{7,4} = P_{7,3}$. The associated eigenvalues are imaginary;
4. for $j = 5$: by symmetry, $C_{7,5} = C_{7,2}$m $P_{7,5} = P_{7,2}$. The associated eigenvalues are imaginary.

In conclusion the regular hexagon solution is linearly stable.

6.5. THE CASE $n = 8$

For $j = 0, 1, 4, 7$ all eigenvalues are imaginary.

We calculate

1. for $j = 2$:

$$C_{8,2} = \sum_{k=1}^{7} \frac{(e^{4i\pi/8})^k}{4r^2 \sin^2 \frac{\theta_k}{2}} = -\frac{3}{4r^2}$$

and

$$P_{8,2} = \omega^4 - [C_{8,2} - A]^2 = \frac{(8-1)^2}{4r^4} - \left[-\frac{3}{4r^2} - \frac{(8-1)(8-5)}{12r^2}\right]^2 =$$
$$= \frac{49}{4r^4} - \frac{25}{4r^4} > 0$$

hence all associated eigenvalues are imaginary;

2. for $j = 3$:

$$C_{8,3} = \sum_{k=1}^{7} \frac{(e^{6i\pi/8})^k}{4r^2 \sin^2 \frac{\theta_k}{2}} = -\frac{9}{4r^2}$$

and

$$P_{8,3} = \omega^4 - [C_{8,3} - A]^2 = \frac{(8-1)^2}{4r^4} - \left[-\frac{9}{4r^2} - \frac{(8-1)(8-5)}{12r^2}\right]^2 =$$
$$= \frac{49}{4r^4} - \frac{16}{r^4} < 0.$$

Two of the associated eigenvalues have non-zero real part.

We deduce that the regular octagon solution is unstable.

6.6. THE CASE $n = 9$

For $j = 0, 1, 8$ all eigenvalues are imaginary.

We calculate

1. for $j = 2$:

$$C_{9,2} = \sum_{k=1}^{8} \frac{(e^{4i\pi/9})^k}{4r^2 \sin^2 \frac{\theta_k}{2}} = -\frac{1}{3r^2}$$

and

$$P_{9,2} = \omega^4 - [C_{9,2} - A]^2 = \frac{(9-1)^2}{4r^4} - \left[-\frac{1}{3r^2} - \frac{(9-1)(9-5)}{12r^2}\right]^2 =$$
$$= \frac{16}{r^4} - \frac{9}{r^2} > 0$$

hence all associated eigenvalues are imaginary;

2. for $j = 3$:

$$C_{9,3} = \sum_{k=1}^{8} \frac{(e^{6i\pi/9})^k}{4r^2 \sin^2 \frac{\theta_k}{2}} = -\frac{7}{3r^2}$$

and

$$P_{9,3} = \omega^4 - [C_{9,3} - A]^2 = \frac{(9-1)^2}{4r^4} - \left[-\frac{7}{3r^2} - \frac{(9-1)(9-5)}{12r^2}\right]^2 =$$
$$= \frac{16}{r^4} - \frac{25}{r^4} < 0$$

hence two eigenvalues are non-zero real part.

Thus the regular 9-gon solution is unstable.

Using Lemma 5.1 and the previous results, we conclude by stating:

Proposition 6.1 *The regular n-gon solution for the second oder ODE systems* (7) *is linearly stable for* $n = 3, 4, 7$ *and unstable for* $n = 6, 8, 9$ *and any* $n \geq 10$, n *even.*

Acknowledgements. CS work was supported by a NSERC Discovery grant. EC completed part of this work during a MSc program at Wilfrid Laurier University.

REFERENCES

Andersen, T.D. and Lim, C.C.: 2014, *Introduction to Vortex Filaments in Equilibrium* Springer Monographs in Mathematics.

Binney, J. and Tremaine S.: 1987, *Galactic Dynamics*, Princeton University Press.

Roberts, G.E.: 2000, *Hamiltonian Systems and Celestial Mechanics (HAMSYS-98), Proceedings of the III International Symposium*, Patzcuaro, Mexico. World Scientific Monograph Series in Mathematics **6**, 303.

Maxwell, J. C.: 1890, *Stability of the motion of Saturn's rings* ,The Scientific Papers of James Clerk Maxwell ed. W D Niven, Cambridge University Press.

Meiss, J.D: 2007, *Differential Dynamical Systems*, SIAM, Philadelphia.

Meyer, K. and Hall, G. R.: 1992, Applied Mathematical Sciences **90**, Springer New York.

Moeckel, R.: 1992, *Journal of Dynamics and Differential Equations* **6**, 43.

Vanderbei, R. J.: 2008, *Linear stability of ring systems around oblate central masses*, Advances in Space Research **42**, 1370.

Schmah T., Stoica C.: 2006, *Journal of Physics: Mathematical and General* **bf 39**, 14405.

Schwarzschild, M.: 1979, *Astrophys.J.* **232236**.

Received on 1 November 2018

A NOTE ON THE GEOMETRIC MODELING OF THE FULL TWO BODY PROBLEM

TANYA SCHMAH[1], CRISTINA STOICA[2]

[1] *University of Ottawa, Ottawa, Canada*
Email: tschmah@uottawa.ca
[2] *Wilfrid Laurier University, Waterloo, Canada*
Email: cstoica@wlu.ca

Abstract. The two full body problem concerns the dynamics of two spatially extended rigid bodies (*e.g.* rocky asteroids) subject to mutual gravitational interaction. In this note we deduce the Euler-Poincaré and Hamiltonian equations of motion using the geometric mechanics formalism.

Key words: full two body problem – Euler-Poincaré reduction – Hamiltonian – Poisson bracket.

1. INTRODUCTION

It is well known that the classical two body problem, in which the bodies are idealized as mass points, can be analysed with almost elementary methods. Once the "mass-point" assumption is dropped, one is faced with a significantly more complex problem: a coupled, nonlinear 12 degrees of freedom system with a configuration space given by the product of two $SO(3)$ Lie groups and two copies of $\mathbb{R}^3$. The main inconvenience in modeling resides in the lack of a global chart for $SO(3)$; for this reason, even for a single rigid body, most classical mechanics textbooks use Euler angles or alike, leading to an intricate presentation; see for example, Iacob (1980).

Anticipating future developments in the aerospace industry, the full two body problem was studied extensively in the last decades; see for instance, Maciejewski (1995), Koon *et al.* (2004), Scheeres (2006), Bellerose and Scheeres (2008), Scheeres (2009), Hou and Xin (2018) and references within. The modeling of the problem within the geometric mechanics framework is developed in Cendra and Marsden (2004). However, this presentation uses extensively the geometric formalism at an abstract level. In this note we provide a description of the full two body problem within the geometric mechanics framework working *directly* in the full two body problem phase space, and thus avoiding abstract generalizations.

We start our modeling by assuming that the reduction due to the linear translation symmetry has already been performed and that the centre of mass coincides with the origin of the inertial system of coordinates. We write the Lagrangian, observe the $SO(3)$ symmetry and state and prove the appropriate (Euler-Poincaré) reduction theorem. We continue by computing the Euler equations. Next, we apply the reduced Legendre transform and deduce the Poisson structure of the reduced space, the Hamiltonian, and the equations of motion. Finally, we deduce the Casimir invariant as a consequence of the conservation of the size of the spatial angular momentum. We also include a small appendix with some formulae concerning the potential.

2. MODELING AND EQUATIONS OF MOTION

Consider two rigid bodies moving freely in space, with a coupling (gravitational) potential V depending on the orientations of the bodies and the relative position $\mathbf{r}$ of their centres of mass. Choose a spatial coordinate system with origin at the centre of mass of the entire system, which we assume remains fixed. Let $\mathbf{r}_i$ be the vector from the centre of mass of the system to the centre of mass of body i, for each i. Let $\mathbf{r} = \mathbf{r}_2 - \mathbf{r}_1$. Let $\mathcal{B}_1$ and $\mathcal{B}_2$, both subsets of $\mathbb{R}^3$, be the reference configurations of the two rigid bodies, each equipped with a reference frame defining *body coordinates*, with origin at the body's centre of mass. A configuration of the system is determined by $(R_1, R_2, \mathbf{r})$, where R_i specifies a rotation of body i from its reference configuration, around its own centre of mass (see, for instance, Marsden and Ratiu (1999)). The configuration space of the system is $Q := SO(3) \times SO(3) \times \mathbb{R}^3 \setminus \{\text{collisions}\}$, where $SO(3)$ denotes the Lie group of spatial rotations.

Let μ_i be the mass measure for body i, for $i = 1, 2$. Then the total mass of body i is

$$m_i := \int_{\mathcal{B}_i} d\mu_i.$$

The translational kinetic energy of body i is $\frac{1}{2} m_i \|\dot{\mathbf{r}}_i\|^2$. Following the centre of mass reduction, the *reduced mass* is $m := \frac{m_1 m_2}{m_1 + m_2}$ and the total translational kinetic energy of the system is $\frac{1}{2} m \|\dot{\mathbf{r}}\|^2$.

The *coefficient of inertia matrix* of body i, with respect to its own centre of mass, is

$$\mathbb{J}_i := \int_{\mathcal{B}_i} X X^t \, d\mu_i(X),$$

where $(\cdot)^t$ denotes the matrix transpose.

The body angular velocities are $\hat{\Omega}_i := R_i^{-1}\dot{R}_i$.

The rotational kinetic energy of body i is

$$K_i = \frac{1}{2}\left\langle \dot{R}_i, \dot{R}_i \right\rangle_i := \frac{1}{2}\operatorname{tr}\left(\dot{R}_i \mathbb{J}_i \dot{R}_i^t\right) \quad = \frac{1}{2}\operatorname{tr}\left(\left(R_i^{-1}\dot{R}_i\right)\mathbb{J}_i\left(R_i^{-1}\dot{R}_i\right)^t\right)$$
$$= \frac{1}{2}\operatorname{tr}\left(\hat{\Omega}_i \mathbb{J}_i \hat{\Omega}_i^t\right) =: \frac{1}{2}\left\langle \hat{\Omega}_i, \hat{\Omega}_i \right\rangle_i .$$

The *moment of inertia tensors* are

$$\mathbb{I}_i := \operatorname{tr}(\mathbb{J}_i)\,\mathrm{Id}_3 - \mathbb{J}_i , \tag{1}$$

where Id_3 is the 3×3 identity matrix. Using the usual identification of the Lie algebra $so(3)$ with $\mathbb{R}^3$ *via* the hat map $\hat{}: \mathbb{R}^3 \to so(3)$,

$$\Omega = (\Omega_1, \Omega_2, \Omega_3) \to \hat{\Omega} = \begin{bmatrix} 0 & -\Omega_3 & \Omega_2 \\ \Omega_3 & 0 & -\Omega_1 \\ -\Omega_2 & \Omega_1 & 0 \end{bmatrix},$$

we can also write

$$K_i = \frac{1}{2}\operatorname{tr}\left(\hat{\Omega}_i \mathbb{J}_i \hat{\Omega}_i^t\right) = \frac{1}{2}\Omega_i^t \mathbb{I}_i \Omega_i .$$

For further reference, recall that for any matrices $\hat{\Omega}, \hat{\Lambda} \in so(3)$ corresponding to the vectors $\boldsymbol{\Omega}, \boldsymbol{\Lambda} \in \mathbb{R}^3$, we have

$$\left[\hat{\Omega}, \hat{\Lambda}\right] = \boldsymbol{\Omega} \times \boldsymbol{\Lambda}$$

where $[\cdot,\cdot]$ denotes the matrix Lie-bracket (*i.e.* $[A,B] = AB - BA$).

In coordinates on the tangent bundle $T(SO(3)\times SO(3)\times \mathbb{R}^3 \setminus \{\text{collisions}\})$, the dynamics is given by the Lagrangian

$$L(R_1, R_2, \mathbf{r}, \dot{R}_1, \dot{R}_2, \dot{\mathbf{r}}) = \frac{1}{2}\left\langle \dot{R}_1, \dot{R}_1 \right\rangle_1 + \frac{1}{2}\left\langle \dot{R}_2, \dot{R}_2 \right\rangle_2 + \frac{1}{2}m\|\dot{\mathbf{r}}\|^2 - V(R_1, R_2, \mathbf{r}). \tag{2}$$

The spatial action of $SO(3)$ on the configuration space is the diagonal left multiplication action,

$$A\cdot(R_1, R_2, \mathbf{r}) = (AR_1, AR_2, A\mathbf{r}) , \qquad A \in SO(3). \tag{3}$$

Since L is invariant under this action, the dynamics may be retrieved from a reduced system. Indeed, describing the motion in the coordinates of one of the bodies allows us to render the equations as a reduced system on a smaller dimensional phase space

(the reduced space), together with the so-called reconstruction equation that lifts the reduced dynamics back into the unreduced phase space.

For future reference, we note that the infinitesimal action of $so(3)$ to $SO(3)\times SO(3)\times\mathbb{R}^3$ is (see Holm *et al.* (2009)):

$$\hat{\Omega}_{SO(3)\times SO(3)\times\mathbb{R}^3}\cdot(R_1,R_2,\mathbf{r})=(\hat{\Omega}R_1,\hat{\Omega}R_2,\hat{\Omega}\mathbf{r}) \tag{4}$$

Denote the relative orientation matrix of $\mathcal{B}_2$ with respect to body $\mathcal{B}_1$, and the relative position of the centre of the mass of the system, respectively, by

$$R:=R_1^{-1}R_2 \qquad \text{and} \quad \mathbf{\Gamma}:=R_1^{-1}\mathbf{r}. \tag{5}$$

We then calculate the tangent vector (velocity corresponding to the relative orientation) $\dot{R}\in T_RSO(3)$ and the advected relative velocity (*i.e.* the velocity corresponding to the relative vector) $\dot{\mathbf{\Gamma}}$

$$\dot{R}=R\hat{\Omega}_2-\hat{\Omega}_1R \qquad \text{and} \quad \dot{\mathbf{\Gamma}}=R_1^{-1}\dot{\mathbf{r}}-\hat{\Omega}_1\mathbf{\Gamma}. \tag{6}$$

Recalling that $\dot{R}_i=R_i\hat{\Omega}_i$, $i=1,2$, and using the above we calculate

$$\begin{aligned}
&L(R_1,R_2,\mathbf{r},\dot{R}_1,\dot{R}_2,\dot{\mathbf{r}})\\
&=L(R_1^{-1}R_1,R_1^{-1}R_2,R_1^{-1}\mathbf{r},R_1^{-1}\dot{R}_1,R_1^{-1}\dot{R}_2,R_1^{-1}\dot{\mathbf{r}})\\
&=L\left(R_1^{-1}R_1,R_1^{-1}R_2,R_1^{-1}(R_1\Gamma),R_1^{-1}(R_1\hat{\Omega}_1),R_1^{-1}(R_2\hat{\Omega}_2),R_1^{-1}R_1(\dot{\Gamma}+\hat{\Omega}_1\Gamma)\right)\\
&=L(\mathrm{Id}_3,R,\Gamma,\hat{\Omega}_1,R\hat{\Omega}_2,\dot{\Gamma}+\hat{\Omega}_1\Gamma)
\end{aligned}$$

from where we define the *reduced lagrangian*

$$\begin{aligned}
&l:SO(3)\times so(3)\times so(3)\times T\left(\mathbb{R}^3\setminus\{\text{collisions}\}\right)\to\mathbb{R}\\
&l(R,\hat{\Omega}_1,\hat{\Omega}_2,\Gamma,\dot{\Gamma}):=L(\mathrm{Id}_3,R,\Gamma,\hat{\Omega}_1,R\hat{\Omega}_2,\dot{\Gamma}+\hat{\Omega}_1\Gamma)
\end{aligned} \tag{7}$$

that takes the form

$$l(R,\hat{\Omega}_1,\hat{\Omega}_2,\Gamma,\dot{\Gamma})=\frac{1}{2}\left\langle\hat{\Omega}_1,\hat{\Omega}_1\right\rangle_1+\frac{1}{2}\left\langle\hat{\Omega}_2,\hat{\Omega}_2\right\rangle_2+\frac{1}{2}m\|\dot{\Gamma}+\hat{\Omega}_1\Gamma\|^2-V(R,\Gamma). \tag{8}$$

Let $\langle\cdot,\cdot\rangle_{\mathbb{R}^3}$ be the usual dot product on $\mathbb{R}^3$. Thus, for all $\mathbf{\Pi}=(\Pi_1,\Pi_2,\Pi_3)\in\mathbb{R}^3\simeq so(3)^*$ and $\mathbf{\Omega}=(\Omega_1,\Omega_2,\Omega_3)\in\mathbb{R}^3\simeq so(3)$ we have

$$\langle\mathbf{\Pi},\mathbf{\Omega}\rangle_{\mathbb{R}^3}=\mathbf{\Pi}\cdot\mathbf{\Omega}=\Pi_1\Omega_1+\Pi_2\Omega_2+\Pi_3\Omega_3.$$

We denote the pairing between $so(3)^*$ and $so(3)$ in matrix notation by $\langle\cdot,\cdot\rangle$ (no subscript!), and define the 'breve' map, $\breve{}:\mathbf{R}^3\to so(3)^*$, by $\left\langle\breve{\Pi},\hat{\Omega}\right\rangle=\langle\Pi,\Omega\rangle_{\mathbb{R}^3}$. It can be shown that

$$\left\langle\breve{\Pi},\hat{\Omega}\right\rangle=\frac{1}{2}\mathrm{tr}(\hat{\Pi}^t\hat{\Omega})=\frac{1}{2}\mathrm{tr}(\hat{\Pi}\hat{\Omega}^t)$$

for all $\hat{\Pi} \in so(3)^*$ and $\Omega \in so(3)$.

$$\left\langle \hat{M}, R\hat{\Omega} \right\rangle = \mathrm{tr}\left(\hat{M}^t(R\hat{\Omega})\right) = \tag{9}$$

$$\mathrm{tr}\left((R^t\hat{M})^t\hat{\Omega}\right) = \left\langle R^t\hat{M}, \hat{\Omega} \right\rangle = \left\langle (R^t\hat{M})_A, \hat{\Omega} \right\rangle = \left\langle \left(R^t\hat{M} - \hat{M}^t R\right), \hat{\Omega} \right\rangle \tag{10}$$

for all $\hat{\Omega} \in so(3)$, where a matrix subscript $_A$ denotes the anti-symmetric part of that matrix. (We use here the fact that the trace pairing of any symmetric matrix with an antisymmetric matrix vanishes.) Similarly,

$$\left\langle \hat{M}, \hat{\Omega}R \right\rangle = \mathrm{tr}\left(\hat{M}^t(\hat{\Omega}R)\right) = \tag{11}$$

$$\mathrm{tr}\left((\hat{M}R^t)^t\hat{\Omega}\right) = \left\langle \hat{M}R^t, \hat{\Omega} \right\rangle = \left\langle (\hat{M}R^t)_A, \hat{\Omega} \right\rangle = \left\langle \left(\hat{M}R^t - R\hat{M}^t\right), \hat{\Omega} \right\rangle. \tag{12}$$

We are ready now to state the main theorem.

Theorem 2.1 *Consider a Lagrangian* $L : T(SO(3) \times SO(3) \times D) \to \mathbb{R}$, $D \subset \mathbb{R}^3$ *open,*

$$L = L\left(R_1, R_2, \mathbf{r}, \dot{R}_1, \dot{R}_2, \dot{\mathbf{r}}\right).$$

For any given curves $(R_1(t), R_2(t)) \in SO(3) \times SO(3)$ *and* $\mathbf{r}(t) \in \mathbb{R}^3$, *let* $R(t) = R_1^{-1}(t)R_2(t)$, $\Gamma(t) = R_1(t)\mathbf{r}(t)$ *and*

$$\hat{\Omega}_i(t) := R_i(t)^{-1}\dot{R}_i(t) \in so(3).$$

Consider

$$l(R, \hat{\Omega}_1, \hat{\Omega}_2, \Gamma, \dot{\Gamma}) := L(Id_3, R, \Gamma, \hat{\Omega}_1, R\hat{\Omega}_2, \dot{\Gamma} + \hat{\Omega}_1\Gamma)$$

and let $R(t)$ *be the solution of the non-autonomous differential equation*

$$\dot{R} = R(t)\hat{\Omega}_2(t) - \hat{\Omega}_1(t)R(t), \quad R(0) = R_0. \tag{13}$$

where $R_0 = R_1(0)^{-1}R_2(0)$. *The following statements are equivalent:*

(i) $(R_1(t), R_2(t), \mathbf{r}(t))$ *satisfies the Euler-Lagrange equations for the Lagrangian* L.

(ii) The variational principle

$$\delta \int_a^b L\left(R_1(t), R_2(t), \mathbf{r}(t), \dot{R}_1(t), \dot{R}_2(t), \dot{\mathbf{r}}(t)\right) \mathrm{d}t = 0$$

holds for variations with fixed endpoints.

(iii) The ***reduced*** *variational principle*

$$\delta \int_a^b l\left(R(t), \hat{\Omega}_1(t), \hat{\Omega}_2(t), \Gamma(t), \dot{\Gamma}(t)\right) \mathrm{d}t = 0$$

holds using variations of the form

$$\delta\hat{\Omega}_i = \dot{\hat{\Sigma}}_i + [\hat{\Omega}_i, \hat{\Sigma}_i] \quad \textit{and} \quad \delta\Gamma = \Lambda - \hat{\Sigma}_1\Gamma$$

where the $\hat{\Sigma}_i(t)$ *are arbitrary paths in* $so(3)$ *which vanish at the endpoints,* i.e. $\hat{\Sigma}_i(a) = \hat{\Sigma}_i(b) = \hat{0}$, $i = 1, 2$, *and* $\Lambda(t)$ *is an arbitrary path in* $\mathbb{R}^3$ *with* $\Lambda(a) = \Lambda(b) = \mathbf{0}_{\mathbf{R}^3}$.

(iv) The (left invariant) "Euler-Poincaré" equations hold:

$$\frac{\mathrm{d}}{\mathrm{d}t}\left(\frac{\delta l}{\delta\hat{\Omega}_1}\right) = \left[\frac{\delta l}{\delta\hat{\Omega}_1}, \hat{\Omega}_1\right] + \left(R\left(\frac{\delta l}{\delta R}\right)^t - \frac{\delta l}{\delta R}R^t\right), \tag{14}$$

$$\frac{\mathrm{d}}{\mathrm{d}t}\left(\frac{\delta l}{\delta\hat{\Omega}_2}\right) = \left[\frac{\delta l}{\delta\hat{\Omega}_2}, \hat{\Omega}_2\right] + \left(R^t\frac{\delta l}{\delta R} - \left(\frac{\delta l}{\delta R}\right)^t R\right), \tag{15}$$

$$\frac{\mathrm{d}}{\mathrm{d}t}\left(\frac{\delta l}{\delta\dot{\Gamma}}\right) = \frac{\delta l}{\delta\Gamma}. \tag{16}$$

Proof. The equivalence of (i) and (ii) is a restatement of Hamilton's principle. To show that (ii) and (iii) are equivalent, we compute the variations $\delta\hat{\Omega}_1, \delta\hat{\Omega}_2$, and $\delta\Gamma$ and induced by the variations $\delta R_1, \delta R_2$, and $\delta\mathbf{r}$.

Given that $\hat{\Omega}_i = R_i^{-1}\dot{R}_i$ and denoting $\hat{\Sigma}_i := R_i^{-1}\delta R_i \in so(3)$, $i = 1, 2$ we calculate:

$$\begin{aligned}
\delta\hat{\Omega}_i &= (\delta R_i^{-1})\dot{R}_i + R_i^{-1}\delta\dot{R}_i = -(R_i^{-1}\delta R_i R_i^{-1})\dot{R}_i + R_i^{-1}\delta\dot{R}_i \\
&= -(R_i^{-1}\delta R_i)(R_i^{-1}\dot{R}_i) + R_i^{-1}\left(\delta\frac{\mathrm{d}R_i}{\mathrm{d}t}\right) = -\hat{\Sigma}\hat{\Omega}_i + R_i^{-1}\frac{\mathrm{d}}{\mathrm{d}t}(\delta R_i) \\
&= -\hat{\Sigma}_i\hat{\Omega}_i + \frac{\mathrm{d}}{\mathrm{d}t}\left(R_i^{-1}\delta R_i\right) - \dot{R}_i{}^{-1}\delta R_i = -\hat{\Sigma}_i\hat{\Omega}_i + \frac{d\hat{\Sigma}_i}{dt} + (R_i^{-1}\dot{R}_i R_i^{-1})\delta R_i \\
&= -\hat{\Sigma}_i\hat{\Omega}_i + \frac{\mathrm{d}\hat{\Sigma}_i}{\mathrm{d}t} + (R_i^{-1}\dot{R}_i)(R_i^{-1})\delta R_i = \frac{\mathrm{d}\hat{\Sigma}_i}{\mathrm{d}t} - \hat{\Sigma}_i\hat{\Omega}_i + \hat{\Omega}_i\hat{\Sigma}_i \\
&= \frac{\mathrm{d}\hat{\Sigma}_i}{\mathrm{d}t} + [\hat{\Sigma}_i, \hat{\Omega}_i].
\end{aligned}$$

Thus we have

$$\delta\hat{\Omega}_i = \frac{\mathrm{d}\hat{\Sigma}_i}{\mathrm{d}t} + [\hat{\Sigma}_i, \hat{\Omega}_i], \quad i = 1, 2.$$

The variation of Γ is

$$\delta\Gamma = \delta(R_1^{-1}\mathbf{r}) = \delta(R_1^{-1})\mathbf{r} + R_1^{-1}\delta\mathbf{r} = -R_1^{-1}(\delta R_1)R_1^{-1}\mathbf{r} + R_1^{-1}\delta\mathbf{r} \tag{17}$$

Denoting $\Lambda := R_1^{-1}\delta\mathbf{r}$, the above reads:

$$\delta\Gamma = \Lambda - \hat{\Sigma}_1\Gamma. \tag{18}$$

To complete the proof we show the equivalence of (iii) and (iv). First note that since

$$\delta R = \delta(R_1^{-1}R_2) = \delta(R_1^{-1})R_2 + R_1^{-1}\delta r_2 = -(R_1^{-1}(\delta R_1)R_1^{-1})R_2 + R_1^{-1}R_2R_2^{-1}\delta R_2$$
$$= -(R_1^{-1}\delta R_1)(R_1^{-1}R_2) + (R_1^{-1}R_2)(R_2^{-1}\delta R_2) = -\hat{\Sigma}_1 R + R\hat{\Sigma}_2$$

we have

$$\delta R = R\hat{\Sigma}_2 - \hat{\Sigma}_1 R.$$

Now we calculate

$$\delta\int_a^b l\left(R,\Gamma,\hat{\Omega}_1,\hat{\Omega}_2,\dot{\Gamma}\right)\mathrm{d}t$$
$$= \int_a^b \left\langle \frac{\delta l}{\delta R}, \delta R\right\rangle + \left\langle \frac{\delta l}{\delta\Gamma}, \delta\Gamma\right\rangle_{\mathbb{R}^3} + \sum_{i=1}^{2}\left\langle \frac{\delta l}{\delta\hat{\Omega}_i}, \delta\hat{\Omega}_i\right\rangle + \left\langle \frac{\delta l}{\delta\dot{\Gamma}}, \delta\dot{\Gamma}\right\rangle_{\mathbb{R}^3}\mathrm{d}t$$
$$= \int_a^b \left\langle \frac{\delta l}{\delta R}, R\hat{\Sigma}_2 - \hat{\Sigma}_1 R\right\rangle dt + \left\langle \frac{\delta l}{\delta\Gamma}, \delta\Gamma\right\rangle_{\mathbb{R}^3} +$$
$$\sum_{i=1}^{2}\int_a^b \left\langle \frac{\delta l}{\delta\hat{\Omega}_i}, \dot{\hat{\Sigma}}_i + [\hat{\Sigma}_i, \hat{\Omega}_i]\right\rangle \mathrm{d}t + \left\langle \frac{\delta l}{\delta\dot{\Gamma}}, \delta\dot{\Gamma}\right\rangle_{\mathbb{R}^3} dt \tag{19}$$

Using the relations (10) and (12), the first term of (19) becomes

$$\int_a^b \left\langle \frac{\delta l}{\delta R}, R\hat{\Sigma}_2 - \hat{\Sigma}_1 R\right\rangle \mathrm{d}t = \int_a^b \left\langle \frac{\delta l}{\delta R}, R\hat{\Sigma}_2\right\rangle dt - \int_a^b \left\langle \frac{\delta l}{\delta R}, \hat{\Sigma}_1 R\right\rangle \mathrm{d}t$$
$$= \int_a^b \left\langle \left(R^t\frac{\delta l}{\delta R} - \left(\frac{\delta l}{\delta R}\right)^t R\right), \hat{\Sigma}_2\right\rangle \mathrm{d}t$$
$$- \int_a^b \left\langle \left(\frac{\delta l}{\delta R}R^t - R\left(\frac{\delta l}{\delta R}\right)^t\right), \hat{\Sigma}_1\right\rangle \mathrm{d}t$$

Using that
$\hat{\Pi} \in so^*(3)$ we have $\left\langle \hat{\Pi}, [\hat{\Sigma}, \hat{\Omega}]\right\rangle = \left\langle [\hat{\Omega}, \hat{\Pi}], \hat{\Sigma}\right\rangle$ for all $\hat{\Sigma}, \hat{\Omega} \in so(3)$,
that $\delta(\mathrm{d}/\mathrm{d}t) = (\mathrm{d}/\mathrm{d}t)\delta$, integrating by parts and taking into account the boundary conditions, the third term of (19) becomes:

$$\int_a^b \left\langle -\frac{\mathrm{d}}{\mathrm{d}t}\left(\frac{\delta l}{\delta \hat{\Omega}_1}\right) + \left[\frac{\delta l}{\delta \hat{\Omega}_1}, \hat{\Omega}_1\right], \hat{\Sigma}_1 \right\rangle \mathrm{d}t$$
$$+ \int_a^b \left\langle -\frac{d}{dt}\left(\frac{\delta l}{\delta \hat{\Omega}_2}\right) + \left[\frac{\delta l}{\delta \hat{\Omega}_2}, \hat{\Omega}_2\right], \hat{\Sigma}_2 \right\rangle \mathrm{d}t$$

Finally, define $\Gamma \diamond \mathbf{P} \in so^*(3)$ *via* $\left\langle \Gamma \diamond \mathbf{P}, \hat{\Sigma} \right\rangle := \left\langle \mathbf{P}, \hat{\Sigma}\Gamma \right\rangle = \langle \mathbf{P}, \Sigma \times \Gamma \rangle_{\mathbb{R}^3} = \langle \Gamma \times \mathbf{P}, \Sigma \rangle_{\mathbb{R}^3}$ for all $\mathbf{P}, \Gamma \in \mathbb{R}^3$, and $\hat{\Sigma} \in so(3)$. Substituting (18) the second and the last terms of (19) transform to

$$\int_a^b \left\langle \frac{\delta l}{\delta \Gamma}, \delta\Gamma \right\rangle_{\mathbb{R}^3} + \left\langle \frac{\delta l}{\delta \dot{\Gamma}}, \frac{\mathrm{d}}{\mathrm{d}t}\delta\Gamma \right\rangle_{\mathbb{R}^3}$$
$$= \int_a^b \left\langle -\frac{\mathrm{d}}{\mathrm{d}t}\left(\frac{\delta l}{\delta \dot{\Gamma}}\right) + \frac{\delta l}{\delta \Gamma}, \Lambda - \hat{\Sigma}_1\Gamma \right\rangle_{\mathbb{R}^3}$$
$$= \int_a^b \left\langle -\frac{\mathrm{d}}{\mathrm{d}t}\left(\frac{\delta l}{\delta \dot{\Gamma}}\right) + \frac{\delta l}{\delta \Gamma}, \Lambda \right\rangle_{\mathbb{R}^3} - \int_a^b \left\langle \Gamma \diamond \left[-\frac{\mathrm{d}}{\mathrm{d}t}\left(\frac{\delta l}{\delta \dot{\Gamma}}\right) + \frac{\delta l}{\delta \Gamma} \right], \hat{\Sigma}_1 \right\rangle.$$

Thus we obtain

$$\delta \int_a^b l\left(R, \Gamma, \hat{\Omega}_1, \hat{\Omega}_2, \dot{\Gamma}\right) \mathrm{d}t$$
$$= \int_a^b \left\langle -\frac{\mathrm{d}}{\mathrm{d}t}\left(\frac{\delta l}{\delta \hat{\Omega}_1}\right) + \left[\frac{\delta l}{\delta \hat{\Omega}_1}, \hat{\Omega}_1\right] - \left(\frac{\delta l}{\delta R}R^t - R\left(\frac{\delta l}{\delta R}\right)^t\right) - \Gamma \diamond \left[-\frac{d}{dt}\left(\frac{\delta l}{\delta \dot{\Gamma}}\right) + \frac{\delta l}{\delta \Gamma} \right], \hat{\Sigma}_1 \right\rangle \mathrm{d}t$$
$$+ \int_a^b \left\langle -\frac{\mathrm{d}}{\mathrm{d}t}\left(\frac{\delta l}{\delta \hat{\Omega}_2}\right) + \left[\frac{\delta l}{\delta \hat{\Omega}_2}, \hat{\Omega}_2\right] + \left(R^t\frac{\delta l}{\delta R} - \left(\frac{\delta l}{\delta R}\right)^t R\right), \hat{\Sigma}_2 \right\rangle \mathrm{d}t$$
$$+ \int_a^b \left\langle -\frac{d}{dt}\left\langle \frac{\delta l}{\delta \dot{\Gamma}}\right) + \frac{\delta l}{\delta \Gamma}, \Lambda \right\rangle_{\mathbb{R}^3} \mathrm{d}t.$$

Since $\hat{\Sigma}_1, \hat{\Sigma}_2$ and Λ are arbitrary, the conclusion follows.

■

Recall that any orthogonal matrix R can be expressed as $R := [\alpha_1, \alpha_2, \alpha_3]$ with $\alpha_i \in \mathbf{R}^3$, $i = 1,2,3$, such that $\alpha_i^2 = 1$ and $\alpha_i \cdot \alpha_j = 0$ for $i \neq j$. Then for any function depending on $R \in SO(3)$, *i.e.*, $f = f(R, \cdot) \to \mathbb{R}$ the vector representation of

$$\hat{T}_1 := R\left(\frac{\delta f}{\delta R}\right)^t - \frac{\delta f}{\delta R}R^t \quad \text{and} \quad \hat{T}_2 := R^t\frac{\delta f}{\delta R} - \left(\frac{\delta f}{\delta R}\right)^t R$$

is

$$T_1 = \sum_{i=1,2,3} \alpha_i \times \frac{\delta f}{\delta \alpha_i} \quad \text{and} \quad T_2 = -\sum_{i=1.2.3} \alpha_i \times \frac{\delta f}{\delta \alpha_i},$$

respectively. Note that in the above, we calculate $\frac{\delta f}{\delta R}$ as the matrix

$$\frac{\delta f}{\delta R} = \left[\frac{\partial f}{\partial \alpha_1} \; \frac{\partial f}{\partial \alpha_2} \; \frac{\partial f}{\partial \alpha_3}\right]$$

where for the vector $\alpha_i = (\alpha_{i1}, \alpha_{i2}, \alpha_{i3})^t$ we have $\frac{\partial f}{\partial \alpha_i} = \left(\frac{\partial f}{\alpha_{i2}}, \frac{\partial f}{\alpha_{i1}}, \frac{\partial f}{\alpha_{i3}}\right)^t$.

This allows to writing the vector form of the reduced equations of motion (16):

$$\frac{\mathrm{d}}{\mathrm{d}t}\left(\frac{\delta l}{\delta \Omega_1}\right) = \frac{\delta l}{\delta \Omega_1} \times \Omega_1 + \sum_{i=1,2,3} \alpha_i \times \frac{\delta l}{\delta \alpha_i} \tag{20}$$

$$\frac{\mathrm{d}}{\mathrm{d}t}\left(\frac{\delta l}{\delta \Omega_2}\right) = \frac{\delta l}{\delta \Omega_2} \times \Omega_2 - \sum_{i=1,2,3} \alpha_i \times \frac{\delta l}{\delta \alpha_i} \tag{21}$$

$$\frac{\mathrm{d}}{\mathrm{d}t}\left(\frac{\delta l}{\delta \dot{\Gamma}}\right) = \frac{\delta l}{\delta \Gamma}. \tag{22}$$

This above system is completed by the relative orientation equation (13).

Specializing the Lagrangian to the full two body problem, the reduced lagrangian is given by (8). In vectorial notation the reduced lagrangian is

$$l(R, \Omega_1, \Omega_2, \Gamma, \dot{\Gamma}) := \frac{1}{2}\langle \Omega_1, \mathbb{I}_1 \Omega_1 \rangle_{\mathbf{R}^3} + \frac{1}{2}\langle \Omega_2, \mathbb{I}_2 \Omega_2 \rangle_{\mathbf{R}^3} + \frac{m}{2}\|\dot{\Gamma} + \Omega_1 \times \Gamma\|^2 - V(R, \Gamma) \tag{23}$$

and the equations of motion are

$$\begin{aligned}
&\frac{\mathrm{d}}{\mathrm{d}t}\left(\mathbb{I}_1 \Omega_1 + m\Gamma \times (\dot{\Gamma} + \Omega_1 \times \Gamma)\right) \\
&= \mathbb{I}_1 \Omega_1 \times \Omega_1 - m\left[(\dot{\Gamma} + \Omega_1 \times \Gamma) \times \Gamma\right] \times \Omega_1 + \sum_{i=1,2,3} \alpha_i \times \frac{\delta V}{\delta \alpha_i} \mathbb{I}_2 \dot{\Omega}_2 \\
&= \mathbb{I}_2 \Omega_2 \times \Omega_2 - \sum_{i=1,2,3} \alpha_i \times \frac{\delta V}{\delta \alpha_i} \\
&\frac{\mathrm{d}}{\mathrm{d}t}\left(\dot{\Gamma} + \Omega_1 \times \Gamma\right) = \left(\dot{\Gamma} \quad + \Omega_1 \times \Gamma\right) \times \Omega_1 - \frac{1}{m}\frac{\delta V}{\delta \Gamma}
\end{aligned} \tag{24}$$

3. HAMILTONIAN FORMULATION

The Hamiltonian of the full two body problem may be obtained by applying the Legendre transform to the Lagrangian (2) and it reads:

$$H : T^*SO(3) \times T^*SO(3) \times T^*\mathbf{R}^3 \setminus \{\text{collisions}\} \to \mathbf{R}$$

$$H(R_1, \pi_{R_1}, R_2, \pi_{R_2}, \mathbf{r}, \mathbf{p}) = \frac{1}{2}\langle \pi_{R_1}, \pi_{R_1} \rangle_1^* + \frac{1}{2}\langle \pi_{R_2}, \pi_{R_2} \rangle_2^* + \frac{1}{2m}\mathbf{p}^2 + V(R, \mathbf{r}), \tag{25}$$

where the pairings $\langle\cdot,\cdot\rangle_i^*$ on $T^*_{R_i}(SO(3)$ for fixed R_i, i=1,2 correspond to the kinetic terms in (2), and, as usual:

$$\pi_{R_i} = \frac{\partial L}{\partial \dot{R}_i} \in T^*_{R_i} SO(3),\ i = 1,2 \quad \text{and} \quad \mathbf{p} = \frac{\partial L}{\partial \dot{\mathbf{r}}} \in T^*_{\mathbf{r}}\mathbb{R}^3 \simeq \mathbb{R}^3. \tag{26}$$

In order to obtain the reduced Hamiltonian we use the reduced Legendre transform. First we calculate the momenta

$$\mathbf{\Pi}_1 = \frac{\mathrm{d}}{\mathrm{d}t}\left(\frac{\delta l}{\delta \mathbf{\Omega}_1}\right) = \mathbb{I}_1\mathbf{\Omega}_1 + m\mathbf{\Gamma}\times\left(\dot{\mathbf{\Gamma}} + \mathbf{\Omega}_1\times\mathbf{\Gamma}\right) \tag{27}$$

$$\mathbf{\Pi}_2 = \frac{\mathrm{d}}{\mathrm{d}t}\left(\frac{\delta l}{\delta \mathbf{\Omega}_2}\right) = \mathbb{I}_2\mathbf{\Omega}_2 \tag{28}$$

$$\mathbf{P} = \frac{\mathrm{d}}{\mathrm{d}t}\left(\frac{\delta l}{\delta \dot{\mathbf{\Gamma}}}\right) = m\left(\dot{\mathbf{\Gamma}} + \mathbf{\Omega}_1\times\mathbf{\Gamma}\right). \tag{29}$$

Next we calculate the reduced Hamiltonian *via*

$$\begin{aligned} &H(R,\mathbf{\Pi}_1,\mathbf{\Pi}_2,\mathbf{\Gamma},\mathbf{P}) \\ &\quad = \langle\mathbf{\Pi}_1,\mathbf{\Omega}_1(\mathbf{\Pi}_1,\mathbf{\Pi}_1,\mathbf{\Gamma},\mathbf{P})\rangle_{\mathbb{R}^3} + \langle\mathbf{\Pi}_2,\mathbf{\Omega}_2(\mathbf{\Pi}_1,\mathbf{\Pi}_1,\mathbf{\Gamma},\mathbf{P})\rangle_{\mathbb{R}^3} \\ &\quad + \left\langle\mathbf{P},\dot{\mathbf{\Gamma}}(\mathbf{\Pi}_1,\mathbf{\Pi}_1,\mathbf{\Gamma},\mathbf{P})\right\rangle_{\mathbb{R}^3} \\ &\quad - l\left(\mathbf{\Omega}_1(R,\mathbf{\Pi}_1,\mathbf{\Pi}_1,\mathbf{\Gamma},\mathbf{P}),\mathbf{\Omega}_2(\mathbf{\Pi}_1,\mathbf{\Pi}_1,\mathbf{\Gamma},\mathbf{P}),\mathbf{\Gamma},\dot{\mathbf{\Gamma}}(\mathbf{\Pi}_1,\mathbf{\Pi}_1,\mathbf{\Gamma},\mathbf{P})\right) \end{aligned} \tag{30}$$

and obtain the reduced Hamiltonian of the full two body problem

$$H : SO(3)\times so^*(3)\times so^*(3)\times T^*\mathbb{R}^3 \to \mathbb{R}, \tag{31}$$

$$\begin{aligned} &H(R,\mathbf{\Pi}_1,\mathbf{\Pi}_2,\mathbf{\Gamma},\mathbf{P}) \\ &= \frac{1}{2}\left\langle\mathbf{\Pi}_1+\mathbf{\Gamma}\times\mathbf{P},\mathbb{I}_1^{-1}(\mathbf{\Pi}_1+\mathbf{\Gamma}\times\mathbf{P})\right\rangle_{\mathbb{R}^3} + \frac{1}{2}\left\langle\mathbf{\Pi}_2,\mathbb{I}_2^{-1}\mathbf{\Pi}_2\right\rangle_{\mathbb{R}^3} \\ &+ \frac{1}{2}m\left\langle\mathbf{P},\mathbf{P}\right\rangle_{\mathbb{R}^3} + V(R,\mathbf{\Gamma}). \end{aligned} \tag{32}$$

The dynamics is given by the Poisson bracket

$$\begin{aligned} &\{F,H\}(R,\mathbf{\Pi}_1,\mathbf{\Pi}_2,\mathbf{\Gamma},\mathbf{P}) \\ &= -\left\langle\mathbf{\Pi}_1,\frac{\delta F}{\delta\mathbf{\Pi}_1}\times\frac{\delta H}{\delta\mathbf{\Pi}_1}\right\rangle_{\mathbb{R}^3} - \left\langle\mathbf{\Pi}_2,\frac{\delta F}{\delta\mathbf{\Pi}_2}\times\frac{\delta H}{\delta\mathbf{\Pi}_2}\right\rangle_{\mathbb{R}^3} \\ &+ \left(\frac{\delta F}{\delta\mathbf{\Gamma}}\frac{\delta H}{\delta\mathbf{P}} - \frac{\delta H}{\delta\mathbf{\Gamma}}\frac{\delta F}{\delta\mathbf{P}}\right) - \left\langle\frac{\delta F}{\delta R},\frac{\delta H}{\delta\mathbf{\Pi}_1}R - R\frac{\delta H}{\delta\mathbf{\Pi}_2}\right\rangle \\ &+ \left\langle\frac{\delta H}{\delta R},\frac{\delta F}{\delta\mathbf{\Pi}_1}R - R\frac{\delta F}{\delta\mathbf{\Pi}_2}\right\rangle. \end{aligned} \tag{33}$$

This is deduced by considering the composition of real valued (smooth) functions $F : SO(3) \times so^*(3) \times so^*(3) \times T^*\mathbb{R}^3 \to \mathbb{R}$ with the Poisson map

$$\lambda : T^*SO(3) \times T^*SO^*(3) \times T^*\mathbb{R}^3 \to SO(3) \times so^*(3) \times so^*(3) \times T^*\mathbb{R}^3$$
$$\lambda(R_1, \pi_{R_1}, R_2, \pi_{R_1}, \mathbf{r}, \mathbf{p}) = \left(R_1^{-1}R_2,\, R_1^t\pi_{R_1},\, R_2^t\pi_{R_2}, \mathbf{r}, \mathbf{p}\right); \tag{34}$$

using the chain rule, the canonical bracket on $T^*SO(3) \times T^*SO^*(3) \times T^*\mathbb{R}^3$ becomes the Poisson bracket (33) (for details on this kind of techniques, see Krishnaprasad and Marsden (1987)).

The equations of the reduced dynamics are:

$$\dot{\mathbf{\Pi}}_1 = \mathbf{\Pi}_1 \times \left[\mathbb{I}_1^{-1}(\mathbf{\Pi}_1 + \mathbf{\Gamma} \times \mathbf{P})\right] + \sum_{i=1,2,3} \boldsymbol{\alpha}_i \times \frac{\delta V}{\delta \boldsymbol{\alpha}_i} \tag{35}$$

$$\dot{\mathbf{\Pi}}_2 = \mathbf{\Pi}_2 \times \mathbb{I}_2^{-1}\mathbf{\Pi}_2 - \boldsymbol{\alpha}_i \times \frac{\delta V}{\delta \boldsymbol{\alpha}_i} \tag{36}$$

$$\dot{\mathbf{\Gamma}} = \frac{1}{m}\mathbf{P} + \mathbf{\Gamma} \times \left[\mathbb{I}_1^{-1}(\mathbf{\Pi}_1 + \mathbf{\Gamma} \times \mathbf{P})\right] \tag{37}$$

$$\dot{\mathbf{P}} = \mathbf{P} \times \left[\mathbb{I}_1^{-1}(\mathbf{\Pi}_1 + \mathbf{\Gamma} \times \mathbf{P})\right] - \frac{\partial V}{\partial \mathbf{\Gamma}} \tag{38}$$

together with the reconstruction (orientation) equation:

$$\dot{R} = R\hat{\Omega}_2 - \hat{\Omega}_1 R. \tag{39}$$

where $R = [\boldsymbol{\alpha}_1, \boldsymbol{\alpha}_2, \boldsymbol{\alpha}_3]$ and $\hat{\Omega}_1$ and $\hat{\Omega}_2$ are calculated via the inverse of (27)- (29).

Remark 3.1 *Note that with the choice of $\mathcal{B}_1$ as reference frame, $\mathbf{\Pi}_1$ is the sum of the angular momentum $\mathbb{I}_1\mathbf{\Omega}_1$ of the rigid body $\mathcal{B}_1$ and the angular momentum $\mathbf{\Gamma} \times \mathbf{P}$ of the relative vector, both in the body coordinates of $\mathcal{B}_1$:*

$$\mathbf{\Pi}_1 = \mathbb{I}_1\mathbf{\Omega}_1 + \mathbf{\Gamma} \times \mathbf{P}. \tag{40}$$

Remark 3.2 *The change of variable*

$$(\mathbf{\Pi}_1, \mathbf{\Pi}_2, \mathbf{P}) = (\mathbf{\Lambda}_1, \mathbf{\Lambda}_2, \mathbf{P}) := (\mathbf{\Pi}_1 - \mathbf{\Gamma} \times \mathbf{P}, \mathbf{\Pi}_2, \mathbf{P}),$$

is a Poisson map (see Marsden (1992), Section 3.7) and it leads to the Hamiltonian of the two full body problem as used by Maciejewski (1995) and Cendra and Marsden (2004):

$$H(R, \mathbf{\Lambda}_1, \mathbf{\Lambda}_2, \mathbf{\Gamma}, \mathbf{P}) = \frac{1}{2}\left\langle \mathbf{\Lambda}_1, \mathbb{I}_1^{-1}\mathbf{\Lambda}_1 \right\rangle_{\mathbb{R}^3} + \frac{1}{2}\left\langle \mathbf{\Lambda}_2, \mathbb{I}_2^{-1}\mathbf{\Lambda}_2 \right\rangle_{\mathbb{R}^3} + \frac{1}{2m}\mathbf{P}^2 + V(R, \mathbf{\Gamma}). \tag{41}$$

The equations of motion are

$$\dot{\mathbf{\Lambda}}_1 = \mathbf{\Lambda}_1 \times \mathbb{I}_1^{-1}\mathbf{\Lambda}_1 + \sum_{i=1,2,3} \boldsymbol{\alpha}_i \times \frac{\delta V}{\delta \boldsymbol{\alpha}_i} + \mathbf{\Gamma} \times \frac{\partial V}{\partial \mathbf{\Gamma}} \tag{42}$$

$$\dot{\mathbf{\Lambda}}_2 = \mathbb{I}_2^{-1}\mathbf{\Lambda}_2 - \sum_{i=1,2,3} \boldsymbol{\alpha}_i \times \frac{\delta V}{\delta \boldsymbol{\alpha}_i} \tag{43}$$

$$\dot{\mathbf{\Gamma}} = \frac{1}{m}\mathbf{P} + \mathbf{\Gamma} \times \mathbb{I}^{-1}\mathbf{\Lambda}_1 \tag{44}$$

$$\dot{\mathbf{P}} = \mathbf{P} \times \mathbf{\Gamma}_1 - \frac{\partial V}{\partial \mathbf{\Gamma}}. \tag{45}$$

Note that this equations coincide to those in Maciejewski (1995).

Let us denote by $\mathbf{\Lambda}_1$ and $\mathbf{\Lambda}_2$ the body angular momenta of $\mathcal{B}_1$ and $\mathcal{B}_2$, respectively (*i.e.*, $\mathbf{\Lambda}_1 = \mathbb{I}_1\mathbf{\Omega}_1$ and $\mathbf{\Lambda}_2 = \mathbb{I}_2\mathbf{\Omega}_2$). The *spatial (inertial) total angular momentum* is

$$J = \boldsymbol{\pi}_1 + \boldsymbol{\pi}_2 + \mathbf{r} \times \mathbf{p} \tag{46}$$

where $\boldsymbol{\pi}_i = R_i\mathbf{\Lambda}_i$. Since the Hamiltonian (25) is invariant under spatial rotations, Noether's theorem implies that the spatial angular momentum is conserved along any trajectory; see Holm *et al.* (2009). We have

$$\begin{aligned} \|\boldsymbol{\pi}_1 + \boldsymbol{\pi}_2 + \mathbf{r} \times \mathbf{p}\| &= \|R_1\mathbf{\Lambda}_1 + R_2\mathbf{\Lambda}_2 + (R_1\mathbf{\Gamma}) \times (R_1\mathbf{P}))\ \| \\ &= \|\mathbf{\Lambda}_1 + R_1^{-1}R_2\mathbf{\Lambda}_2 + R_1^{-1}\left(R_1(\mathbf{\Gamma} \times \mathbf{P})\right)\ \| \\ &= \|\mathbf{\Lambda}_1 + R\mathbf{\Lambda}_2 + \mathbf{\Gamma} \times \mathbf{P}\| = \|\mathbf{\Pi}_1 + R\mathbf{\Pi}_2\|. \end{aligned} \tag{47}$$

Any scalar function $\Phi(\|\mathbf{\Pi}_1 + R\mathbf{\Pi}_2\|^2)$ is a conserved quantity, *i.e.* a Casimir for the reduced dynamics.

Acknowledgements. The authors were supported by two Discovery grants awarded by the National Science and Engineering Council of Canada (NSERC).

REFERENCES

Bellerose J.E., Scheeres D.J.: 2008, *Celest. Mech. Dyn. Astron.* **100**, 63.

Cendra, H. and Marsden, J.E.: 2004, *Dynamical Systems. An International Journal* **20**, 3.

Doubochine, G. N.: 1984, *Celestial Mech.* **33**, no. 1, 31.

Hernández-Garduno, A. and Stoica, C.: 2015, *SIAM Journal on Applied Dynamical Systems* **14**, 1. 221.

Xiyun Hou X. and Xin X.: 2018, *Astrodynamics* **2**, Issue 1, 39.

Iacob, C.: 1980, *Theoretical mechanics*, Editura Didacticua csi Pedagogicua, Bucurecsti.

Jose, J.V. and Saletan, E.J.: 1998, *Classical Dynamics: a contemporary approach*, Cambridge University Press.

Kondurar V.T.: 1974, *On Lagrange solutions in the problem of three rigid bodies* **10**, Issue 3, 327.
Krishnaprasad, P. and Marsden, J.E.: 1987, *Arch. Rat. Mech. Anal.* **98**, no.1, 71.
Koon, W.-S., Marsden, J. E., Ross S. ,Lo M., , and D. J. Scheeres, D. J.: 2004, *NY Acad of Sciences* **1017**, 11.
Maciejewski, A.J.: 1995, *Celestial Mech. Dynam. Astronom.* **63**, 1.
Marsden, J.E.: 1992, *Lectures on Mechanics*, Vol. **174** London Mathematical Society Lecture Notes, Cambridge University Press.
Marsden, J.E. and Ratiu T.S.: 1999 , *Introduction to Mechanics and Symmetry, Texts in Applied Mathematics* **17**, Springer-Verlag, Second edition.
Moeckel, R.: 2017 , *Celestial Mech. Dynam. Astronom.* **128**, 3.
Moeckel, R.: 2018, *Celestial Mech. Dynam. Astronom.* **130**, 17.
Holm D.D., Schmah T. and Stoica C.: 2009, *Geometric mechanics and symmetry. From finite to Infinite Dimensions*, Oxford Texts in Applied and Engineering Mathematics **12**, Oxford University Press.
Scheeres, D.J.: 2006, *Celes. Mech. Dyn. Astron.* **94**, 317.
Scheeres, D.J.: 2009, *Celes. Mech. Dyn. Astron.* **104**, 103.
Scheeres, D.J.: 2017, *Celes. Mech. Dyn. Astron.* **128**, Issue 2-3, pp 131.
Vera, J.A. and Vigueras A.: 2006, *Celes. Mech. Dyn. Astron.* **94**, Issue 3, pp 289.
Zhuravlev, S.G., Petrutskii, A.A.: 1990, *Soviet Astron.* **34**, 299304.

APPENDIX

We append this note with some formulas on the interacting potential. In concordance with most physical situations, we may assume that the distance between the bodies is much larger than the bodies dimensions. Thus we consider the potential truncated to the third order (Maciejewski (1995)):

$$V(R,\Gamma) = -\frac{Gm_1m_2}{|\Gamma|} - \frac{G}{2|\Gamma|^3}\left(m_1 \mathrm{Tr}\mathbb{I}_1 + m_1 \mathrm{Tr}\mathbb{I}_2\right)$$
$$+ \frac{3G}{2|\Gamma|^5}\left(m_1 \langle \Gamma, \mathbb{I}_1\Gamma\rangle_{\mathbf{R}^3} + m_2 \langle R\Gamma, \mathbb{I}_2 R\Gamma\rangle_{\mathbf{R}^3}\right) \tag{48}$$

where the rotation matrix $R \in SO(3)$ is represented by $R = [\boldsymbol{\alpha}_1, \boldsymbol{\alpha}_2, \boldsymbol{\alpha}_3]$ with $\boldsymbol{\alpha}_i$ (column) vectors such that $\boldsymbol{\alpha}_i^2 = 1$ and $\boldsymbol{\alpha}_i \cdot \boldsymbol{\alpha}_j = 0$ for $i \neq j$. Next we calculate the terms $\boldsymbol{\alpha}_i \times \partial V/\partial \boldsymbol{\alpha}_i$ and $\boldsymbol{\Lambda} \times \partial V/\partial \boldsymbol{\Lambda}$ occurring in the equations of motion. Denoting $\mathbb{I}_2 := \mathrm{diag}(I_{21}, I_{22}, I_{23})$, we obtain:

$$\boldsymbol{\alpha}_1 \times \frac{\partial V}{\partial \boldsymbol{\alpha}_1} = 2\Gamma_1^2 \begin{pmatrix} \alpha_2\alpha_3(I_{23} - I_{22}) \\ -\alpha_3\alpha_1(I_{23} - I_{21}) \\ \alpha_1\alpha_2(I_{21} - I_{21}) \end{pmatrix} + 2\Gamma_1\left(\boldsymbol{\alpha}_1 \times \mathbb{I}_2\boldsymbol{\alpha}_2 + \boldsymbol{\alpha}_1 \times \mathbb{I}_2\boldsymbol{\alpha}_3\right) \tag{49}$$

and circular combinations. Further

$$\frac{\partial V}{\partial \mathbf{\Lambda}} = \left[\frac{G m_1 m_2}{|\mathbf{\Gamma}|^2} - \frac{3G}{2|\mathbf{\Gamma}|^4} \left(m_1 \mathrm{Tr}\, \mathbb{I}_1 + m_1 \mathrm{Tr}\, \mathbb{I}_2 \right) - \right.$$
$$\left. \frac{15G}{2|\mathbf{\Gamma}|^6} \left(m_1 \left\langle \mathbf{\Gamma}, \mathbb{I}_1 \mathbf{\Gamma} \right\rangle_{\mathbf{R}^3} + m_2 \left\langle R\mathbf{\Gamma}, \mathbb{I}_2 R\mathbf{\Gamma} \right\rangle_{\mathbf{R}^3} \right) \right] \frac{\mathbf{\Lambda}}{|\mathbf{\Lambda}|}$$
$$+ \frac{3G}{|\mathbf{\Gamma}|^4} \left(m_1 \mathbb{I}_1 + m_2 R^t \mathbb{I}_2 R \right) \frac{\mathbf{\Lambda}}{|\mathbf{\Lambda}|} \tag{50}$$

and so

$$\mathbf{\Lambda} \times \frac{\partial V}{\partial \mathbf{\Lambda}} = \frac{3G}{|\mathbf{\Gamma}|^5} \left[m_1 \mathbf{\Lambda} \times \mathbb{I}_1 \mathbf{\Lambda} + m_2 \mathbf{\Lambda} \times \left(R^t \mathbb{I}_2 R \mathbf{\Lambda} \right) \right] . \tag{51}$$

Received on 20 November 2018

ASTEROID PARENT BODIES OF METEOR SHOWERS

BOGDAN ALEXANDRU DUMITRU[1,2,3], MIREL BIRLAN[2,3], DAN ALIN NEDELCU[4,2]

[1] *Institute of Space Science*
Str. Atomistilor 409, 077125 Magurele, Romania
Email: bogdan.dumitru@spacescience.ro
[2] *IMCCE, Paris Observatory,*
77 avenue Denfert-Rochereau, 75014 Paris Cedex, France
[3] *Faculty of Physics, Bucharest University,*
405, Atomistilor Street, 077125 Magurele, Ilfov, Romania
[4] *Astronomical Institute of Romanian Academy,*
5, Cutitul de Argint Street , 040557 Bucharest, Romania

Abstract. In the previous study, we associated 223 asteroids to 28 meteor showers by using three D-Criteria metrics, our own empirical method of threshold selection and D-parameter uncertainty. The databases used in the simulation were the MPCORB (for asteroids) and IAU Meteor Data Center (for meteor showers) from February 2017.

In the present work, we will present an update of our previous study on the new databases (the MPCORB and meteor shower databases form February 2018). In the new simulation, we found 72 additional asteroids that can be associated to 20 meteor showers. By using physical parameters, we found the fast-rotator asteroid 2007RS146.

Key words: meteorites – meteors – meteoroids — minor planets – asteroids.

1. INTRODUCTION

The meteor showers represent the ablation of solid particles or fragments, namely meteoroids, in the upper atmosphere of the Earth. The main source of these meteoroids are comets and asteroids (Jopek and Williams, 2013, and references).

At first, it was believed that only comets can produce meteor showers, but is was suspected that asteroids may also have the ability to produce fragments of matter (Olivier, 1925). This concept was accepted after the discovery of asteroids that could be extinct comets (Weissman *et al.*, 1989) and the asteroids with activity (Jewitt, Hsieh, and Agarwal, 2015).

In the previous study (Dumitru *et al.*, 2017), we associated asteroids with meteor showers by comparing their orbits with three D-Criteria metrics, namely (Southworth and Hawkins, 1963; Jopek, 1993; Asher, Clube, and Steel, 1993). For each metric we obtained a threshold value by using our own empirical method (see Dumitru *et al.*, 2017, Section 3.1), for each association were computed the D-parameter error and the asteroid orbital stability. Also, the associations were classified as high,

medium or low probability according to the number of metrics that were below the threshold (Dumitru *et al.*, 2017).

The simulation was made with IAU Minor Planet Center* (for asteroids) and IAU Meteor Data Center† (for meteor showers) databases from February 2017.

In this work we present an update of the Dumitru *et al.* (2017) results on association list by using the update databases for asteroids and meteor showers from February 2018.

2. ANALYSIS METHOD

In the new simulation, were used the same methods as for Dumitru *et al.* (2017).

We remove from the simulation the meteor showers Daytime κ Aquariids (MKA) and β Hydrusids (BHY). In these cases, the activity was observed in a single year (BHY in 1985 and MKA in 1961). Also, their orbital elements are incomplete.

As in the previous study, we created three categories of associations, of high, medium and low probability, according to the number of metrics that make the association. Also, in the case of meteor showers Corvids (COR) and h Virginids (HVI), due to the high percentage of associations (over 50% of the total number) we selected only the objects cataloged as high probability.

3. RESULTS

The new run uses the most recent databases of asteroids and meteor showers of February 2018. 72 new asteroids were associated in the cluster analysis process (see Table 1 and for the D-parameter values and other information see Table 2).

A part of those asteroids were not cataloged as possible parents in the previous study, due to their orbital parameter uncertainties. In the case of these asteroids, if the sum between D–parameter and the computed error exceeded the threshold value, the object was ignored. In the present study, these objects have been taken into account, because they have the D–parameter below the threshold.

All the associated asteroids are Near Earth Asteroids (NEAs) (Fig. 1a). 13 of them are on cometary like orbit ($2 < T_J < 3$) and 58 of them are on asteroidal orbit ($T_J > 3$). Here T_J represent the Tisserand parameter computed using Jupiter planet (i.e. the influence of Jupiter gravity field as the disruptive object of asteroid's orbit). One of the asteroids from Table 1 (2013 HT25) belongs to the category of Damocloids ($T_J < 2$).

From the Tisserand parameter (TJ) point of view (Fig. 1b), with respect to

*https://www.minorplanetcenter.net/

†http://pallas.astro.amu.edu.pl/~jopek/MDC2007/index.php

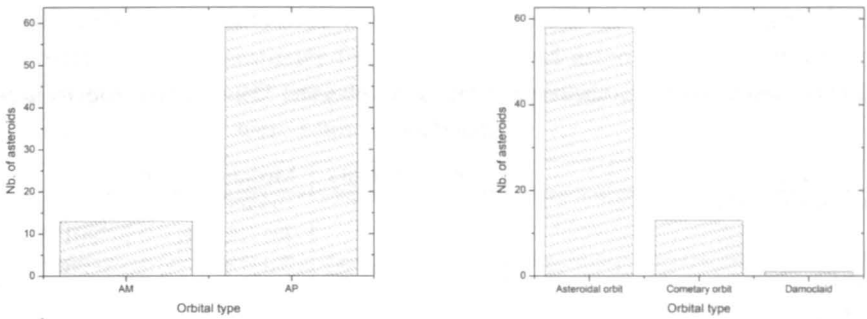

Fig. 1 – Orbital type of the associated asteroids after their position (left) and TJ (right).

Jupiter, we found 13 asteroids that have cometary like orbit ($2 < TJ < 3$), 58 asteroids that have asteroidal orbit ($TJ > 3$) and one asteroid that belongs to the minor planet group of damocloids ($TJ < 2$).

In addition to the cluster analysis, we search in the literature for physical parameters of objects from Table 1, and we found only three objects described only by the rotational period, namely: 2002 GM5 – 2.633 ± 0.003 h (Vaduvescu *et al.*, 2017), 2007RS146 – 0.03209 ± 0.00004 h (Kwiatkowski *et al.*, 2010) and 2017 MB1 – 6.69 ± 0.01 h (Warner, 2018).

The rotation period can help us to distinguish between asteroids with monolithic and rubble-piles structure. Pravec *et al.* (2006) studied the relationship between asteroids diameter and rotation period and found a limit at 2.2 h, which they called it the spin barrier. If the asteroid is larger than 200 m and the rotation period is larger than spin barrier, that asteroid is assumed to have a rubble-pile structure. If an asteroid has the rotation period smaller than the spin barrier, that asteroid is assumed the have monolithic structure.

In our case, we found one fast-rotating asteroid, namely 2007RS146, that has a rotational period of 0.03209 ± 0.00004 h (Kwiatkowski *et al.*, 2010) and diameter (derived from magnitude and assumed albedo) between 65 and 147 m. This asteroid has most likely a monolithic structure and can not produce meteor showers. Because of this, it was removed from the associated sample.

Additional objects to the list of Dumitru *et al.* (2017). 72 asteroids (24 associations with high probability and 52 associations with medium probability). The asteroids in bold are associated to several meteor showers and those underlined are the asteroids found with physical data (taxonomy, albedo or rotation period). Corvids (COR) and h Virginids (HVI) are on the last two lines and only high probability associations are presented.

Table 1

List of 72 asteroids (24 associations with high probability and 52 associations with medium probability)

Cod	Name	High Probability	Medium Probability
AND	Andromedids		1995FF, 2010TN167, 2017FL101, 2017SB33, 2017UE5, 2017UL7, 2017UM1
APS	Daytime April Piscids		2013HT25
AUD	August Draconids		***2017NW5***
CAP	α Capricornids		1995CS, 2012BQ123, 2017MB1, 2017QT1
DLT	Daytime λ Taurids		2017SK10
DPC	December ϕ Cassiopeiids		2017UE45
EVI	η Virginids		2001FB90, 2010VF, 2015TC144
KCG	κ Cygnids		***2017NW5***
NCC	Northern δ Cancrids	2006BF56	2008WZ94, **2017YO4**, 2018AK12
NTA	Northern Taurids		2010VN139, 2016TP18
OCC	October Capricornids		2005RA, 2005RJ, 2005XN27, 2007WW3, 2008SH148, 2016TV93, 2017VC13, 2017VM2, 2017YC6
PPU	π Puppids		1997UZ10, 2014SM142, 2014WN202, 2017UW7, 2017XC2
SCC	Southern δ Cancrids	***2017YO4***	
SMA	Southern Daytime May Arietids		2015PM307, 2017QN18
SSG	Southern μ Sagittariids		2010CR5, 2015BL311, 2018BT6
STA	Southern Taurids	2007UL12	2017UM44
ZPE	Daytime ζ Perseids		2007TC14
AVB	α Virginids	2017FU64	2002GM5, 2014HD198, 2014HK197, **2014HN199**, **2014HT197**, 2017JA, 2017SP12
COR	Corvids	2004LA10, 2004NU7, 2008LB, 2012KX41, 2014HE197, **2014HT197**, 2016PE8, 2017KQ27, 2017MA3, 2017QB17, 2017SA, 2017SG33	
HVI	h Virginids	2007RS146, 2009SD15, 2010RZ11, 2010TD, 2012KZ41, **2014HN199**, 2014JH15, 2016RO40	

List with new associations and D-parameters. The columns are: the asteroid name, the orbital elements used for MPCORB, the Lyapunov time, associated meteor shower, the D—parameter for all metrics and asteroids diameter which is an estimation computed with asteroid absolute magnitude and an albedo set to 0.15. The diameters with "*" were found in literature.

Table 2: D-parameter and Lyapunov time for all asteroids--meteor showers associations

Asteroid	a[a.u.]	e	i[deg.]	T_L	Shower	D_{acs}	D_{sh}	D_j	Diameter [km]
1995CS	1.939	0.774	2.596	60	CAP		0.1853	0.1836	0.027
1995FF	2.317	0.709	0.595	56	AND		0.1852	0.1748	0.018
1997UZ10	2.837	0.62	12.779	301	PPU		0.1791	0.1651	0.082
2001FB90	2.467	0.777	1.883	116	EVI		0.1499	0.1494	0.359
2002GM5	2.113	0.695	7.280	82	AVB		0.1652	0.1503	2.633*
2004LA10	2.509	0.576	1.080	85	COR	0.0594	0.0871	0.0665	0.034
2004NU7	2.233	0.545	0.896	65	COR	0.0557	0.1455	0.1447	0.057
2005RA	2.552	0.659	4.419	92	OCC		0.2034	0.1778	0.125
2005RJ	2.578	0.664	6.327	116	OCC		0.1929	0.1634	0.119
2005XN27	2.406	0.633	0.299	46	OCC		0.2070	0.1871	0.045
2006BF56	2.342	0.799	0.962	31	NCC	0.0504	0.1817	0.1846	0.004
2007RS146	2.366	0.644	2.665	49	HVI	0.0448	0.1127	0.0813	0.065*
2007TC14	2.09	0.806	4.659	169	ZPE		0.1589	0.1710	0.130
2007UL12	1.97	0.806	4.187	62	STA	0.0221	0.1733	0.1754	0.227
2007WW3	3.109	0.653	6.484	40	OCC		0.1958	0.1784	0.060
2008LB	2.455	0.607	4.223	57	COR	0.0577	0.0928	0.0881	0.015
2008SH148	2.751	0.657	3.847	37	OCC		0.1697	0.1654	0.021
2008WZ94	1.522	0.774	6.528		NCC		0.1464	0.1572	0.328
2009SD15	2.346	0.621	2.904	87	HVI	0.0561	0.1978	0.1601	0.014
2010CR5	3.186	0.824	5.395	90	SSG		0.1499	0.1487	0.376
2010RZ11	2.337	0.634	1.280	46	HVI	0.0320	0.1615	0.1352	0.016
2010TD	2.177	0.676	3.228	48	HVI	0.0557	0.0673	0.0622	0.014
2010TN167	1.698	0.588	5.385	56	AND		0.1851	0.1801	0.013
2010VF	1.854	0.754	3.709	44	EVI		0.1783	0.1784	0.026
2010VN139	1.874	0.748	1.511	56	NTA		0.1626	0.1809	0.043
2012BQ123	2.038	0.694	0.960	45	CAP		0.1538	0.1516	0.039
2012KX41	2.35	0.622	4.384		COR	0.0596	0.2092	0.1872	0.034
2012KZ41	2.297	0.602	1.566	47	HVI	0.0580	0.1905	0.1329	0.031
2013HT25	4.524	0.945	5.185	94	APS		0.1845	0.1845	0.006
2014HD198	2.103	0.642	0.986	44	AVB		0.1878	0.1877	0.004
2014HE197	2.214	0.598	3.222	56	COR	0.0538	0.1369	0.1008	0.024
2014HK197	2.335	0.65	5.560	124	AVB		0.1406	0.1287	0.014
2014HN199	2.215	0.653	2.901	199	AVB		0.1849	0.1841	
					HVI	0.0416	0.0710	0.0683	0.016
2014HT197	2.246	0.609	2.072	44	AVB		0.1962	0.1658	
					COR	0.0526	0.1765	0.1433	0.007

Table 2: continued.

Asteroid	a[a.u.]	e	i[deg.]	T_L	Shower	D_{acs}	D_{sh}	D_j	Diameter [km]
2014JH15	2.316	0.624	1.525	64	HVI	0.0385	0.1496	0.1105	0.045
2014SM142	2.576	0.596	26.711	302	PPU		0.1683	0.1646	0.109
2014WN202	2.574	0.579	13.465	102	PPU		0.2026	0.1889	0.143
2015BL311	2.368	0.844	1.717	101	SSG		0.1764	0.1862	0.207
2015PM307	2.225	0.863	8.090	88	SMA		0.1734	0.1792	0.157
2015TC144	2.304	0.777	3.063	123	EVI		0.1549	0.1554	0.047
2016PE8	2.47	0.597	2.352	80	COR	0.0478	0.1186	0.1186	0.016
2016RO40	2.295	0.649	3.832	74	HVI	0.0523	0.1047	0.0930	0.043
2016TP18	1.094	0.686	4.646	49	NTA		0.1867	0.1871	0.038
2016TV93	2.828	0.608	2.016	704	OCC		0.2035	0.1730	0.039
2017FL101	2.847	0.785	4.618	218	AND		0.1993	0.1721	0.026
2017FU64	2.445	0.707	6.907	58	AVB	0.0362	0.1232	0.1215	0.057
2017JA	2.032	0.616	1.978	49	AVB		0.1791	0.1769	0.006
2017KQ27	2.335	0.589	4.773	75	COR	0.0425	0.1358	0.1314	0.024
2017MA3	2.353	0.578	4.005	63	COR	0.0255	0.1245	0.1244	0.015
2017MB1	2.372	0.753	8.508	176	CAP		0.0463	0.0461	0.516*
2017NW5	3.050	0.709	28.956	60	AUD		0.1791	0.1469	
					KCG		0.1602	0.1318	0.227
2017QB17	2.301	0.515	2.472	117	COR	0.058	0.1639	0.1281	0.034
2017QN18	2.147	0.831	6.656	123	SMA		0.1357	0.1752	0.299
2017QT1	2.546	0.751	1.120	67	CAP		0.1806	0.1777	0.015
2017SA	2.442	0.548	2.595	122	COR	0.0381	0.1132	0.0665	0.130
2017SB33	1.850	0.625	11.348	454	AND		0.1740	0.1673	0.065
2017SG33	2.397	0.550	5.415	154	COR	0.0557	0.1858	0.1721	0.060
2017SK10	2.064	0.932	24.591	4098	DLT		0.1207	0.1861	0.164
2017SP12	1.804	0.622	11.569	47	AVB		0.1588	0.1525	0.285
2017UE45	2.829	0.673	15.106	67	DPC		0.1483	0.1462	0.596
2017UE5	2.012	0.599	6.073	117	AND		0.1641	0.1599	0.095
2017UL7	2.211	0.661	2.479	133	AND		0.1708	0.1707	0.045
2017UM1	1.971	0.654	4.065	124	AND		0.1562	0.1461	0.026
2017UM44	1.756	0.745	8.486	54	STA		0.1239	0.1427	0.047
2017UW7	2.532	0.606	14.860	153	PPU		0.1805	0.1804	0.010
2017VC13	2.706	0.606	3.307	234	OCC		0.1847	0.1717	0.029
2017VM2	2.613	0.615	1.969	119	OCC		0.1566	0.1557	0.075
2017XC2	2.580	0.581	20.684	3424	PPU		0.1600	0.1430	0.359
2017YC6	2.753	0.702	0.358	58	OCC		0.1857	0.1241	0.023
2017YO4	2.236	0.830	7.400	76	NCC		0.1488	0.1505	
					SCC	0.0513	0.1525	0.1565	0.227
2018AK12	1.926	0.710	2.532	61	NCC		0.1819	0.1859	0.031
2018BT6	2.279	0.830	3.020	158	SSG		0.1642	0.1702	0.197

4. CONCLUSIONS

We updated the existing list of asteroids associated with meteor showers. From the simulation we obtained 72 new asteroids that can be associated to 20 meteor showers. The associated objects have Apollo and Amor orbits, but are not cataloged as potential hazardous. With the help of the Tisserand parameter we concluded that 13 asteroids are on cometary orbits, 58 asteroids are on asteroidal orbits and one asteroid belongs to Damocloid group.

By using physical data we found one asteroid that can not produce meteor showers, namely 2007RS146. This asteroid is a fast-rotator.

REFERENCES

Asher, D.J., Clube, S.V.M., Steel, D.I.: 1993, Asteroids in the Taurid Complex. *Mon. Not. Roy. Astron. Soc.* **264**, 93. doi:10.1093/mnras/264.1.93.

Dumitru, B.A., Birlan, M., Popescu, M., Nedelcu, D.A.: 2017, Association between meteor showers and asteroids using multivariate criteria. *Astron. Astrophys.* **607**, A5. doi:10.1051/0004-6361/201730813.

Jewitt, D., Hsieh, H., Agarwal, J.: 2015, In: Michel, P., DeMeo, F.E., Bottke, W.F. (eds.) *The Active Asteroids*, 221 – 241.

Jopek, T.J.: 1993, Remarks on the meteor orbital similarity D-criterion. *Icarus* **106**, 603. doi:10.1006/icar.1993.1195.

Jopek, T.J., Williams, I.P.: 2013, Stream and sporadic meteoroids associated with near-Earth objects. *Mon. Not. Roy. Astron. Soc.* **430**, 2377 – 2389. doi:10.1093/mnras/stt057.

Kwiatkowski, T., Buckley, D.A.H., O'Donoghue, D., Crause, L., Crawford, S., Hashimoto, Y., Kniazev, A., Loaring, N., Romero Colmenero, E., Sefako, R., Still, M., Vaisanen, P.: 2010, Photometric survey of the very small near-Earth asteroids with the SALT telescope . I. Lightcurves and periods for 14 objects. *Astron. Astrophys.* **509**, A94. doi:10.1051/0004-6361/200913152.

Olivier, C.P.: 1925, *Meteors*.

Pravec, P., Scheirich, P., Kušnirák, P., Šarounová, L., Mottola, S., Hahn, G., Brown, P., Esquerdo, G., Kaiser, N., Krzeminski, Z., Pray, D.P., Warner, B.D., Harris, A.W., Nolan, M.C., Howell, E.S., Benner, L.A.M., Margot, J.L., Galád, A., Holliday, W., Hicks, M.D., Krugly, Y.N., Tholen, D., Whiteley, R., Marchis, F., DeGraff, D.R., Grauer, A., Larson, S., Velichko, F.P., Cooney, W.R., Stephens, R., Zhu, J., Kirsch, K., Dyvig, R., Snyder, L., Reddy, V., Moore, S., Gajdoš, Š., Világi, J., Masi, G., Higgins, D., Funkhouser, G., Knight, B., Slivan, S., Behrend, R., Grenon, M., Burki, G., Roy, R., Demeautis, C., Matter, D., Waelchli, N., Revaz, Y., Klotz, A., Rieugné, M., Thierry, P., Cotrez, V., Brunetto, L., Kober, G.: 2006, Photometric survey of binary near-Earth asteroids. *Icarus* **181**, 63 – 93. doi:10.1016/j.icarus.2005.10.014.

Southworth, R.B., Hawkins, G.S.: 1963, Statistics of meteor streams. *Smithsonian Contributions to Astrophysics* **7**, 261.

Vaduvescu, O., Macias, A.A., Tudor, V., Predatu, M., Galád, A., Gajdoš, Š., Világi, J., Stevance, H.F., Errmann, R., Unda-Sanzana, E., Char, F., Peixinho, N., Popescu, M., Sonka, A., Cornea, R., Suciu, O., Toma, R., Santos-Sanz, P., Sota, A., Licandro, J., Serra-Ricart, M., Morate, D., Mocnik, T., Diaz Alfaro, M., Lopez-Martinez, F., McCormac, J., Humphries, N.: 2017, The EURONEAR Lightcurve Survey of Near Earth Asteroids. *Earth Moon and Planets* **120**, 41 – 100. doi:10.1007/s11038-017-9506-9.

Warner, B.D.: 2018, Near-Earth Asteroid Lightcurve Analysis at CS3-Palmer Divide Station: 2017 July Through October. *Minor Planet Bulletin* **45**, 19 – 34.

Weissman, P.R., A'Hearn, M.F., Rickman, H., McFadden, L.A.: 1989, Evolution of comets into asteroids. In: Binzel, R.P., Gehrels, T., Matthews, M.S. (eds.) *Asteroids II*, 880 – 920.

Received on 20 November 2018

THE SOLAR CYCLE 24 GEOMAGNETIC STORMS TRIGGERED BY ICMES AND CIRS

CRISTIANA DUMITRACHE, NEDELIA A. POPESCU

Astronomical Institute of Romanian Academy,
Str. Cutitul de Argint 5, 040557 Bucharest, Romania
Email: crisd@aira.astro.ro

Abstract. Based on an automatic detection of the events during solar cycle 24, developed on specific criteria in terms of the solar wind plasma parameters and magnetic field, we approach a statistical study of the geomagnetic storms produced by the *interplanetary coronal mass ejections* (ICMEs), *corotating interaction regions* (CIRs) and other sources, as *heliospheric current sheet* (HCS) and magnetic reconnections in the solar wind.

Key words: Heliosphere – automatic detection – interplanetary coronal mass ejections – corotating interaction regions – solar wind – magnetic reconnections – geomagnetic storms.

1. INTRODUCTION

The interplanetary events can be identified in the solar wind data using defined signatures, more or less restrictive. The requirements imposed on the solar wind plasma and magnetic field should be concomitantly accomplished and more often there are applied by the visual inspection and interpretation of an author. The automatic detections of the events have the advantage to find out more features.

There are more attempts for automatic detection of ICMEs or for the geomagnetic storms, with different algorithms and philosophy of defining the events. For instance, Zuo *et al.* (2015) developed an algorithm useful to automatic detect the dynamic pressure pulses in the solar wind. This algorithm enable them to identify the upstreams and downstreams in the solar wind.

Lepping, Wu, and Berdichevsky (2005) have applied an automatic detection for MC identification, through a two-step process: first they detected the regions with low proton plasma beta, degree of small-scale smoothness of the magnetic field's directional change, duration of the event, the thermal speed and field strength. In the second step they have tested the large-scale smoothness of the magnetic field for the candidates obtained at the first step.

Shinohara, Kikuchi, and Nozaki (2005) considered the sudden commencement (SC) as a good marker of a geomagnetic storm onset and the South magnetic field amplitude to be greater than 7.5 nT, while the increase period to be 10 less than

minutes, and the maximum time variation to be superior to 2.5 nT/minute.

The relation between (I)CMEs and the geomagnetic storms is already known from long years (Burlaga (1968),Wu and Lepping (2005), and many others).

Concerning the solar or interplanetary sources of the geomagnetic storms, there are few previous work and we remind here the work of Zhang *et al.* (2007) or of . Zhang *et al.* (2007) discussed the sources of the major geomagnetic storms (DST index less than -100 nT) between 1996 and 2005. They found three types of geomagnetic storms from a total of 85 analyzed events: (a) produced by ICMEs or magnetic clouds(MCs); (b) produced by CIRs; (c) a complex solar wind flow produced by multiple interacting ICMEs. For nine of these geomagnetic storms, the authors could not identify solar explosive events or active regions. also found three types of geomagnetic storms: produced by ICMEs/MCs, by sheath fields, and by sheath fields followed by CIRs or MCs.

A recent study of Watari (2017) analyzed seventeen major geomagnetic storms registered between 2009 and 2015 for which he identified their solar sources.

A study of Tsurutani and Gonzalez (1997) indicates the equal importance of both sheath fields or draped fields and driver gas fields for the generation of major geomagnetic storms.

Our goal was to detect automatically the interplanetary mass ejections (ICMEs), corotating interaction regions (CIRs), heliospheric current sheets (HCS), as well as the geomagnetic storms (Geo). By applying out software, we have obtained a catalogue of the events for the period 2008–2017. We have accounted a statistics of these events over the solar cycle. The next questions we were asked to answer was about the interplanetary source of the geomagnetic storms obtained by our algorithm. We considered four types of geomagnetic storms: that produced by ICMEs, by CIRs, by HCS (that linked to the IMF boundaries, as well as that multiple and locally current sheets), and the geomagnetic storms produced by complex configurations in different combination.

Gosling (2012) considers that magnetic reconnections is a fundamental plasma process occurring in the solar wind. They produce in thin current sheets and there are responsible for plasma acceleration.

In this article, we have interpreted the appearance of multiple local current sheets, that are also accompanied by the increase of the magnetic field magnitude and velocity, as signature of interplanetary magnetic reconnections. We appreciate that they could produce geomagnetic storms.

In the last section we have discussed a particular case of geomagnetic storm produced by the magnetic reconnections in the solar wind.

2. THE ALGORITHM

The identification of the events was performed imposing the following conditions:
- for ICMEs: $T/Texp \leq 0.5$; $\beta \leq 0.2$; $Bmag \geq 5$; $Np \geq 5$;
- for CIR: $T/Texp \geq 0.2$; v ascending trend; $Np \geq 10$;
- for HCS: the change of the sign of the interplanetary magnetic field polarity p_imf;
- for geomagnetic storms: $SymH \leq -50$.

The used data are: (a) ACE Spacecraft - Solar wind data for plasma and magnetic field, with 5 minutes resolution (Explorer); (b) OMNIWEB - SymH index, with 5 minutes resolution (Facility(SPDF)).

The interplanetary magnetic field polarity was computed as

$$p\_imf = \frac{-[Bx - \Omega R \cos\lambda By/v]}{\sqrt{1+(1+(\Omega R\cos\lambda/v)^2)}\sqrt{Bx^2+By^2}}$$

where $\Omega = 2.7 \times 10^{-6}$ s^{-1} is the solar rotation rate corresponding to 25.4 days of the Sun's sidereal rotation period, λ is the heliographic latitude and R is the spacecraft distance to the Sun. The polarity of the interplanetary magnetic field (IMF) is oriented toward the Sun when $sign(p\_imf)$ is minus, and away from the Sun when $sign(p\_imf)$ is plus.

3. RESULTS

We have obtained a catalogue with ICMEs, CIRs and geomagnetic storms, for the solar cycle 24 (2008–2017). Figure 1 plots the evolution of these event along the cycle.

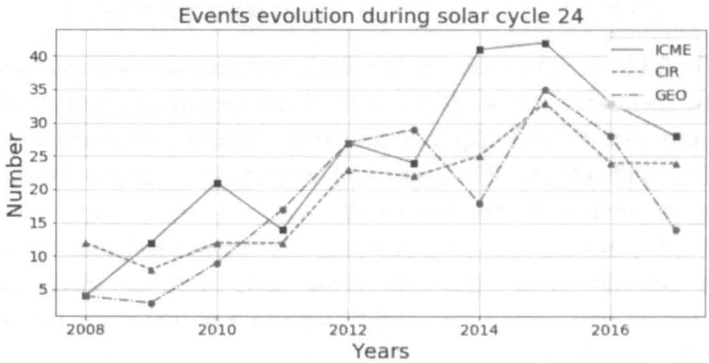

Fig. 1 – Evolution of the events during solar cycle 24.

We have searched for the interplanetary events that produced the the geomag-

netic storms. We have found four types of geomagnetic storms: - produced by ICMEs (denoted by *sicme*);
- produced by CIRs (denoted by *scir*);
- produced by interplanetary magnetic reconnections or by HCS (denoted by *srec*);
- produced by a combination of those above (denoted by *scomb*).

Figure 2 displays the evolution of the four category of geomagnetic storms during the solar cycle.

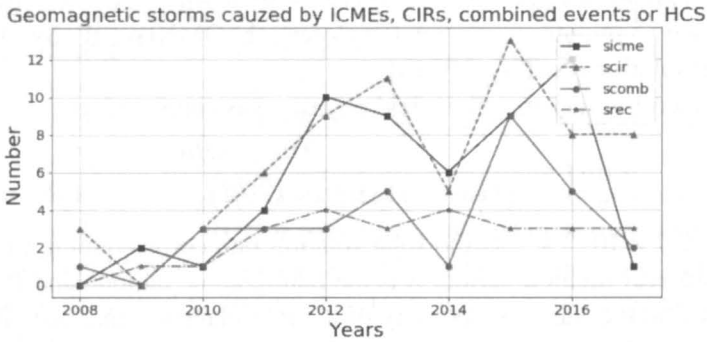

Fig. 2 – Distribution of the geomagnetic storms during the solar cycle.

What do we name interplanetary magnetic reconnections? When p_imf changes its sign for long time (days) we have a HCS, but when the IMF polarity has multiple changes during minutes/hours we have signature of interplanetary magnetic field reconnections. We found out that also multiple reconnections of solar wind produce geomagnetic storms. A particular such case is discussed in the next section.

4. A PARTICULAR CASE OF GEOMAGNETIC STORM

As we found in the previous section, there are geomagnetic storms for that we have not found a classical cause (ICME or CIR or combined event) by interpreting the interplanetary plasma and magnetic field data. Much more, the variations of the parameter p_imf indicates HCS existence or, at least, local current sheets, signatures of magnetic reconnections in the solar wind.

We exemplify here a case of a geomagnetic storm produced by local current sheets that we consider to be signatures of magnetic field reconnections. We have analyzed the period between DOY 123.55 and 124.5 in 2014, *i.e.* between 3 May, 13UT, and 4 May, 12UT 2014.

Figures 3 displays the properties of solar wind plasma and magnetic filed, as well as the polarity of the interplanetary magnetic field (p_imf).

Figure 3(a) plots the plasma beta (black continuum line) and the rate of the

proton temperature on the expected temperature $Tp/Texp$ (dash-dotted red line), where the expected temperature depends on the solar wind speed, and it was inferred for distances less 1 AU by Lopez and Freeman (1986), in 10^3 K units, as:

$$T_{exp} = \begin{cases} (0.0106v - 0.278)^3/r, & for \quad v < 500 \quad \text{km} \cdot \text{s}^{-1} \\ (0.77v - 265)/r, & for \quad v \geq 500 \quad \text{km} \cdot \text{s}^{-1} \end{cases} \tag{1}$$

We remind that for an ICME β should be less than 0.2 and $Tp/Texp \leq 0.5$. The time (on the abscissa) is expressed in day of the year (DOY). The shaded gray region represents strictly the period with SymH under the -50 threshold and not all the geomagnetic storm period (figure 3). The interplanetary magnetic field (IMF) changed its sign for short time periods (during minutes), *i.e.* p_imf changed its sign, at the following times (expressed in DOY): 123.6,123.685, 124.2, 124.22,124.34, 124.43, 124.65,124.75. These moments are marked on the figures 3(a–f) with vertical dot-dashed green lines, and white continuous line in and 3(e). The geomagnetic storm development is plotted in figure 3(f). Figure 3(b) displays the evolution of the proton density (black continuum line), as well as the dynamic pressure (dash-dotted red line). Figure 3(c) shows the velocity evolution, while (e) and (f) plot the solar wind magnetic field components evolution. Figure 3(d) plots the evolution of the computed parameter p_imf.

Figure 3(f) contains the plot of the geomagnetic index SymH. A sudden increase of the SymH to positive values represents the characteristic of the storm sudden commencement (SSC). After the SSC, it follows an interval that represents the initial phase of the storm, in which the maximum values of the magnetic field did not change significantly. For the main phase, a decrease of the SymH is present over a period from one to few hours, and the magnitude of magnetic storms can be defined by the minimum values of SymH (Gonzalez *et al.*, 1994). In our case, the SSC was produced by a small interplanetary shock that raised the solar wind speed from 308 km/sec to 334 km/sec, with an enhancement of plasma densities up to ~ 25.6 cm^{-3}. The SSC presented a value of SymH= 12 nT on DOY 123.74. The magnetic field magnitude reached a maximum value of 10.46 nT at the beginning of the initial phase. It is worth mention that, starting with DOY 123.75, a period of southward Bz lasted for 15 hours, until DOY 124.37. On DOY 123.79, SymH index begun to decrease with values under zero, indicating the start of the main phase of the storm. This moment corresponds to the peak of the solar wind speed (after another small shock). During the main phase of this geomagnetic storm a substantial increase in proton number density up to ~ 32 cm^{-3} was encountered for the interval between DOY 124.22 and DOY 124.24, together with a decrease of the magnetic field magnitude. The maximum of the geomagnetic storm was at 124.25, when SymH= -56 nT. The recovery phase of the storm lasted until DOY 125.16, when an ICME hit the Earth and produced a new geomagnetic storm at DOY 125.2, but one smaller, with

SymH minimal value equal to -37 nT. What do we learn from this? The first geomagnetic storm was stronger than the second one, in spite of an ICME that appeared later.

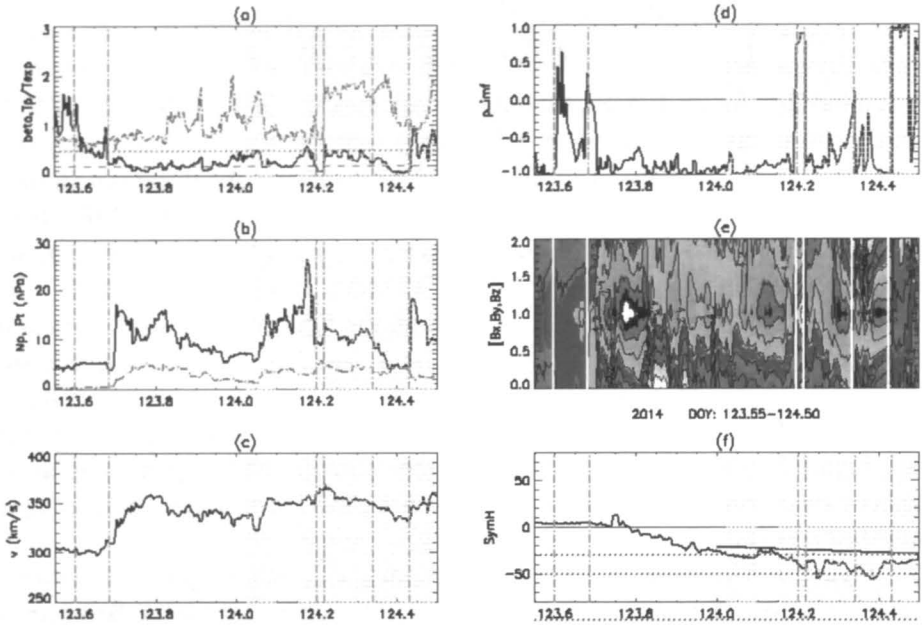

Fig. 3 – Plasma and magnetic field characteristics for the period DOY between 123.55 and 124.5. Geomagnetic storm produced by magnetic reconnections in the solar wind.

Figure 3(e) contains a visualisation of the magnetic field components *vs.* time, *i.e.* the contour plots of the matrix $[Bx, By, Bz]$. We can see the contour plots marking few interplanetary features similar to ICMEs but that do not accomplish all the ICMEs conditions: the temperature is too high in spite of low plasma beta conditions. These features are called plasmoids or magnetic islands in the solar wind by Zhang *et al.* (2007). Foullon *et al.* (2011) showed that the plasmoids are slow ICMEs structures with small length scales of the magnetic field - an order of magnitude than the magnetic clouds. Lin, Cranmer, and Farrugia (2008) found plasmoid, also named plasma blobs, in the magnetotail. Khabarova *et al.* (2016) showed that magnetic reconnections occur in many locations of a region filled with small-scale magnetic islands separated by thin current sheets. They have used the accelerated plasma flows to infer the presence of magnetic reconnections.

In our case, we have two currents sheet (DOY 123.6 and 123.685) and after them plasmoids are observed. At the end of the first plasmoid, at DOY=123.79, a bow shock occurred and also the SymH index became negative. A series of small

plasmoids continue the sequence of the solar wind and the plasma speed reached maximum 361 km/s. At DOY 124.05 and 124.2, new magnetic reconnections are visible, moments when the proton temperature high increased and the speed attaints 367 km/s. All these happened after a maximum of the proton density. Two other plasmoids follow and a new current sheet end the analysed sequences, being linked with the next event registered in the solar wind data - an ICME (not plotted in our figures).

Margnetic reconnections leads to particle acceleration (Zank *et al.*, 2014); he shows that magnetic islands of different scales are observed in Earth's magnetosphere frequently, and medium- and small-scale flux ropes or magnetic islands have been observed in the vicinity of the HCS. Khabarova (2011) showed that sharp changes of solar wind ion flux and density are geoeffective. These sharp changes are observed under dense, turbulent solar wind slow velocity conditions, with slightly increased values of the magnetic field strength. Khabarova and Zastenker (2011) found that 85% of them are associated with sector boundary crossings or local current sheets. Revising the moments of prominent shocks in plasma, by looking at the evolution of the proton density, we found DOY 123.685, 124.05 and 124.43. These moments corresponds to the beginning front of the first plasmoid, the third plasmoid and at the end of the last plasmoid.

Acceleration of energetic electrons during reconnection can be observed in the pitch-angle distribution. The pitch angle of a charged particle is the angle between the particle's velocity vector and the local magnetic field. Their distribution for different levels of energies give us information about the existence of current sheets and reconnections signaled by the energetic particle detection in situ. We have used the suprathermal electrons pitch angle plots from SWEPAM/ACE (Explorer), for the interval 3–4 May 2014.

Figure 4 displays the evolution of the suprathermal electron pitch angle distributions from SWEPAM, in the interval from 3 May 2014, 12UT, to 4 May 2014, 12UT. All the local current sheets from the moments DOY 123.6,123.685, 124.2, 124.22,124.34, 124.43 are visible in the SWEPAM pictures as discontinuities. For the easy reading of the moments we transcribe here them in the terms of day and hours. These are: for 3 May, 14.40UT, 16.44UT, and for 4 May, 4.80UT, 5.28UT, 8.16UT and 10.32UT. The last two current sheets (DOY 124.65 and 124.75) appeared after 4 May, 12UT. The color-coded pitch angle distribution of suprathermal (272 eV) electrons shows the strahl. The most intense beam is centered on 180° *pitch angle* (PA), before the current sheet crossing, and the beam of lower intensity is centered on 0° PA, after the crossing. This change of the pitch angle is in agreement with our results regarding the change of polarity described in Figure 3(d).

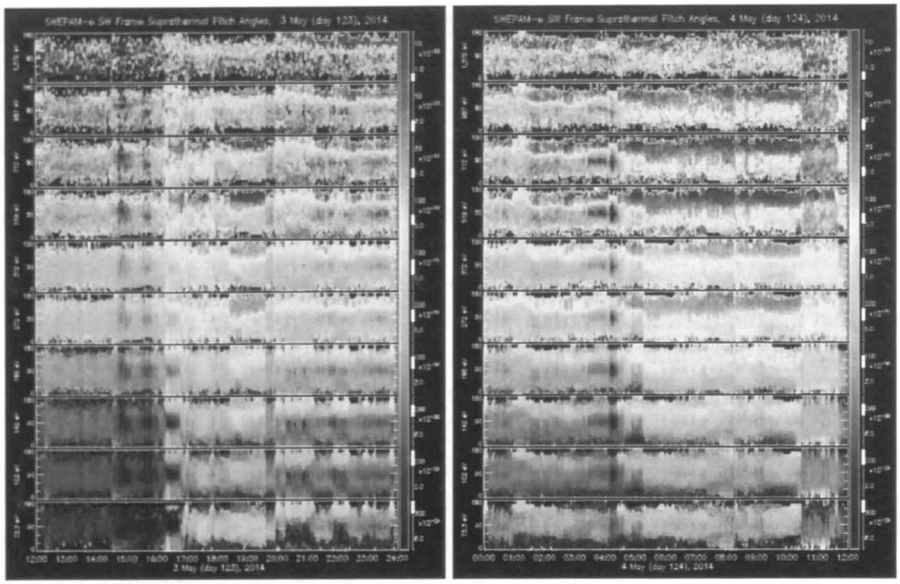

Fig. 4 – The color-coded suprathermal electrons pitch angle plots from SWEPAM for the interval DOY 123.5 – DOY 124.0 (left) and for DOY 124.0 – DOY 124.5 (right).

5. CONCLUSIONS

Our investigation focussed to summarize the geomagnetic storms during the solar cycle 24, by paying attention to the interplanetary causes of these storms. The events we have analysed were detected by an automatic algorithm, where only the period with defining conditions these type of events are accomplished and the beginning and end of them are neglected.

We have identified the precursor category of events to the geomagnetic storms and found three main categories:

– geomagnetic storms that are produced by ICMEs are -31%;

– geomagnetic storms that are produced by CIRs are -37%;

– geomagnetic storms that are produced by interplanetary magnetic reconnections or by HCS are -14%.

A fourth category is a combination of two or more other categories of storms, *i.e.* geomagnetic storms produced by complex events - these represent 18%. For five events we could not found an interplanetary cause.

Tsurutani and Gonzalez (1997) stated that during the solar maximum and few years after, the dominant interplanetary phenomena causing intense magnetic storms are the ICMEs. On the descendent phase of the cycle, close to the minimum, CIRs are dominant. Our results showed that near the maximum of the solar cycle 24 also CIRs and ICMEs are main causes of the geomagnetic storms. After the maximum, on

the descendant phase of the cycle, the combined complex events reached a maximum in 2015. The geomagnetic storms that we have identified as coming from magnetic reconnections in the solar wind have two maxima in the years of sunspot cycle maxima in this cycle: 2012 and the secondary maximum 2014. In fact, the maximum number in a year does not exceed four events of this type.

From a total of 178 geomagnetic storms we have automatic identified, 25 are produced by the magnetic reconnections, but for 5 events we have no explanations from the solar wind data analysed. We have found 54 major geomagnetic storms where $symH \leq -80$, among them 27 are produced by CIRs, 18 by ICMEs, 8 are combined and one is produced by magnetic reconnections.

A particular case of geomagnetic storm occurred after local interplanetary current sheets was discussed. These local interplanetary current sheets are signatures of magnetic reconnections, idea reinforced by the aspect of the contour plot of the magnetic field (3(e)). We think that these reconnections are due to the presence of more plasmoids in the solar wind. We remind that our catalogues of events (CIRs, ICMEs, geomagnetic storms) were obtained automatically, by using our own code.

The pitch-angle distribution confirm our retrieval of the interplanetary current sheets.

REFERENCES

Burlaga, L.F.: 1968, Micro-scale structures in the interplanetary medium. *Solar Physics* **4**(1), 67 – 92.

Explorer, A.C.: *(ace)*.

Facility(SPDF), S.P.D.: *Omniweb*.

Foullon, C., Lavraud, B., Luhmann, J., Farrugia, C.J., Retinò, A., Simunac, K., Wardle, N., Galvin, A., Kucharek, H., Owen, C.J., *et al.*: 2011, Plasmoid releases in the heliospheric current sheet and associated coronal hole boundary layer evolution. *The Astrophysical Journal* **737**(1), 16.

Gonzalez, W., Joselyn, J.A., Kamide, Y., Kroehl, H.W., Rostoker, G., Tsurutani, B., Vasyliunas, V.: 1994, What is a geomagnetic storm? *Journal of Geophysical Research: Space Physics* **99**(A4), 5771 – 5792.

Gosling, J.: 2012, Magnetic reconnection in the solar wind. *Space science reviews* **172**(1-4), 187 – 200.

Khabarova, O., Zastenker, G.: 2011, Sharp changes of solar wind ion flux and density within and outside current sheets. *Solar Physics* **270**(1), 311 – 329.

Khabarova, O.V., Zank, G.P., Li, G., Malandraki, O.E., le Roux, J.A., Webb, G.M.: 2016, Small-scale magnetic islands in the solar wind and their role in particle acceleration. ii. particle energization inside magnetically confined cavities. *The Astrophysical Journal* **827**(2), 122.

Lepping, R., Wu, C.C., Berdichevsky, D.: 2005, Automatic identification of magnetic clouds and cloud-like regions at 1 au: occurrence rate and other properties. In: *Annales Geophysicae* **23**, 2687 – 2704. Copernicus GmbH.

Lin, J., Cranmer, S., Farrugia, C.: 2008, Plasmoids in reconnecting current sheets: Solar and terrestrial contexts compared. *Journal of Geophysical Research: Space Physics* **113**(A11).

Lopez, R.E., Freeman, J.W.: 1986, Solar wind proton temperature-velocity relationship. *Journal of Geophysical Research: Space Physics* **91**(A2), 1701 – 1705.

Shinohara, M., Kikuchi, T., Nozaki, K.: 2005, Automatic realtime detection of sud-den commence-

ment of geomagnetic storms.

Tsurutani, B.T., Gonzalez, W.D.: 1997, The interplanetary causes of magnetic storms: A review. *Magnetic storms* **98**, 77 – 89.

Watari, S.: 2017, Geomagnetic storms of cycle 24 and their solar sources. *Earth, Planets and Space* **69**(1), 70.

Wu, C.C., Lepping, R.: 2005, Relationships for predicting magnetic cloud-related geomagnetic storm intensity. *Journal of atmospheric and solar-terrestrial physics* **67**(3), 283 – 291.

Zank, G.I., Le Roux, J., Webb, G., Dosch, A., Khabarova, O.: 2014, Particle acceleration via reconnection processes in the supersonic solar wind. *The Astrophysical Journal* **797**(1), 28.

Zhang, J., Richardson, I., Webb, D., Gopalswamy, N., Huttunen, E., Kasper, J., Nitta, N., Poomvises, W., Thompson, B., Wu, C.C., et al.: 2007, Solar and interplanetary sources of major geomagnetic storms (dst *leq* -100 nt) during 1996–2005. *Journal of Geophysical Research: Space Physics* **112**(A10).

Zuo, P., Feng, X., Xie, Y., Wang, Y., Li, H., Xu, X.: 2015, Automatic detection algorithm of dynamic pressure pulses in the solar wind. *The Astrophysical Journal* **803**(2), 94.

Received on 29 October 2018

NOTICE TO AUTHORS

ROMANIAN ASTRONOMICAL JOURNAL (RoAJ) is a peer-review journal that appears twice a year since 1991, covering the fields of Extra-galactic astronomy, Cosmology, Stellar Astrophysics, Solar Physics, Helio-sphere, Space Sciences, Celestial Mechanics, Astrometry, and History of the Astronomy.

The manuscripts submitted by authors must contain original scientific contributions, be prepared in English using a latex editor and accompanying figures in jpg or eps format. The manuscripts (pdf, latex and figures files) should be submitted to `roaj@aira.astro.ro`.

The first page should contain: articles title (brief and informative), author(s) name(s) and affilliation(s), followed by an Abstract in English, and Keywords. The text should be clear and concise. The Abstract will clearly present the main conclusions of the work, in no more than 10–15 lines. *The fonts* to be used are: 11pt. for the normal text, 13pt. for the paper title, 9pt. for author(s) name(s) and affiliation(s), abstract, keywords, titles of chapters and paragraphs, figure captions, tables, running titles, and references. *Chapters and Paragraphs:* Papers, except short notes, should be divided into chapters, numbered by Arabic numerals. Chapters may be divided into paragraphs denoted by the number of the chapter and the number of the paragraph; each chapter and each paragraph should have a short descriptive title (e.g. 3.2. Results). *Formulae* have to be centered and numbered consecutively in Arabic numerals, included in parentheses, on the right-hand side of the manuscript. Tables should be numbered consecutively in Arabic numerals; they should be introduced in the text at their appropriate place. *Figures* and illustrations should be submitted separately, in eps or jpg format, having a high quality, in order to allow their reproduction without retouching. Any lettering should be large enough to be readable after the figure has been reduced in size for printing. Captions should be introduced in the text at their appropriate place. All figures should be numbered consecutively in Arabic numerals and referred to in the text (e.g. Fig. 2 or Figs. 2-5). Photographs should be included only if essential and should be enlarged enough to allow a clear reproduction.

References should be indicated in the text by the authors name and year of publication. They should be listed in alphabetical and chronological order at the end of the paper, as follows: name and initial(s) of the author(s), year of publication, suitable abbreviation of the journal (or title of the book and publisher), its volume and page(s). The natbib package is necessary in order to obtain the correct bibliography style of this journal.

Detailed instructions for the preparation of manuscripts and the RoAJ latex style can be found at the journal page: `http://www.astro.ro/~roaj`.

CONTENTS

ISSN 2285-3758
ISSN-L 1220-5168

Rom. Astron. J., **Vol. 28**, No. 1, P. 65–182, Bucharest, 2018